# Fluid Transport in Oscillatory Flows

by

Ruy Ibanez Amador

Submitted in Partial Fulfillment

of the

Requirements for the Degree

Doctor of Philosophy

Supervised by

Professor Douglas H. Kelley

Department of Mechanical Engineering
Arts, Sciences and Engineering
Hajim School of Engineering and Applied Sciences

University of Rochester
Rochester, New York

2023

Dedicated to Ivy Sol Ibanez and Daniel Ibanez S.

# Table of Contents

# Biographical Sketch

Ruy Ibanez Amador moved from Mexico to the United States of America in 2010 when he started his studies in economics at the University of Texas at Austin. During his first year, he found his passion for physics and went on to graduate with B.S. in physics in 2015. In 2013 he first began doing research in fluid mechanics with Dr. Harry Swinney and Bruce Rodenborn. Afterward, he joined Baylor University where he got a Master's in Mechanical Engineering and continued his research in fluid mechanics with Dr. Joseph Kuehl.

He joined the University of Rochester in 2017 and continued his work in research focused on experimental fluid mechanics. He worked there with Dr. Doug Kelley on projects involving understanding flows in the inner ear and the glymphatic system.

List of publications:

1. Ibanez, R., and D. H. Kelley. "A bioinspired apparatus for modeling peristaltic pumping in biophysical flows." *Bioinspiration and Biomimetics* **17.6** (2022): 066023.

2. Ibanez, R., Shokrian, M., Nam, J. H., and Kelley, D. H. "Simple analytic model for peristaltic flow and mixing." *Physical Review Fluids* **6.10** (2021): 103101.

3. Ibanez, R., Kuehl, J., Shrestha, K., and Anderson, W. "Brief communication: A nonlinear self-similar solution to barotropic flow over varying topography." *Nonlinear Processes in Geophysics* **25.1** (2018): 201-205.

4. Ibanez, Ruy, Harry L. Swinney, and Bruce Rodenborn. "Observations of the stratorotational instability in rotating concentric cylinders." *Physical Review Fluids* **1.5** (2016): 053601.

# Acknowledgments

Without the following people, I would have never been able to complete this work: Ivy Ibanez, Janelle Thomas, Daniel Ibanez, Diana Amador, Ava Ibanez, Harry Swinney, Bruce Rodenborn and Joseph Kuehl.

# Abstract

This thesis focused on the study of oscillatory flows in two special cases. First, it explored the dynamics of peristaltic pumping and its role in the functioning of the biological auditory system. Specifically, it was established that the tunnel of Corti's fluid, containing potassium ions, undergoes deformations at its walls which push fluid, producing electrical signals that the brain interprets as sound. To ensure healthy functioning of the auditory system, it was demonstrated through the development of an experimental and analytic model that peristaltic pumping plays a role in homogenizing the concentration of ions in the tunnel of Corti. Furthermore, the experimental and analytic model provided a novel approach for modeling complex waveforms in peristaltic pumping. The second oscillatory flow study sought to gain a better understanding of flow dynamics in the glymphatic system, which consists of oscillatory flows and complex channel networks with bifurcations. It was found that an oscillating flow coupled with a junction was sufficient to induce a directional flow.

# Contributors and Funding Sources

This work was supervised by a dissertation committee consisting of Professors Douglas H. Kelley and Professor Jong-Hoon Nam of the Mechanical Engineering Department, and Professor Pierre Gourdain of the Department of Physics and Astronomy.

Funding for the projects presented in this thesis was provided by the National Science Foundation under award number CBET-1552182 and the US Army Research Office grant MURI W911NF1910280.

Major contributions to my research on fluid flows in the inner ear were made by Dr. Douglas H. Kelley, Dr. Jong-Hoon Nam, and Mohammad Shokrian. Dr. Kelley provided guidance, expertise in fluid mechanics, and management throughout the study, Dr. Nam offered his expertise on the workings of the inner ear, and Mohammad conducted numerical simulations for the study. Dr. Kelley and Dr. Aditya Raghunandan were major contributors to the study of flows in the T-junction. Dr. Kelley provided guidance, expertise in fluid mechanics, and management. Dr. Raghunandan undertook large portions of the analysis with me.

# List of Figures

# 1 Introduction

In this thesis, I explore oscillatory flows in different systems, their implications on physiological systems, and their transport properties. Oscillatory flows are defined as a flow where the velocity field is periodic in time and has a periodic directionality. A simple example of an oscillatory flow is a tube where the fluid moves back and forth periodically.

## 1.1 Introduction

This thesis presents a series of studies on oscillatory fluid flows. Oscillatory flows are characterized as fluid flows in which the velocity follows a periodic pattern over time. This phenomenon can be expressed mathematically as

$$u_{oscillatory} = U_0 f_{periodic}(t), \tag{1.1}$$

where $t$ is time, $u_{oscillatory}$ represents the fluid velocity, $U_0$ is a velocity scale, and $f_{periodic}(t)$ is a periodic function of time, such as sine or cosine. It should be noted that $u_{oscillatory}$ and $U_0$ may have dependencies on other dimensions than time and still be considered oscillatory flows. For example

$$u_{oscillatory} = \sin(y)\cos(x - t), \tag{1.2}$$

where $x$ and $y$ are spatial dimension variables. A visual example of an oscillatory flow can be found in figure 1.1.

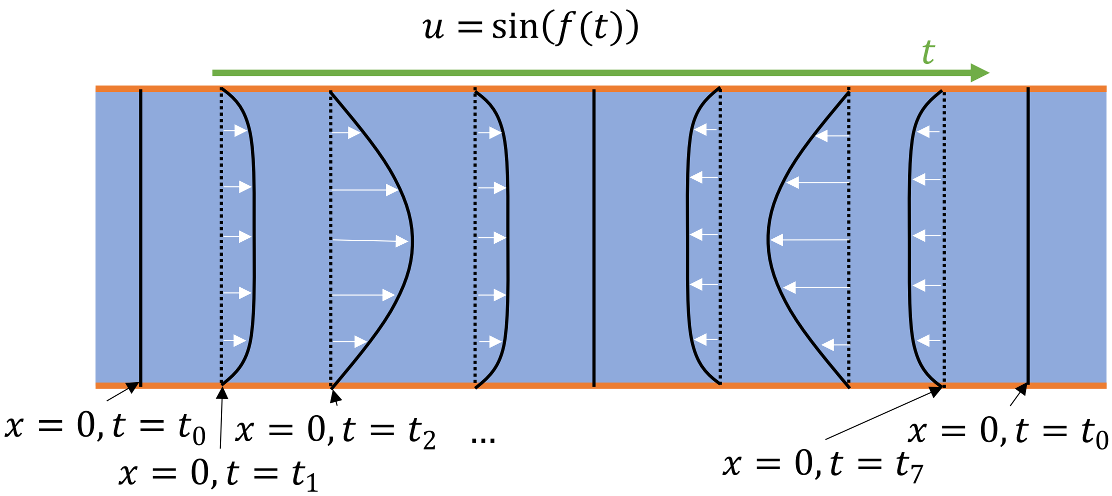


**Figure 1.1:** Shown is a sketch of a fluid-filled channel where an oscillatory flow is present. The black dotted lines indicate the center line from which the continuous black line gives the velocity profile of the flow at that point. The velocity profile is periodic and changes direction over the cycle. As such the profile oscillates over time.

Oscillatory flows play an important role in nature and industrial applications. The dynamics of oscillatory flows are not fully understood, since they can have dramatically different behaviors from non-oscillatory flows. As an example, consider a simple flow in a pipe (also referred to as Poiseuille flow). One simple way to describe the flow behavior is to look at the Reynolds number. The Reynolds number for Poiseuille flow is

$$Re_{Poi} = \frac{U_{\text{pipe}} D_{\text{pipe}}}{\nu}, \tag{1.3}$$

where $U_{\text{pipe}}$ is the average velocity of the flow at the pipe, $D_{\text{pipe}}$ is the diameter of the pipe, and $\nu$ is the kinematic viscosity of the fluid. The Reynolds number, a dimensionless quantity, provides valuable information by measuring the ratio of inertial and viscous forces in the flow. Applying the Reynolds number in analysis can be of great value in determining the characteristic dynamics of a flow within a pipe. However, calculating the Reynolds number for oscillatory flows is more challenging since the velocity is not constant. If one assumes that an oscillatory flow is solely a function of time, such as $\sin(t)$, computing the average would result in a value of zero, despite the fact that $\sin(t)$ possesses instantaneous speeds that are non-zero.

Given the prevalence of oscillatory systems found in nature, many previous studies [9, 14, 15] have developed techniques and approaches to analyze the dynamics of different oscillatory flows. Later in this thesis, I show how I approached these challenges in understanding oscillatory flows. The goal of my studies was to develop a better understanding of oscillatory flows found in the human inner ear. To accomplish this aim, I conducted experimental and analytical analyses, striving to replicate the flow conditions observed in the actual system as closely as possible.

Oscillatory flows are a general term for flows that exhibit a variation in time. While different oscillatory flows can share the criteria of a periodic flow in time, they can be dynamically different. To better illustrate this concept, consider that oscillatory flows can be induced in various ways, e.g. a piston moving back and forth displacing fluid or a periodic pressure gradient on a pile. Experimental observations suggest that the flow in the inner ear is generated via periodic deformations of the walls that contain the fluid. This means that the type of oscillatory flow found in the inner ear appears to be produced by peristaltic pumping. Thus, peristaltic pumping is one of the key types of oscillatory flows I study in this thesis.

In order to model and understand peristaltic pumping flows in the inner ear I used two approaches. First, I performed analytic analysis and was able to develop a simple and accurate analytic model of peristaltic flows for the parameter range of the inner ear. Second, I constructed and ran an experiment. The experiment consisted of a tabletop device that acted as a peristaltic pump. The device was capable of recreating peristaltic pumping with similar characteristics to those found in the inner ear. I performed cross-validation between the analytic and experimental results. Finally, I used the analytic model to determine if peristaltic pumping could play a role in the function of the inner ear by inducing fluid mixing. I found that peristaltic pumping does have a mixing effect and demonstrated the ability of the analytic model to model the mixing characteristics for the inner ear.

Another problem of interest in oscillatory flows is understanding flows and mass transport in the glymphatic system. The glymphatic system is a biological system that helps remove waste proteins from the brain. It is composed of a network of channels that transport cerebrospinal fluid, which helps to cleanse the brain of toxins and metabolic waste. At the time of writing, the physical mechanisms that produce mass transport in the glymphatic system are still an open question. Observations have shown [11] that the glymphatic system consists of a network of small channels which appear to exhibit an oscillatory flow, with some net transport properties.

I hypothesized that deformations of the wall are the mechanism that induces mass transport in the glymphatic system. However, my study of the inner ear suggested that peristaltic pumping was an unlikely candidate for the mechanism driving flow in the glymphatic system. This is due to the small deformations that have been observed in the glymphatic system are predicted to produce different flow characteristics than the ones that have been observed. As I discuss details of peristaltic pumping in chapter 2 and discuss flows in the glymphatic system in more detail in chapter 6, the challenge to the hypothesis that peristaltic pumping is what drives flow transport in the glymphatic system will become evident.

Similar to the study motivated by the inner ear, I created an experimental device designed to simulate conditions that resemble those present in the glymphatic system. While my model successfully replicated some of the glymphatic system's characteristics, it became apparent during the course of the experiment that the significant findings I obtained would be constrained in their similarity to the glymphatic system.

The experiment consisted of a closed-loop channel, where I induced an oscillatory flow. The closed-loop channel was set up in such a manner that the fluid has to pass through a T-junction. Based on my experimental observations, the configuration of the closed-loop channel with a junction can result in a net flow along the closed-loop, depending on how it is set up. It appears that the geometric properties of the closed-loop allow for the oscillatory flow to possess a net directional component, in addition to its oscillations.

## 1.2 Overview of the Thesis

Chapters 2 through 5 of this document are focused on an in-depth study of peristaltic flows, specifically within the context of the inner ear. These chapters have been devoted to exploring the context and significance of my study of peristaltic pumping, outlining the experimental design, presenting the results of analytic analyses, and engaging in discussions of the outcomes.

Chapters 6 through 8 of this thesis are dedicated to my research on oscillatory flows in closed-loop channels. The purpose of this study was to develop a model that could enhance our comprehension of the glymphatic system's flows. While the method employed in these chapters may not be the optimal analog, the research findings are substantial and could have potential applications in other systems. The chapters detail the motivation behind the study, the experimental design, the analytic analysis, and an extensive discussion of the findings.

Chapter 9 serves as the concluding segment of this thesis. In this chapter, a comprehensive summary of the key findings derived from the studies is presented, along with a discussion of their implications. Additionally, the chapter highlights how these findings align with the overarching theme of oscillatory flows, thereby bringing together the entirety of the research presented within this thesis.

# 2 Modeling Peristaltic Flows in the Inner ear

The following four chapters are dedicated to the series of experiments and analytic methods that I used to study peristaltic flows. The focus for these experiments was targeted towards developing a better understanding of flows in the inner ear as briefly discussed in section 1.2.

## 2.1 Introduction

To begin, let me introduce and contextualize what peristaltic flows are, why they are important, and why I was motivated to develop this study.

### 2.1.1 Importance of Peristaltic Pumping

Peristaltic pumping is a mechanism that is found often in various biological systems and specialized industrial applications for pumping fluids. Some examples of such systems and applications are: Pumping in the stomach [4], pumping in the urethra [16], medical applications [17], pumping sterilized industrial fluid [18], etc. Peristaltic pumping is unique in that it uses the deformation of the channel boundary to produce flow, unlike other pumping mechanisms that one will commonly see on a daily basis. That is, the channel containing the fluid deforms in such a manner that it displaces fluid through the system. For peristaltic pumping the deformation is specifically enforced by the boundary's periodic deformation, traveling along the channel. Peristaltic pumping, even though it operates using deformable walls, does not consider any form of fluid-structure coupling. In other words, the material properties of the deformable walls are not of importance. This is different from other forms of pumping where the boundary is deformed, such as impedance pumping, where the material properties play an important role. Figure 2.1 is a sketch that illustrates the basic principle of how peristaltic pumping works.

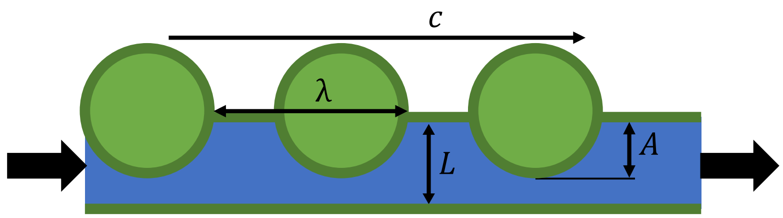


**Figure 2.1:** The diagram presented depicts the fundamental principles of peristaltic pumping. Specifically, a channel containing fluid, denoted by the color blue, experiences periodic deformation of its upper boundary through the action of green circles. These circles travel at a wave speed denoted by $c$ and possess a wavelength represented by $\lambda$. The deformation of the channel occurs by an amplitude denoted by $A$. As the green circles move toward the right side of the illustration, fluid displacement occurs, constituting the mechanism through which peristaltic pumping functions.

Peristaltic pumping is a process that involves the periodic deformation of the walls of a fluid-filled channel in a specific direction. The parameters that describe this process are the channel gap $L$, the deformation (or wave) amplitude $A$, a characteristic wavelength $\lambda$, and a deformation (or wave) speed $c$.

Fundamentally, the flow characteristics between a peristaltic pump that operates using amplitudes where the ratio $\epsilon$ of the channel gap to wave amplitude is large ($\epsilon = A/L \gg 0$) are very different from the case where the amplitude ratio is small ($\epsilon = A/L \approx 0$). To provide some physical intuition to the reader, the sketch in figure 2.2 is a visual guide to help illustrate how different dynamics ought to be expected. In the case of small amplitudes, observations show that an oscillatory flow is produced, where the fluid travels back and forth in the channel at some frequency. Obviously, in the case of large amplitudes, the wall deformation covers the entire channel and the fluid can only flow in one direction.

Most commercially available peristaltic pumps operate using amplitudes that span the entire channel gap $L$, for example: Xsample 200 from the manufacturer Anton Paar, and the Preciflow peristaltic pump from the manufacturer Sigma Aaldrich. The reason for this is that pumping efficiency (how much fluid is displaced for a given energy input) is proportional to the amplitude [19], thus maximum efficiency is achieved when $A = L$. On the other hand, small amplitude peristaltic pumping is found more frequently in nature [20, 21], and has been present in exploratory applications for microfluidics devices [22, 23].

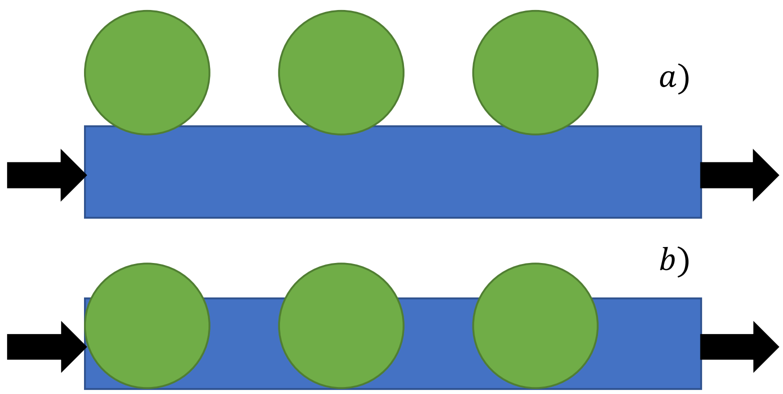


**Figure 2.2:** The purpose of this illustration is to demonstrate the distinct manners in which a peristaltic pump with a small amplitude (a) and one with a large amplitude (b) interact with the fluid domain. As depicted, in the latter scenario, the deformation of the channel is more pronounced, and the fluid becomes trapped as a result. Consequently, the available paths through which the fluid can travel are more limited when compared to the case of a smaller amplitude peristaltic pump.

The previous examples provide a clear demonstration of the critical role that amplitude plays in determining the dominant physics of peristaltic pumping. In order to streamline my study of the inner ear and avoid introducing unnecessary complexity to my model, it was crucial to identify these dominant factors. However, it is important to acknowledge that other parameters also have a significant impact. For example, wave speed has an intuitive effect on the flow velocity in peristaltic pumping, as faster waves would push the fluid faster. To gain a better understanding of the quantitative impact of each parameter, I explored their respective roles in the peristaltic pumping process.

Illustrated in figure 2.3, the inner ear of humans contains a small, fluid-filled channel known as the inner ear labyrinth, where an organ called the cochlea resides. This part of the inner ear is shared among mammals [24]. The function of the cochlea is to convert sound waves into electrical signals that can be interpreted by the brain as sound [24].

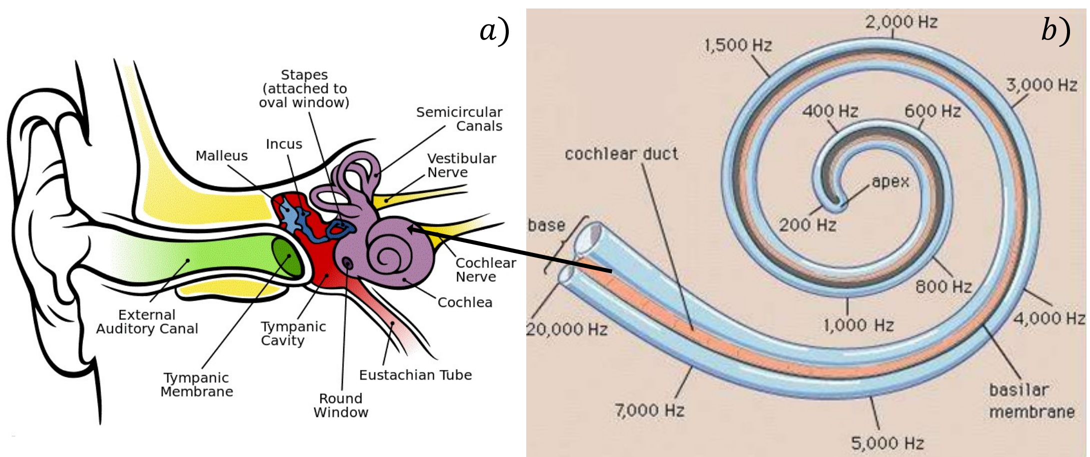


**Figure 2.3:** Sketches showing the inner ear and cochlea of a human. a) shows a sketch labeling different parts of the inner ear. Figure was modified from [1]. b) Shows a sketch of the organ named the cochlea. It shows how the cochlea is a spiral structure with two fluid-filled channels inside of them. The marked frequencies are the locations in the cochlea that are stimulated when hearing a frequency. Figure was taken from [2].

Straightening out the spiral structure of the cochlea and zooming in, one finds a channel within the cochlea named the tunnel of Corti. Figure 2.4 shows a sketch of the stretched-out cochlea. The tunnel of Corti is the location where essential chemical reactions occur for auditory function. A more detailed view of the structure of the channel can be seen in figure 2.5. Inside the tunnel of Corti, as a sound stimulates the cochlea, sections of the channel consume ions to produce an electrical signal [24]. This is because the location where the chemical reaction occurs is dependent on the frequency of the sound. This raises an important question: since ion consumption is localized and dependent on frequency, how does the tunnel of Corti remain homogenized enough to maintain function? In simpler terms, if ions are used at a specific spatial point in the channel, how is it replenished such that hearing is not affected?

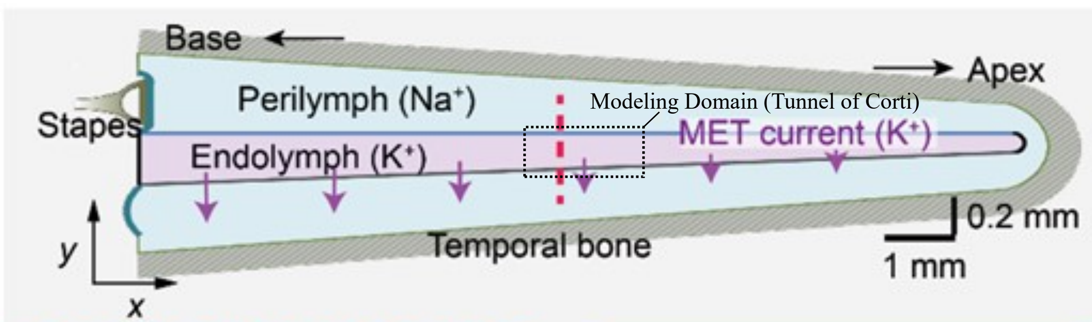


**Figure 2.4:** The illustration depicts a stretched-out representation of the cochlea, a structure within the inner ear that contains two channels, namely Endolymph and Perilymph. Of particular interest in this model is the Tunnel of Corti, a section within the Endolymph channel that undergoes compression during auditory stimulation. Figure from J.-H. Nam was modified.

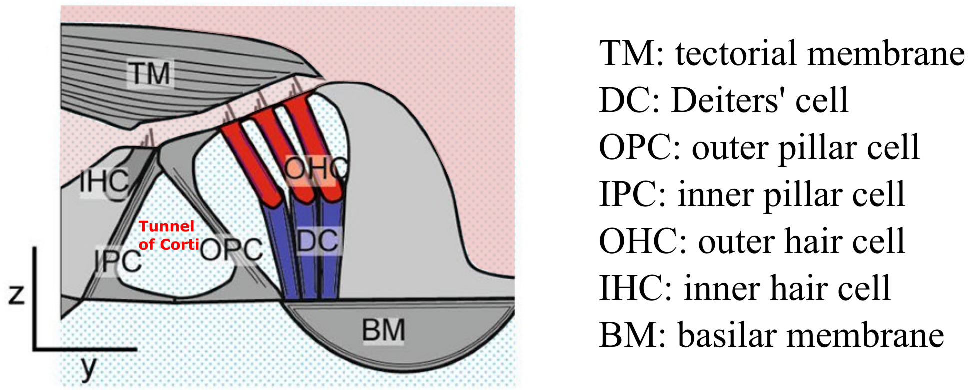


**Figure 2.5:** Side view of the organ of Corti. The triangular-like shape opening is the fluid channel of interest, the tunnel of Corti. Indicated are the outer hair cells, responsible for the deformations which I hypothesize drive flow in the system. The pink region corresponds to the Endolymph, and the blue region to the Perilymph. This figure was taken from [3].

Although there is consistent ion production along the tunnel of Corti, it seems insufficient to sustain optimal function. This issue has been a subject of discussion in several studies [25–28]. Due to this fact, one hypothesis was that diffusion would ensure that the tunnel of Corti ion concentration stays homogenized [29, 30]. However, the issue with this hypothesis is that the diffusion time scale is inadequate for the requirements of the auditory system. Doing some basic scale estimates for diffusion, I obtain the following: The diffusivity coefficient of potassium ions is $\Xi = 5 \cdot 10^{-10}$ m$^2$/s [25]. The spatial scale of diffusion for the tunnel of Corti is $L_{corti} = 10$ mm, which is the approximate length of the stretched-out cochlea for a rodent (10 mm for a human). The time scale $\tau$ for homogenization via diffusion is then given by

$$\tau = \frac{L_{corti}^2}{\Xi} \approx 2 \cdot 10^5 \text{ s.} \tag{2.1}$$

This estimated time scale for homogenization is too long for adequate function of the tunnel of Corti. For adequate hearing functionality, a time scale under the order of one second ($\tau < 1$) is needed. This brings us back to a potential solution to this problem, which could be that the induced peristaltic flow in the tunnel of Corti facilitates homogeneity by producing a mixing mechanism.

Peristaltic pumping is a potential mechanism due to the fact that during stimulation, the organ of Corti experiences deformation akin to those in peristaltic pumps. Karavitaki and Mountain [20] showed that a fluid flow was present in the tunnel of Corti. Ex-vivo observations by [31] showed that the outer hair cells contract, and are responsible for the deformations that create a flow given that they deform in a traveling wave along the channel. To get a better understanding of how these cells induce a flow when stimulated consider figure 2.5 which is a side view of the tunnel of Corti. The motion of the outer hair cells leads to a deformation of the organ of Corti which displaces the fluid in the tunnel of Corti, and coupling that with the traveling wave of the deformations, it is reasonable to hypothesize that some form of flow would be induced.

In summary, the tunnel of Corti can be modeled as a fluid-filled tube that experiences deformations. Now the question is whether the parameters of this channel induce a flow that assists in the homogenization of the tunnel of Corti, and thus plays a role in the auditory system of mammals.

This is why I developed the upcoming series of analyses presented in this thesis. While the inner ear was the primary motivation, let me make a brief pause before delving into the details of the study by mentioning how the analysis I performed has applications beyond just the inner ear. There are various biological systems that have similar characteristics to flows in the inner ear, as well as utility in industrial applications. A large number of biological systems use peristaltic pumping, as tissue and organic material tend to be malleable. The fact that the pumped fluid does not contact any additional parts other than the channel itself means that the fluid can be kept sterilized with ease when compared to alternative pumping mechanisms. Figure 2.6, shows a series of visual sketches of examples where peristaltic pumping is found other which are not in the inner ear.


**Figure 2.6:** Shown are examples of systems where one can find peristaltic pumping: a) Pumping in the stomach [4, 5]. b) Industrial applications on food processing [6]. c) Applications in medical pumps [7].

By now, I trust that I have adequately conveyed the significance of investigating peristaltic pumping. Moving forward, let us delve into the specifics of my research on this subject.

### 2.1.2 Analysis Overview

First, I will present previous studies on peristaltic pumping and the main takeaways from them. From that point, I will go on to describe a full mathematical analysis, which will give us a quantitative understanding of the relevant physics in peristaltic pumping. Understanding the mathematical fundamentals of the problem will lead to a full analytic model which I developed. This analytic model is capable of capturing the dynamics of peristaltic flows in the parameter range relevant to the inner ear. After presenting the details of the analytic model, it should the driving mechanisms for peristaltic flows will be clear. As such, I will move on to the details of the experimental approach. Drawing on insights from the analytic study as background knowledge, it will be more straightforward to comprehend the mechanics of the experimental device and its underlying objectives. Additionally, this knowledge can illuminate the reasoning behind the experimental design decisions that were made. Finally, I bring everything together as I show results from each approach, cross-validate, and apply my model to the inner ear by implementing the relevant parameters found in previous studies relating to the inner ear. The ultimate goal is to determine whether peristaltic flows play any role at all in the inner ear, and if so, whether peristaltic pumping plays a role in mixing fluids in the inner ear.

## 2.2 Peristaltic Pumping Literature Review

In this section, I present previous studies of peristaltic pumping with their key contributions and how each is relevant to my study. Former studies of peristaltic pumping are, typically, divided by the key parameters $A$ amplitude (also referred to as occlusion in other literature), $\lambda$ wavelength, $c$ is the deformation wave speed, and the undeformed channel width $L$. For a fundamental understanding of how peristaltic pumping functions, refer to Figure 2.1. The figure depicts a straightforward peristaltic pump model in which the motion of green circles generates deformations at a wall of the fluid channel, inducing a flow over the channel.

Perhaps the most important research on peristaltic pumping was performed by Shapiro et al.[19], and Weinberg et al. [32]. Their studies laid some of the foundations for the study of peristaltic flows, and as such are often cited in any paper that is related to peristaltic pumping. [19] aimed to establish a basic understanding of peristalsis, and the authors presented an analytic foundational theory of the physics underlying peristaltic pumping. Weinberg et al. [32] performed experiments that validated the former results. Given that their results lay the foundations of peristaltic pumping, I think it is important for me to lay out how their results are not sufficient for my application. They defined key non-dimensional numbers for the system. Reynolds number was defined as

$$Re = \frac{cL^2}{\nu\lambda}, \tag{2.2}$$

where $c$ is the wave speed, $L$ is the width of the channel and $\nu$ is the kinematic viscosity of the fluid. The ratio of the channel gap to the wavelength (which they call wavenumber),

$$L_\lambda = \frac{L}{\lambda} \tag{2.3}$$

where $\lambda$ is wavelength and $L$ is the width of the channel. And the amplitude ratio, also referred to as occlusion by some authors, was denoted as

$$\epsilon = \frac{A}{L}, \tag{2.4}$$

where $A$ is the amplitude of the wave and $L$ is the width of the channel. The analytic models that were developed by this group of researchers (Shapiro, Jaffrin, and Weinberg) have two crucial limitations that are relevant for my study of the inner ear: They are limited to low Reynolds numbers $Re \approx 0$ (although they make a limited extension to what they call 'moderate Reynolds number') and do not take into consideration the possibility of non-sinusoidal waveforms. That said, the contents of these studies are critical for anyone trying to study any sort of peristaltic pumping problem. Additionally, they discovered that the Lagrangian dynamics, which encompass the transport and motion of individual particles in the flow, were complex. Depending on certain conditions, particles in a peristaltic pump could be transported in a direction opposite to the flow or become trapped in orbits. Notably, these material transport properties could be vastly different from what one would assume based on an Eulerian perspective of the flow. A peristaltic flow may exhibit no net flow through a channel in the Eulerian perspective, yet be able to transport material from one side of the channel to the other due to the Lagrangian dynamics. Yih and Fung [33], and Yin and Fung [34] developed an analytic model and experimental model around the same time as Shapiro et al. [19]. Yih and Fung, and Yin and Fung were interested in the applications of peristaltic pumping for biological systems. One notable aspect is they used a slightly different definition for the Reynolds number from Shapiro et al., they used

$$Re_{YF} = \frac{cL}{\nu}, \tag{2.5}$$

where $c$ is the wave speed, $L$ is the width of the channel and $\nu$ is the kinematic viscosity of the fluid. Their study used a two-dimensional analytic model for peristaltic flows with small amplitudes and long wavelengths ($L_\lambda \gg 1$). Unfortunately, their study is held back by a lack of detail in the assumptions and limitations of the model. To obtain a more detailed look at the analytic model I studied the thesis by Yin [35], which includes more detail on the derivation of the solution, but found that at higher Reynolds numbers ($Re > 100$) and larger amplitudes ($\epsilon > 0.2$) the solution produced unphysical results. I was not able to determine the cause, but boundary conditions would not be met.

Lozano [36] conducted numerous investigations into peristaltic flows, utilizing numerical [37], analytic [38] and experimental [36] approaches. The scope of the studies was targeted to understand the role of peristaltic flow in the urethra. For the purposes of my study, Lozano's parameter regime is not a good analog. This is due to the nature of the flows in the urethra, which tend to have large deformations, i.e. $\epsilon \approx 1$. However, the experimental setup described in Lozano [36] served as inspiration for my own design. Lozano used a series of pneumatic actuators to deform a rubber tube filled with fluid in a periodic manner. This induced peristaltic flow in the tube which he studied. While elaborate, the experimental design lacked the fine control that I was seeking in terms of varying the amplitude and shape of the wave.

Ayukawa et al. [39] performed experiments and numerical analysis [40] of peristaltic flows at high Reynolds numbers $Re = 1000$ and long wavelengths $L_\lambda >$

1. They developed a simple model, which they find to be relatively accurate for the conditions of their experiment. They documented to have different findings from previous studies in terms of the Lagrangian motion of particles in the system. Although their findings did not align with some of the expected behavior reported in previous literature, it's important to note that the experiment was conducted for a limited range of parameters. Furthermore, at the time the experiments were performed, flow measurement techniques were relatively constrained.

Selverov [22] studied the effects of mixing produced by peristaltic pumping. Their interest was focused on microfluidic channels, similar to my interest. They found that at high frequencies of peristaltic pumping, fluid could be mixed. This goal was to determine the possibility of producing mixing in microfluidic channels, without the need for internal mechanical components. One significant difference from my study interest is that they studied the problem for an enclosed channel. Notably, they stressed the importance of analyzing the peristaltic flow from an Eulerian and Lagrangian perspective, adding further evidence that one can find interesting results depending on how the flow is analyzed.

There are numerous studies on peristaltic pumping in addition to the ones I have reviewed. The goal was to set a baseline background on peristaltic pumping with the former review. If the reader wishes to gain further insight into the analytic approach used in this paper, they should look into the specifics of the previous studies to gain a better understanding of the mathematical analysis.

## 2.3 Physics of Peristaltic Pumping

In this section, I will now focus on the physics of peristaltic pumping and how we can mathematically describe it. First, I consider the following simplified model depicted in figure 2.7. By using a simplified model, I can capture the essential dynamics of peristaltic pumping without the added complexities of a realistic model. The simple model consists of an infinite two-dimensional channel, where one wall is deformed by a periodic traveling wave. The system has coordinates $x$ in the horizontal spatial direction, $y$ in the vertical spatial direction, and $t$ for the time dimension. The channel gap is defined as the length from $y = 0$ to $y = L + \eta(x,t)$, where $\eta(x,t)$ is a function that describes the position of the deformable wall. The boundary conditions can be described as follows. $y = 0$ and $y = \eta(x,t)$ are no-slip conditions, while the channel extends infinitely in $x$.

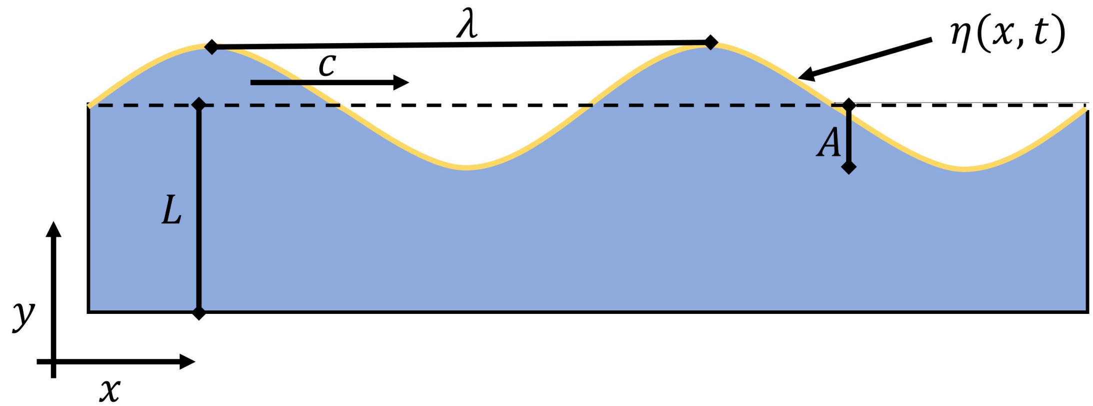


**Figure 2.7:** A schematic representation of the domain of the analytical model is presented. The domain is an infinite two-dimensional channel with a mean width of $L$ and a periodic spatial period of $\lambda$ in the $x$-direction. Fluid flow is induced by the periodic deformation of one boundary in the shape of $\eta(x,t)$ at a velocity of $c$ in the $x$-direction and an amplitude of $A$.

A large number of peristaltic flow studies [19, 22, 34, 39] limited themselves to only considering the case of a sinusoidal traveling wave deformation, where $\eta = A\sin(\alpha x - \omega t)$, $\alpha = 2\pi/\lambda$ and $\omega = 2\pi c/\lambda$. The reason for this is simplicity. Note that there are no other forcing mechanisms in the equations that describe peristaltic pumping. The boundary condition at the deforming wall is the source of pumping and energy for the system.

Before continuing with this analysis, it is important to consider if $\eta(x,t)$ is a dispersive wave or a non-dispersive wave. A dispersive wave is one which contains multiple wavelengths traveling at different phases, while a non-dispersive wave is one which can be followed by a deformation wave in a moving frame, thus appearing stationary. Figure 2.8 presents a visual example of the differences between dispersive and non-dispersive waves. Due to the complexity of the analysis for a dispersive wave, I limit the scope of my study of non-dispersive waves. In nature, dispersive waves do exist, such as those found in the inner ear [25]. However, for the purpose of simplifying the analysis, nonlinearities associated with dispersive waves are not addressed in this thesis.

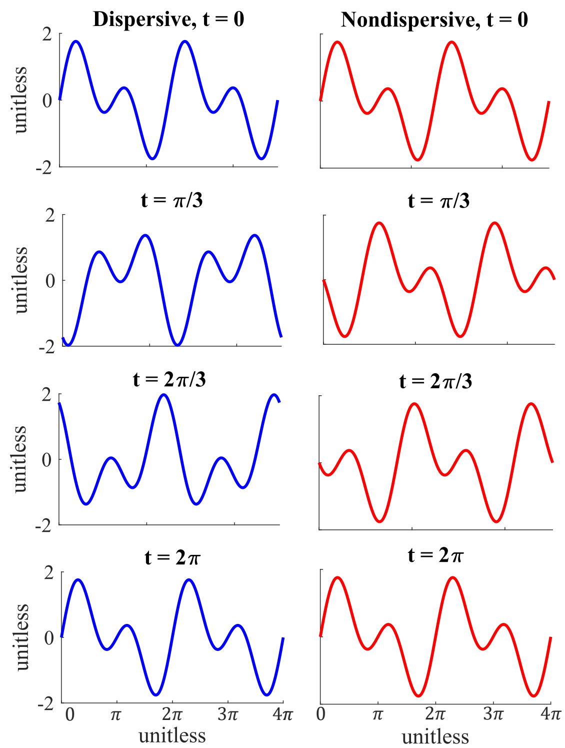


**Figure 2.8:** Comparison of a nondispersive wave and a dispersive wave. One can see how a nondispersive wave has a specific periodic shape which simply translates in one direction in $y$. The dispersive wave has a more complex evolution over time.

The model I considered did not take into account the material properties of the deformable wall, as they are not relevant when imposing a specific velocity on the wall. This means that the wall position is dictated by the boundary condition at the wall, and the fluid must move at the same velocity as the wall in order for the model to be valid. Thus, an interaction between the deformable wall and the fluid is not necessary, and the only information needed regarding the wall is the velocity it is deforming at.

As I hinted at in the literary review in section 2.2, I will first go over a brief overview of the fundamental differences between the Eulerian and Lagrangian perspectives for fluid flow analysis. To understand the fundamental differences between the two perspectives, one must go back to how the foundations of fluid physics are described. Figure 2.9 serves as a visual aid to help understand the differences between the two perspectives. I have the option to look at a fluid as many individual fluid parcels that compose the entire fluid. I then can describe a flow using these fluid elements over time. The difficulty with this approach comes from the fact that it is mathematically difficult to solve for large numbers of individual elements, whose positions, velocities, and other parameters change over time and space. The Eulerian perspective simplifies this by instead looking at fixed points in space, and describing the velocity of fluid elements along an infinitesimally small volume or area. Fundamentally, the main difference is that in the Lagrangian approach one tracks individual fluid elements, while in the Eulerian one looks at how the flow properties at fixed spatial positions. Eulerian perspective is generally simpler and more straightforward to use, which is why it is the more common approach. The Lagrangian perspective can be more useful for certain applications, such as when tracking the trajectory of a fluid particle.

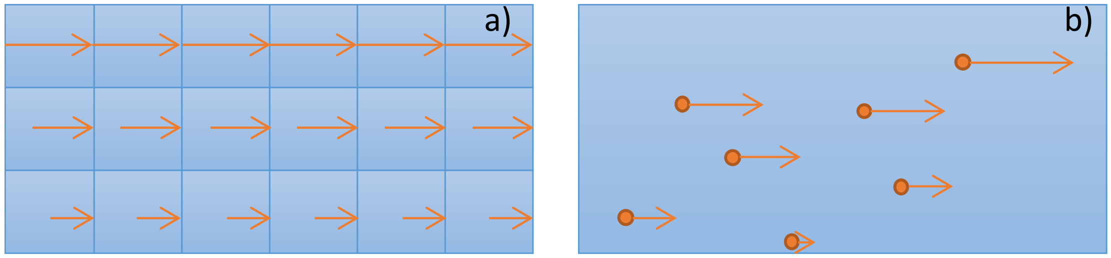


**Figure 2.9:** Sketch comparing the Eulerian description of a fluid flow a) and Lagrangian description b). The Eulerian perspective of fluid flow describes the properties of the fluid at a fixed point in space, whereas the Lagrangian perspective describes the properties of the fluid at a fixed point in time, following the motion of individual fluid particles.

### 2.3.1 Generalized Lagrangian Mean

The Generalized Lagrangian Mean (GLM) is a technique that was developed in [41, 42] to calculate a Lagrangian velocity field for time-periodic flows, such as that of ocean waves. This method assumes that particles follow the flow perfectly, i.e. the Stokes number is zero and utilizes the equation

$$u_d \approx \overline{\int u(x,y,t)\partial t \frac{\partial u(x,y,t)}{\partial x} + \int v(x,y,t)\partial t \frac{\partial u(x,y,t)}{\partial x}} \tag{2.6}$$

and

$$v_d \approx \overline{\int v(x,y,t)\partial t \frac{\partial v(x,y,t)}{\partial y} + \int u(x,y,t)\partial t \frac{\partial v(x,y,t)}{\partial y}}. \tag{2.7}$$

This technique is useful to track the paths of particles over a period of time and generate a field description. Figure 2.10 provides a sketch of the difference between the GLM and the full Lagrangian path. This technique will be important for the Lagrangian analysis in a later section.

Given that the GLM is a vector field, I define the GLM velocity field in $x$ and $y$ as

$$U_{\text{Lag}} =< u_{\text{d}}, v_{\text{d}} >, \tag{2.8}$$

where $u_{\mathrm{d}}$ is the GLM velocity in $x$ and $v_{\mathrm{d}}$ is the GLM velocity in $y$. It will be useful for later sections to define the mean value of $u_{\mathrm{d}}$ as

$$u_{\mathrm{dm}} = \bar{u_{\mathrm{d}}}. \tag{2.9}$$

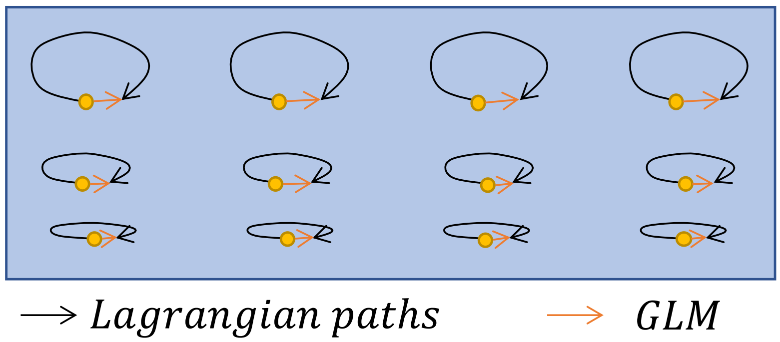


**Figure 2.10:** Sketch of a fluid with a flow, particles in the flow are sketched as the yellow circles. The black lines indicate the Lagrangian path a particle takes over one period. The generalized Lagrangian mean of the particles is shown by the orange vectors.

The Generalized Lagrangian Mean is a simplified field that indicates the motion of particles in the flow. This is advantageous since it is difficult to obtain the paths of individual particles and to obtain meaningful results without the calculation of paths for the entire domain. The Generalized Lagrangian Mean presents a single velocity field that illustrates the movement of particles in the fluid over successive periods, making it feasible to draw conclusions and apply them to relevant problems.

### 2.3.2 Nondimensionalization of the Governing Equations

The technique of nondimensionalizing the governing equations in fluid mechanics analytic analysis has been commonly employed in order to determine the dominant physics in a system. To do this, I began with the Navier-Stokes equations for an incompressible viscous fluid problem. The equations of motion were given by

$$\frac{\partial U}{\partial t} + U \cdot \nabla U = -\frac{\nabla P}{\rho} + \nu \nabla^2 U, \tag{2.10}$$

where $U$ is the two-dimensional velocity field of the fluid so $U =< u, v >$, $t$ is time, $P$ is the pressure field of the fluid, $\nabla$ is a derivative an operator $< \partial x, \partial y >$, $\rho$ is the density of the fluid, and $\nu$ is the kinematic viscosity of the fluid.

Incompressibility is imposed by the continuity equation, which is

$$\nabla \cdot U = 0. \tag{2.11}$$

Since the model I consider is two-dimensional, as I mentioned in subsection 2.3, I can rewrite equation 2.10 as two equations for each spatial component of $x$ and $y$. The equations are

$$\frac{\partial u}{\partial t} + u\frac{\partial u}{\partial x} + v\frac{\partial u}{\partial y} = -\frac{1}{\rho}\frac{\partial P}{\partial x} + \nu(\frac{\partial^2 u}{\partial x^2} + \frac{\partial^2 u}{\partial y^2}) \tag{2.12}$$

for the $x$ component, where $u$ is the velocity in $x$ of the fluid and

$$\frac{\partial v}{\partial t} + u\frac{\partial v}{\partial x} + v\frac{\partial v}{\partial y} = -\frac{1}{\rho}\frac{\partial P}{\partial y} + \nu(\frac{\partial^2 v}{\partial x^2} + \frac{\partial^2 v}{\partial y^2}) \tag{2.13}$$

for the $y$ component, where $v$ is the velocity in $y$ of the fluid.

At this point, the previous equations simply describe the physics of some fluid without specifying much. In order to apply these equations to my study of peristaltic pumping, I must define the boundary conditions. One notable aspect is that there is no forcing term in equations 2.12 or equation 2.13. The driving mechanism is defined by the boundary conditions. Going back to figure 2.7, it is easy to describe the boundary condition at the stationary wall. The boundary conditions at the non-moving wall is a no-slip condition defined as

$$U(x, 0) =< 0, 0 > . \tag{2.14}$$

The ends at $x = 0$ and $x = \lambda$ are treated as periodic boundary conditions. This is to further simplify the problem and treat the system as an infinite wave train, in other words, the domain is infinitely long in $x$ and the traveling wave spans the entire infinite domain. While real-world peristaltic pumps have finite lengths, I can significantly simplify the problem by concentrating on the fluid motion within one wavelength if I consider an infinite train of waves. From this simplification, one can expect the flow to be periodic in nature over the scale of a wavelength. The periodic boundary condition is described as

$$U(0, y) = U(\lambda, y). \tag{2.15}$$

Describing the last boundary condition of the deforming wall is more complicated. The deformation is traveling across the deformable wall with some direction in $x$ over time $t$. Applying this to my simple model from figure 2.7, I can describe the deformation of the wall by using its position. Thus, let $\eta(x, t)$ be a function that describes the displacement of the wall from the nondeformed state. Using this definition, I can describe the position of the deformed wall as $y = L + \eta(x, t)$.

From this, I can easily determine that the deformable wall is imposing a vertical velocity condition as

$$v(x, L + \eta(x, t)) = \frac{\partial \eta(x, t)}{\partial t}. \tag{2.16}$$

The remaining component to describe is the horizontal velocity at the deformable wall. For the purposes of this study I treat it as

$$u(x, L + \eta(x, t)) = 0. \tag{2.17}$$

However, this may not always be the case. Note that in the real world as the flexible wall is deformed from the undeformed position, the total length of the wall changes. This would impose an additional velocity component parallel to the shape of the wall. Figure 2.11 visually demonstrates how this effect is present.

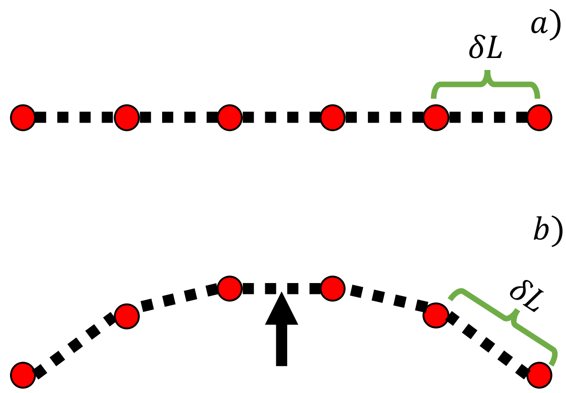


**Figure 2.11:** Sketch demonstrating stretching effects on a wall using a discretized flexible line, where I separate each part into segments of length $\delta L$. a) An unstretched line. All segments that compose the discretized line are of length $\delta L$. b) If I stretch the line it becomes clear that $\delta L$ cannot remain constant, it must have gained some length $\delta S$. This added distance has a component in $x$ and $y$. This added component can add a boundary condition if significant enough when considering peristalsis.

If a line goes from $x = 0, y = 0$ to $x = M_1, y = 0$, I would then know the length of such a line is $M_1$. Now, say I deform it with the function $\eta(x,t)$, such that its position is described as $y = \eta(x,t)$ from $x = 0$ to $x = M_1$. An infinitesimal segment of the line is defined by

$$\delta M_{\text{deformed}} = \sqrt{\delta x^2 + \delta y^2}, \tag{2.18}$$

where $\delta x$ and $\delta y$ are infinitesimal segments in the $x$ and $y$ components. Then it would follow that the way to calculate the total length of the line is given by

$$M_{\text{deformed}} = \int_0^{M_1} \sqrt{1^2 + \frac{\partial \eta(x,t)^2}{\partial x}} dx. \tag{2.19}$$

While the previous equation yields exact results to tell us how much the line has stretched, it can be impossible to solve, depending on the function $\eta(x,t)$. To estimate the impact of this effect let us simplify to consider only the relevant scales at play. I am displacing the wall approximately a distance $A$ over a length

$\lambda$, at a frequency $f$. Then the estimated velocity induced by stretching would be given by

$$S_{\text{vel}} = (\lambda - \sqrt{\lambda^2 + A^2})f. \tag{2.20}$$

Since $\lambda \gg L \gg A$ for the cases I consider, I find that the stretching velocity is negligible ($S_{vel} \approx 0$), and so the boundary condition in equation 2.17 is adequate. Having defined the problem, let us move on to finding a solvable case where I consider simple conditions. Although there are various forms of periodic functions that are admissible here, first I consider the simplest case of a traveling sinusoidal wave. To begin, $\eta$ is defined as

$$\eta = A\cos(\frac{2\pi}{\lambda}x - \frac{2\pi c}{\lambda}t). \tag{2.21}$$

Since $\eta(x,t)$ describes the position of the wall, it must push an amount of fluid equal to the area it moves to conserve the incompressibility of the fluid. As a consequence the boundary condition (equation 2.16) of the governing equations is defined by

$$v(x, y = L + \eta) = \frac{\partial \eta}{\partial t}. \tag{2.22}$$

The former, along with equations 2.14, 2.15 and 2.17, are all the boundary conditions required to model a two-dimensional peristaltic flow. Now, I proceed with the nondimensionalization. I decided to nondimensionalize the variables of the governing equations as shown in Table 2.1. It is important to note that the nondimensionalization of the velocity is done by using the mean displacement velocity of the boundary over one cycle, which differs from previous studies, such as the ones by Shapiro et al. [19], and Yin and Fing [34].

The parameters that describe the system are $A$, $L$, $\lambda$, $c$, $\nu$, and $P$. Thus, three nondimensional numbers should be able to characterize the system. From the nondimensionalization it will be clear that the important numbers are the ratio of wavelength to gap width $\frac{\lambda}{L}$, the amplitude ratio $\frac{A}{L}$, and a Reynolds number $\frac{4AcL}{\nu\lambda}$.

| Dimensional variable | $x$ | $y$ | $u$ | $v$ | $t$ |
|---|---|---|---|---|---|
| Nondimensional variable | $\frac{x}{\lambda}$ | $\frac{y}{L}$ | $\frac{u\lambda}{4Ac}$ | $\frac{v\lambda}{4Ac}$ | $\frac{tc}{\lambda}$ |

**Table 2.1:** Nondimesional form of the variables.

Plugging the nondimensionalization picks into the Navier-Stokes equations (equations 2.12 and 2.13) gives

$$\frac{4Ac^2}{\lambda^2}\frac{\partial u}{\partial t} + \frac{16A^2c^2}{\lambda^3}u\frac{\partial u}{\partial x} + \frac{16A^2c^2}{\lambda^2 L}v\frac{\partial u}{\partial y} = -\frac{1}{\rho\lambda}\frac{\partial P}{\partial x} + \nu(\frac{4Ac}{\lambda^3}\frac{\partial^2 u}{\partial x^2} + \frac{4Ac}{\lambda L^2}\frac{\partial^2 u}{\partial y^2}) \tag{2.23}$$

for the $x$ direction and

$$\frac{4Ac^2}{\lambda^2}\frac{\partial v}{\partial t} + \frac{16A^2c^2}{\lambda^3}u\frac{\partial v}{\partial x} + \frac{16A^2c^2}{\lambda^2 L}v\frac{\partial v}{\partial y} = -\frac{1}{\rho L}\frac{\partial P}{\partial y} + \nu(\frac{4Ac}{\lambda^3}\frac{\partial^2 v}{\partial x^2} + \frac{4Ac}{\lambda L^2}\frac{\partial^2 v}{\partial y^2}) \tag{2.24}$$

for the $y$ direction.

One can simplify the resulting equations by multiplying by $\frac{\lambda^2}{16A^2c^2}$. The result is

$$\frac{1}{4A}\frac{\partial u}{\partial t} + \frac{1}{\lambda}u\frac{\partial u}{\partial x} + \frac{1}{L}v\frac{\partial u}{\partial y} = -\frac{\lambda^2}{16A^2c^2\rho\lambda}\frac{\partial P}{\partial x} + \nu(\frac{1}{4Ac\lambda}\frac{\partial^2 u}{\partial x^2} + \frac{\lambda}{4AcL^2}\frac{\partial^2 u}{\partial y^2}) \tag{2.25}$$

for the $x$ direction and

$$\frac{1}{4A}\frac{\partial v}{\partial t} + \frac{1}{\lambda}u\frac{\partial v}{\partial x} + \frac{1}{L}v\frac{\partial v}{\partial y} = -\frac{\lambda^2}{16A^2c^2\rho\lambda}\frac{\partial P}{\partial x} + \nu(\frac{1}{4Ac\lambda}\frac{\partial^2 v}{\partial x^2} + \frac{\lambda}{4AcL^2}\frac{\partial^2 v}{\partial y^2}) \tag{2.26}$$

for the $y$ direction.

At this point, I pick a length scale to finish the nondimensionalization. The important thing to note is that different multiplications will lead to different insights onto how the governing equations behave. For the purposes of studying our problem, I multiply by L which yields

$$\frac{L}{4A}\frac{\partial u}{\partial t} + \frac{L}{\lambda}u\frac{\partial u}{\partial x} + \frac{1}{1}v\frac{\partial u}{\partial y} = -\frac{\lambda L}{16A^2c^2\rho}\frac{\partial P}{\partial x} + \nu(\frac{L}{4Ac\lambda}\frac{\partial^2 u}{\partial x^2} + \frac{\lambda}{4AcL}\frac{\partial^2 u}{\partial y^2}) \tag{2.27}$$

for the $x$ direction and

$$\frac{L}{4A}\frac{\partial v}{\partial t} + \frac{L}{\lambda}u\frac{\partial v}{\partial x} + \frac{1}{1}v\frac{\partial v}{\partial y} = -\frac{\lambda^2}{16A^2c^2\rho}\frac{\partial P}{\partial y} + \nu(\frac{L}{4Ac\lambda}\frac{\partial^2 v}{\partial x^2} + \frac{\lambda}{4AcL}\frac{\partial^2 v}{\partial y^2}) \quad (2.28)$$

for the $y$ direction.

In this form one can reduce the terms with the following assumption $\lambda >> L$. This restricts the equation to cases where the wavelength scale must be significantly higher than that of the channel gap. The simplified equations are

$$\frac{L}{4A}\frac{\partial u}{\partial t} + \frac{1}{1}v\frac{\partial u}{\partial y} = -\frac{\lambda L}{16A^2c^2\rho}\frac{\partial P}{\partial x} + \nu(\frac{\lambda}{4AcL}\frac{\partial^2 u}{\partial y^2}) \quad (2.29)$$

for the $x$ direction and

$$\frac{L}{4A}\frac{\partial v}{\partial t} + \frac{1}{1}v\frac{\partial v}{\partial y} = -\frac{\lambda^2}{16A^2c^2\rho}\frac{\partial P}{\partial y} + \nu(\frac{\lambda}{4AcL}\frac{\partial^2 v}{\partial y^2}) \quad (2.30)$$

for the $y$ direction.

Inspection of equations 2.29 and 2.30 demonstrated the following properties of the system. The nondimensional equations show that the nonlinear term scaled with the amplitude, while the viscous terms were reduced to include only the $y$ derivatives. This reduction was reasonable, considering that a long wavelength indicated that the shearing effect of the change in vertical velocity occurred over a long distance, thus playing a significantly lesser role than the shear induced by the no-slip boundary conditions due to the channel dimensions. With improved knowledge of the dominant physics of the problem, I proceeded to devise a mathematical solution that modeled the dominant physics of peristalsis for conditions found in the inner ear.

### 2.3.3 Mean Pressure Rise

An important characteristic of peristaltic pumping, which is discussed in previous literature such as [32], is the mean pressure rise per wavelength. The mean pressure rise per wavelength is defined as

$$\Delta P_\lambda = \int_x^{\lambda+x} \frac{\partial P}{\partial x} dx. \tag{2.31}$$

As noted by Shapiro et al. [19], the value of $\Delta P_\lambda$ heavily dictates the behavior of pumping. To better understand the physical implications of the mean pressure rise per wavelength, I created the sketches found in figure 2.12. In the case of peristaltic pumping, the flow must experience a periodic pressure differential. So, if one assumes the pressure gradient is purely sinusoidal over space, then it follows that $\Delta P_\lambda = 0$.

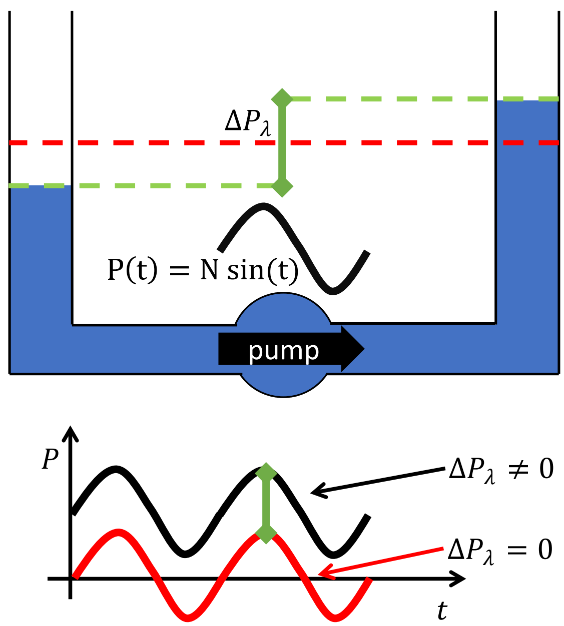


**Figure 2.12:** A sketch of a peristaltic pump pushing fluid. The pump is connected to two reservoirs, which are in hydrostatic pressure balance when the pump is off. When the pump is turned on if the hydrostatic balance level of each reservoir will depend on $\Delta P_\lambda$. The bottom sketched graph demonstrates the effect of having $\Delta P_\lambda \neq 0$, where the pressure function is shifted by a constant, which explains why the equilibrium height of the reservoir is changed from the $\Delta P_\lambda = 0$ case.

What this means from a physical standpoint, is that since a peristaltic pump can generate flows in two directions in $x$, it can effectively pump fluid to meet a specific pressure gradient. After that point, the fluid volume will not travel any further but still be oscillated back and forth around a mean. To visualize this effect see figure 2.13.

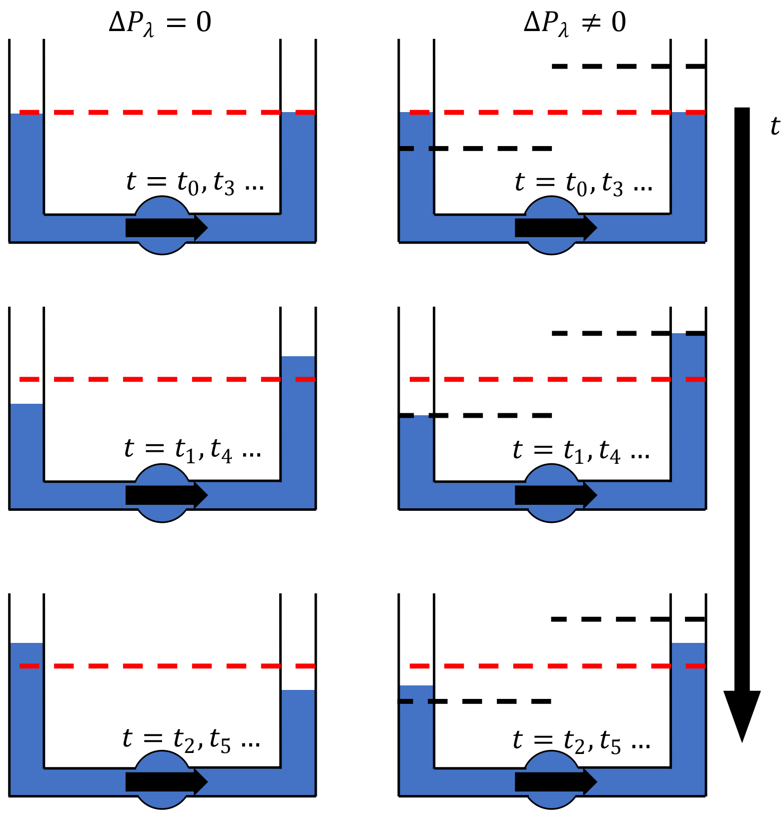


**Figure 2.13:** A sketch based on the same setup as figure 2.12 that compares two peristaltic pumps. The pressure $P$ is oscillatory in nature, and one sees a system where $\Delta P_\lambda \neq 0$ and one where $\Delta P_\lambda = 0$. The big difference is that the equilibrium pressure from the inlet reservoir (the left side of the pump) with the outlet reservoir (the right side of the pump) is different when $\Delta P_\lambda \neq 0$. $t$ indicates time, where subscripts are points further in time. Since the flow is oscillatory, the behavior is repeated every three indices in this example, i.e. $P(t_1) = P(t_4) = P(t_7)$.

For the purposes of my study, I only considered the case of $\Delta P_\lambda = 0$, which as indicated by Eckstein et al. [43] would appear to defeat the point of pumping. However, the main interest in my applications is not to pump fluid, but to mix a fluid. As I stated earlier, even if fluid is not pumped in the sense that a net flow over time is achieved, it is still creating a flow that can have transport characteristics that lead the channel to be mixed.

# 3 Analytic Approach to Modeling Peristaltic Flows in the Inner Ear

## 3.1 Analytic Approach

In this section, I will describe how I developed an analytic model for peristaltic flows considering the conditions that are typically found in the inner ear. Building upon the nondimensionalization outlined in the previous section, I will establish the groundwork for my analysis. This approach will allow me to simplify the physics and find a solution to the governing equations. To accomplish this, I will leverage the physical attributes of the inner ear, which motivated this analysis as discussed in section 1.1.

Previous in-vivo studies of the inner ear have shown measurements of flow and channel deformations [20]. Using measurements from in-vivo studies, I estimated the relevant physical parameters for the fluid system. Table 3.1 is a comprehensive list of the parameters relevant to the study. I estimated the flow of the inner ear to lie in the regime of High Reynolds number ($Re > 100$) flows as the wave speed has been measured to be in the range of 1 m/s to 200 m/s. This is important to note, as it is relevant for the first simplification in my analytic method.

| Parameter | Tunnel of Corti | Experimental Setup |
|---|---|---|
| Wave speed $c$ | $1-200$ m/s | $0.05-2$ m/s |
| Cross-stream length of channel $L$ | 50 $\mu$m | 2.54 cm |
| Stream-wise length of channel | 10 mm | 91.44 cm |
| Amplitude $A$ | $50-500$ nm | $0.13-1.3$ mm |
| Wavelength $\lambda$ | $50-5000$ $\mu$m | $4-30$ cm |

**Table 3.1:** Comparison of the tunnel of Corti dimensions and parameters with the experimental. The tunnel of Corti ranges are estimated from observational studies, the experimental range is the range the system is capable of producing while being within the same Reynolds number range of the real system.

### 3.1.1 Solution for a Traveling Sine Wave

I proceed to develop an analytic solution to the problem. I can now combine the simplified equations (equations 2.29 and 2.30) from the nondimensionalization using a streamfunction where $\frac{\partial\psi}{\partial x}=v$, $\frac{\partial\psi}{\partial y}=-u$, and the vorticity $W=\frac{\partial v}{\partial x}-\frac{\partial u}{\partial y}$

$$\begin{gathered}\frac{\partial^3\psi}{\partial^2 x\partial t}+\frac{\partial^3\psi}{\partial^2 y\partial t}+\frac{\partial^2\psi}{\partial^2 x}\frac{\partial^2\psi}{\partial x\partial y}+\frac{\partial\psi}{\partial x}\frac{\partial^3\psi}{\partial^2 x\partial y}\\ +\frac{\partial^2\psi}{\partial x\partial y}\frac{\partial^2\psi}{\partial y^2}+\frac{\partial^2\psi}{\partial x\partial y}\frac{\partial^3\psi}{\partial^3 y}=-\nu(\frac{\partial^4\psi}{\partial^2 x\partial^2 y}+\frac{\partial^4\psi}{\partial^4 y})\end{gathered} \tag{3.1}$$

I can neglect the nonlinear terms as they are higher-order terms from my nondimensionalization. I eliminate the time derivative by using a coordinate shift to the wave speed and assuming the flow to be steady in the moving frame. Thus using a coordinate transformation where $\mathbf{x}=x-\frac{\omega}{\alpha}t$, where $\mathbf{x}$ is the $x$ coordinate in the moving frame, I can dramatically simplify the equations of motion to

$$\frac{\partial^4\Psi}{\partial^2\mathbf{x}\partial^2 y}+\frac{\partial^4\Psi}{\partial^4 y}=0 \tag{3.2}$$

where $\Psi$ is the streamfunction in the moving frame, such that $\Psi(\mathbf{x},y)$. Note that the problem has become viscosity independent. This is the problem to solve where

I specify a series of constraints (boundary conditions)

$$\frac{\partial \Psi}{\partial \mathbf{x}}(\mathbf{x}, L) = A\omega \sin(\alpha \mathbf{x}), \tag{3.3}$$

$$\frac{\partial \Psi}{\partial \mathbf{x}}(\mathbf{x}, 0) = 0, \tag{3.4}$$

$$\Psi(0, y) = \Psi(\lambda, y), \tag{3.5}$$

$$\Delta\Psi(0, y) = \Delta\Psi(\lambda, y) \tag{3.6}$$

To solve this problem I will assume that the flow must be irrotational, such that

$$\frac{\partial^2 \Psi}{\partial^2 \mathbf{x}} + \frac{\partial^2 \Psi}{\partial y^2} = 0. \tag{3.7}$$

Now I try to find a solution to equation 3.2 by assuming that $\Psi$ is a separable equation such that it can be rewritten as

$$\Psi(\mathbf{x}, y) = X(\mathbf{x})Y(y) \tag{3.8}$$

This means equation 3.2 can be rewritten as

$$\frac{d^2X}{d\mathbf{x}^2}(\mathbf{x})\frac{d^2Y}{dy^2}(y) + X(\mathbf{x})\frac{d^4Y}{dy^4}(y) = 0 \tag{3.9}$$

At this point, I can proceed with solving the problem, which happens to be a typical separable partial differential equation problem encountered at the undergraduate level. For additional detail on the method see [44]. The separable equation tells us that

$$-\frac{\frac{d^2X}{d\mathbf{x}^2}(\mathbf{x})}{X(\mathbf{x})} = \frac{\frac{d^4Y}{dy^4}(y)}{\frac{d^2Y}{dy^2}(y)} = \mu, \tag{3.10}$$

where $\mu$ is a constant. The general solution equation 3.10 of the problem can then be split into the $\mathbf{x}$ and $y$ parts, for which the general solutions to their respective differential equations are

$$X(\mathbf{x}) = \theta_a sin(\mu \mathbf{x}) + \theta_b cos(\mu \mathbf{x}) \tag{3.11}$$

and

$$Y(y) = \theta_1 + \theta_2 y + \theta_3 e^{-\mu y} + \theta_4 e^{\mu y}. \tag{3.12}$$

where the $\theta$ terms are constants. Boundary condition 3.3 imposes a strong constraint that will simplify the problem significantly.

$$\frac{dX}{d\mathbf{x}}(\mathbf{x})Y(L) = A\omega sin(\alpha\mathbf{x}) = (\mu\gamma_1 cos(\mu\mathbf{x}) + \mu\gamma_2 sin(\mu\mathbf{x}))Y(L) \tag{3.13}$$

The only way this equation can be satisfied is if $\gamma_2 = 0$ and $\mu = \alpha$. This simplifies the problem to

$$X(\mathbf{x})Y(y) = (\theta_1 + \theta_2 y + \theta_3 e^{-\alpha y} + \theta_4 e^{\alpha y})cos(\alpha\mathbf{x}) \tag{3.14}$$

The next constraint I apply is irrotation, so equation 3.14 must satisfy equation 3.7.

$$\begin{aligned}\frac{d^2X}{d\mathbf{x}^2}(\mathbf{x})Y(y) + X(\mathbf{x})\frac{dY^2}{dy^2}(y) = -\alpha^2(\theta_1 + \theta_2 y + \theta_3 e^{-\alpha y} \\ +\theta_4 e^{\alpha y})cos(\alpha\mathbf{x}) + \alpha^2(\theta_3 e^{-\alpha y} + \theta_4 e^{\alpha y})cos(\alpha\mathbf{x}) = 0\end{aligned} \tag{3.15}$$

Which can be simplified to

$$\frac{d^2X}{d\mathbf{x}^2}(\mathbf{x})Y(y) + X(\mathbf{x})\frac{dY^2}{dy^2}(y) = -\alpha^2(\theta_1 + \theta_2 y) = 0 \tag{3.16}$$

The only way to satisfy this condition then is for $\theta_1$ and $\theta_2$ to be zero. Thus I can further simplify the stream function to

$$X(\mathbf{x})Y(y) = (\theta_3 e^{-\alpha y} + \theta_4 e^{\alpha y})\cos(\alpha\mathbf{x}) \tag{3.17}$$

Now by applying boundary conditions 3.3 and 3.4 I obtain a final form of

$$\Psi(\mathbf{x}, y) = -\frac{e^{\alpha L - \alpha y}\cos(\alpha\mathbf{x})\left(Aw - \frac{Awe^{2\alpha L}}{e^{2\alpha L}-1}\right)}{\alpha} - \frac{Awe^{\alpha L + \alpha y}\cos(\alpha\mathbf{x})}{\alpha\left(e^{2\alpha L} - 1\right)}. \tag{3.18}$$

The final step is to transform back to the stationary frame, where I obtain the following simplified equation using some trigonometric identities

$$\psi(x, y, t) = -\frac{A\omega\text{csch}(\alpha L)\sinh(\alpha y)\sin(\alpha x - t\omega)}{\alpha}. \tag{3.19}$$

This streamfunction (Eq. 3.19) is a solution for modeling peristaltic for a sine wave deformation. However, this solution does not take into account viscosity, this does not mean it is a bad model, but it is particularly a bad model if I care about the characteristics of the flow near the no-slip boundaries or if the Reynolds number is low ($Re < 1$). As such the next step in creating the model is to implement a correction to the solution which will be able to capture the viscous effects.

### 3.1.2 Viscous correction

To implement the viscous effects into the solution, let me first split the solution in streamfunction form into the two-dimensional velocity components,

$$u(x, y, t) = A\omega \text{csch}(\alpha L) \cosh(\alpha y) \sin(\alpha x - t\omega) \tag{3.20}$$

$$v(x, y, t) = -A\omega \text{csch}(\alpha L) \sinh(\alpha y) \cos(\alpha x - t\omega) \tag{3.21}$$

Based on the results of the nondimensionalization in section 2.3.2, specifically equations 2.29 and 2.30, I determined that for long wavelengths $L_\lambda \gg 1$, the viscous component in the $y$ direction is considerably less significant compared to that in the $x$ direction. Thus, for the purposes of the model, I can prioritize adding the effects of viscosity in $x$ and neglecting those in $y$. Inspecting equation 3.20, one can see that the flow at some position in $x$, is periodic in $t$ and has some velocity profile $y$ in the $x$ direction. This mathematical description is similar to Stokes second problem ([45]). Recognizing this similarity, the next step is to split the problem in two. I want to locally solve for the viscous effects near the top and bottom of the velocity profile. Figure 3.1 will serve as a visual guide for this mathematical approach.

If I only consider the local problem at the boundary, I can treat it as a flow profile oscillating due to a pressure gradient near a plate. This problem has a well established analytic solution. First, one must recognize the governing equation for this section of the flow is

$$\frac{\partial u}{\partial t} = \nu \frac{\partial^2 u}{\partial y^2}, \tag{3.22}$$

which is similar to equation 2.12, but I only keep the viscous term and linear velocity term. This is what one would expect of a simple viscous flow. The boundary conditions relevant to the localized problem I am are the $x$ components for the no-slip boundary conditions described by equation 2.14.

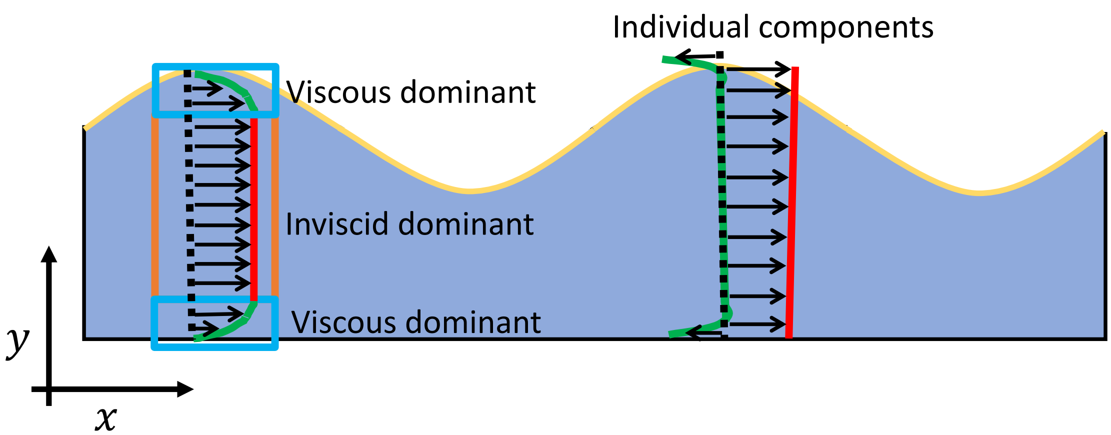


**Figure 3.1:** Shown is a sketch of velocity profiles for a channel that has a peristaltic flow. The velocity profiles are divided into the respective analytic models. Shown in red is an example velocity profile of the inviscid component of $u$. In green are two example velocity profiles of the local viscous component of $u$. The left velocity profile sketch indicates how the superpositioned velocities produce a complete modeled velocity, while the right one splits the components and shows each example velocity profile would look like individually.

Taking the $u$ velocity values at $y = L$ and $y = 0$ now gives the boundary conditions to solve this localized problem. It follows, that the local solution must be equal to the velocity given the inviscid solution as I move away from the boundary. To better illustrate this point let us first solve the problem near $y = 0$. In the vicinity of this boundary, the boundary conditions governing the local problem can be expressed as

$$u_a(x, 0, y) = 0,\ u_a(x, \infty, t) = u(x, 0, t) \tag{3.23}$$

where I label $u_a$ as the velocity for the localized model near $y = 0$. Now I must seek a form for $u_a(x, y, t)$ which satisfies equation 3.22. The solution in this specific case is

$$u_a(x, y, t) = u(x, 0, t)e^{\sqrt{-\frac{\omega}{2\nu}}y}\cos(\omega t - \sqrt{\frac{\omega}{2\nu}}y). \tag{3.24}$$

Equation 3.24 gives a solution that describes the flow near the boundary.

The process for solving the other local region where viscosity is dominant is similar. The solution for the velocity $u_b$ near $y = L$ is

$$u_b(x, L, y) = 0,\ u_b(x, -\infty, t) = u(x, L, t). \tag{3.25}$$

Now that I have the two local regions, I must bring them together to form one single general solution for the entire system. To do this I will superposition both solutions.

$$u_f(x, y, t) = u(x, y, t) + (u_a(x, y, t) - u(x, 0, t)) - (u_b(x, y, t) - u(x, L, t)) \tag{3.26}$$

Equation 3.26, is a superposition of the local viscous solutions and the inviscid solution. While the local solutions have boundaries at infinite points in $y$, the local solution converges to the value exponentially. I can describe a characteristic length scale $\delta_{BL}$ as

$$\delta_{BL} = \sqrt{\frac{2\nu}{\omega}}. \tag{3.27}$$

It is possible to rewrite $\delta_{BL}$ in terms of the Reynolds number as

$$\delta_{BL} = \sqrt{\frac{L^2}{\pi Re}}. \tag{3.28}$$

Equation 3.28 shows that as the Reynolds number increases the length scale of the viscous section decays rapidly. Dividing by $L$ I can obtain a ratio of the scale of the channel to the viscous length scale,

$$\frac{\delta_{BL}}{L} = \sqrt{\frac{1}{\pi Re}}. \tag{3.29}$$

Given that I only consider cases where the Reynolds number is high, i.e. $Re \gg 1$, then the viscous region will always be a small portion (at a maximum 15%, i.e. $Re \approx 10$) of the domain as indicated by equation 3.29.

At this point, I have a corrected velocity in the $x$ direction, but I am still missing a corrected velocity in $y$. To obtain the corrected velocity I use the continuity equation (equation 2.11). Given that $u$ is known, now as $u_f$, I can integrate and apply boundary conditions to obtain a corrected velocity $v_f$ in the $y$ direction.

$$\int \frac{\partial u_f}{\partial x} \partial y = \int \frac{\partial v_f}{\partial y} \partial y = v_f + \mathbf{E}, \tag{3.30}$$

where $\mathbf{E}$ is constant that is obtained by reapplying the no penetration boundary condition at $y = 0$ (equation 3.4) of the problem. substituting for the equations in the case of a sinusoidal wave boundary condition, equation 3.30 yields

$$\begin{aligned} v_f(x,y,t) = A\omega \text{csch}(\alpha L)\text{sinh}(\alpha y)\text{cos}(\alpha x - t\omega) \\ + \frac{\alpha A \omega}{\sqrt{2}\delta_{BL}}(\coth(\alpha L) e^{\frac{L-y}{\delta_{BL}}} \sin(\frac{\pi}{4} - \frac{L-y}{\delta_{BL}} + t\omega - \alpha x) \\ - \text{csch}(\alpha L) e^{-y/\delta_{BL}} \text{sin}(\frac{\pi}{4} + t\omega - \alpha x - y/\delta_{BL})) + \mathbf{E}, \end{aligned} \tag{3.31}$$

where the constant term due to integration is

$$\begin{aligned} \mathbf{E} = \frac{1}{2}\alpha A \delta_{BL} \omega (\text{csch}(\alpha L) \\ (\cos(\alpha x - t\omega) - \sin(\alpha x - t\omega)) - e^{-\frac{L}{\delta_{BL}}} \coth(\alpha L) \\ (\sin(-\frac{L}{\delta_{BL}} - t\omega + \alpha x) + \cos(-\frac{L}{\delta_{BL}} - t\omega + \alpha x))). \end{aligned} \tag{3.32}$$

Note that the viscous corrected solution will not exactly match the boundary at $v(x, y = L, t)$ (equation 3.3). If I take equation 3.31, and evaluate at $y = L$, one obtains the following result

$$\begin{split} e_{BL} = \\ -\frac{1}{2}A\omega e^{-\frac{L}{\delta_{BL}}}(2e^{L/\delta_{BL}}\cos(\alpha x - t\omega) + \alpha\delta_{BL}\coth(\alpha L)(\cos(\alpha x) - \sin(\alpha x)) \\ (e^{L/\delta_{BL}}\sin(t\omega) - \sin(\frac{L}{\delta_{BL}} + t\omega)) - \alpha\delta_{BL}\text{csch}(\alpha L)(\sin(\alpha x) + \cos(\alpha x)) \\ (e^{L/\delta_{BL}}\sin(t\omega) + \sin(\frac{L}{\delta_{BL}} - t\omega))). \end{split} \tag{3.33}$$

I had expected that the error constant would scale with $\sqrt{\nu\omega^{-1}L^{-2}}$, which is inversely proportional to the Reynolds number. I had anticipated that it would remain small in this model, given that the error scales with $Re$. From my understanding, the source of the error was likely due to implementing the viscous correction. This added viscous correction would have implemented some form of resistance to the flow, or energy drain. The error factor essentially implied that the sine wave needed to be stronger to achieve the flow that was modeled as inviscid. In other words, the error factor was an additional energy input into the system that was necessary to account for the viscous losses in order to match the inviscid solution.

### 3.1.3 Extending the Model to Arbitrary Nondispersive Waveforms

Since I used separation of variables to find a solution to the analytic model, it became evident that I could find solutions to other cases other than the simple sine wave. Upon examining the analytical solution approach, it became clear that the boundary condition outlined in equation 3.3 for the simple sine wave case is represented as a Fourier series in the solution methodology. This boundary condition imposes a specific form on the Fourier series, implying that any waveform that can be expressed as a Fourier series can be solved using this method.

Now I solve for a generalized wave function $Z(\mathbf{x})$, where the solution is defined by the stream function $\psi_g$ and $\Psi_g$ in the moving frame. The boundary condition in the moving frame changes to

$$\frac{\partial \Psi_g}{\partial x}(\mathbf{x}, L) = Z(\mathbf{x}) \tag{3.34}$$

This changes the solution such that the constant term $\mu$ changes to $\mu_n = (\frac{n\pi}{\lambda})^2$. This extends the applicability of the general solution of the sine wave case (equation 3.20) and transforms to

$$\Psi_g = \Gamma_n \mathrm{sin}(\sqrt{\mu_n}\mathbf{x})y + \vartheta_n \mathrm{cos}(\sqrt{\mu_n}\mathbf{x}), \tag{3.35}$$

where the $\Gamma_n$ and $\vartheta_n$ are

$$\Gamma_n = \frac{1}{\pi}\int_0^\lambda Z(\mathbf{x})\mathrm{sin}(\sqrt{\mu_n}\mathbf{x})dx, \vartheta_n = \frac{1}{\pi}\int_0^\lambda Z(\mathbf{x})\mathrm{cos}(\sqrt{\mu_n}\mathbf{x})dx. \tag{3.36}$$

Note that the Fourier series has no constant term given that I have restricted functions to those which are periodic over $\lambda$.

Applying the periodic boundary conditions will simplify to only retain the $\Gamma_n$ term, which can give a generalized solution by letting it be a sum of constants depending.

$$\Psi_g = \Gamma_n \mathrm{cos}(\sqrt{\mu_n}\mathbf{x})\mathrm{csch}(\alpha_n L)\sinh(\alpha_n y), \tag{3.37}$$

for

$$Z(x) = -\sqrt{\mu_n} L \sum_{n}^{1,2...} C_n \mathrm{sin}(\sqrt{\mu_n}\mathbf{x}), \tag{3.38}$$

where $C_n$ is a series of constant terms. Finally giving

$$C_n = \frac{2}{\sqrt{\mu_n}\lambda L}\int_0^\lambda Z(\mathbf{x}) sin(\sqrt{\mu_n}\mathbf{x}). \tag{3.39}$$

Note that this transformation will apply to a single wave speed, this means that when going back into the time-dependent form the frequency must be adjusted to match the wavenumber of the series $\mu_n$. The final generalized analytic solution to the problem is then equal to

$$\Psi_g = \sum_{n}^{1,2...} \frac{A\omega}{\alpha_n L} C_n cos(\alpha_n x - n\omega_n t) \operatorname{csch}(\alpha_n L) \sinh(\alpha_n y). \tag{3.40}$$

With equation 3.40, one can model peristaltic flows for any waveform that is nondispersive with good accuracy, except near the walls. Near the walls, the solution still requires an adjustment to account for the no-slip boundary condition. So far, the solution only works if I assume the flow to be inviscid.

For equation 3.40, it is also possible to implement the viscous effects, although it is somewhat more cumbersome since I have to deal with a long sum of equations. The exact same procedure as the one described in section 3.1.2 for the sinusoidal wave case applies here, where one replaces the term $u(x, y, t)$ from equations 3.22 with the negative derivative in x from equation 3.40 ($-\frac{\partial \Psi_g}{\partial x} = u(x, y, t)$).

Because the generalized solution consists of a sum of wavelengths and frequencies, that means that the viscous component will also have the same frequency summation. As noted in equation 3.27 for the sinusoidal case, one can see that the viscous length scale would consist of multiple wave frequencies in the generalized case, in the same manner as the sum operates having multiple frequencies and wavelengths. Thus one determines the viscous length scale to be

$$\delta_{BL_n} = \sqrt{\frac{2\nu}{\omega_n}}. \tag{3.41}$$

# 4 Experimental Approach to Modeling Peristaltic Flows

This chapter provides a comprehensive overview of the experiment design, construction, and operation utilized to investigate peristaltic flows. To start, I will provide a brief summary of the apparatus, its construction, and its intended purpose.

## 4.1 Experimental Device Overview

The experiment I designed consisted of a square channel where one of the walls was flexible. I filled the channel with water and used an array of actuators to deform the flexible wall. I used the actuators to deform the wall in a periodic manner. The wall deformations would displace the fluid inducing a flow. The induced flow is peristaltic pumping, which I studied for a specific set of parameters. Ultimately the goal was to gain a better understanding of peristaltic flow conditions found in the inner ear, as discussed in chapter 2. Figure 4.1 provides a general overview of the experimental setup.

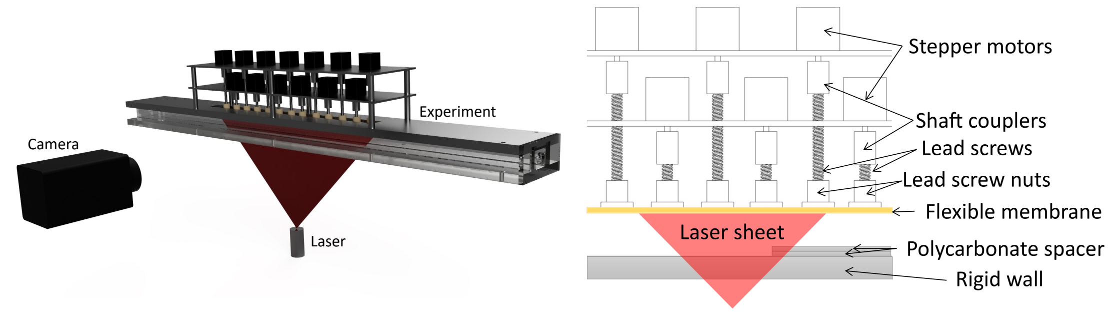


**Figure 4.1:** Left: Rendering of the key components of the experimental setup. Right: Design images of the experimental setup. The side view shows the hardware that makes up the experiment apparatus.

The top wall of the experimental setup was made of flexible rubber with a thickness of 1.6 mm and a durometer of 40A, sourced from McMaster-Carr. The wall was actuated by 14 translation stages, each driven by a stepper motor. The stepper motors were capable of inducing a discrete form of a traveling wave deformation in the rubber wall. The position of each motor was accurately controlled by a combination of MATLAB code and an Arduino board. This setup provided flexibility in capabilities to deform the flexible wall, as any waveform could be induced, and a large range of wavelengths, wave speeds, and amplitudes could be achieved.

The channel gap $L$ was adjustable by inserting polycarbonate sheets to reduce the effective flow region. This reduced the Reynolds number and increased the range of operability for different amplitudes $\epsilon$. The experimental device characteristics are fully detailed in the appendix, chapter A.

## 4.2 Experiment Measurement Techniques

Having established an overview of the experimental setup, in this section I detail the measurement techniques that I used to obtain data from the experimental apparatus.

### 4.2.1 Particle Image Velocimetry

Particle image velocimetry (PIV) is a technique that consists of taking images from a fluid flow where a large number of particles are present. The particles are illuminated so that they are clearly visible in the image. Additionally, particles must have a low Stokes number. A low Stokes number ensures that particles track the flow stream accurately, by ensuring that inertial effects are negligible. The Stokes number is defined by

$$\mathrm{St} = \frac{U_s(\rho_p - \rho)d}{18\nu\rho}, \tag{4.1}$$

where $\rho_p$ is the particle density, $\rho$ is the fluid density, and $U_s$ is a characteristic flow speed. In all instances for this experiment, the Stokes number is small ($St \ll 1$). The Stokes number remains small since the particles I used were of diameter $d = 115.5 \pm 9.5$ $\mu$m and density $\rho_p = 1 \pm 0.01$ g/cc from the manufacturer Cospheric. Since the fluid I used was water in all experiments, the main component dictating the Stokes number is the difference between $\rho_p$ and $\rho$, which are approximately equal, as such $St \approx 0$.

PIV works by taking a section of an image where a large number of particles are present, and determining how they have displaced in the next frame. The determined displacement gives a velocity vector derived from the motion of the set of particles that were in that section of the image. Each image is divided into multiple sections, which all produce a vector, and when combined one can have an experimentally measured velocity field of the flow. After capturing images of particles in the flow by recording videos, I use a MATLAB version of the open-source code PIVlab [46]. The code uses the video image data to produce two-dimensional velocity fields of the flow. These velocity fields allow me to compare analytic and numerical models with ease, and as such, it was my primary tool for experimental measurements over the course of this study.

### 4.2.2 Particle Tracking Velocimetry

Particle tracking velocimetry (PTV) is a similar technique to PIV, however, PTV focuses on tracking the motion of individual particles instead of a set and produces individual particle path data. This is a Lagrangian measurement of the flow. This data is particularly useful for determining material transport in a flow since transport can sometimes be difficult to determine with PIV data alone. The fundamental principle of Particle Tracking Velocimetry (PTV) involves the identification of individual particles and the recording of their positions over time as they move. To obtain these measurements, the MATLAB code, PredictiveTracker, was utilized, as detailed by Kelley and Ouellette in their publication [47].

# 5 Applications and Results

In this chapter, I present the applications of the experimental and analytic approaches with their respective measurements. The first subsection is dedicated to the validation of the experiment and analytic solution when considering high Reynolds number flows. The second subsection focuses on the validation of the experiment in low Reynolds number cases. The third and final subsection focuses on how the validated analytic model can be applied to practical problems, which in my case is modeling mixing in the inner ear.

## 5.1 Validation of the Experimental and Analytic Model

Before I can apply either the analytic or experimental models that I developed directly to modeling flows inside the inner ear, I had to perform a series of experiments that spanned a large parameter range to validate the accuracy of the models. In order to validate the models, I compared my measurements and predictions with other analytic and numerical results.

The first form of comparison I employed for preliminary validation was Yin and Fung's analytic model from [34]. With the help of Yin's dissertation [35], I was able to write up a Matlab code that computed the lengthy analytic solution. In figure 5.1, I show a series of comparisons that I made between experimentally measured values and Yin and Fung's analytic model. For this comparison, I measured the root-mean-square velocity ($V_{\mathrm{rms}}$), as calculated by equation A.6, and compared against three key variables, the wavelength $\lambda$, the wave speed $c$ and the nondimensional amplitude $\epsilon$.

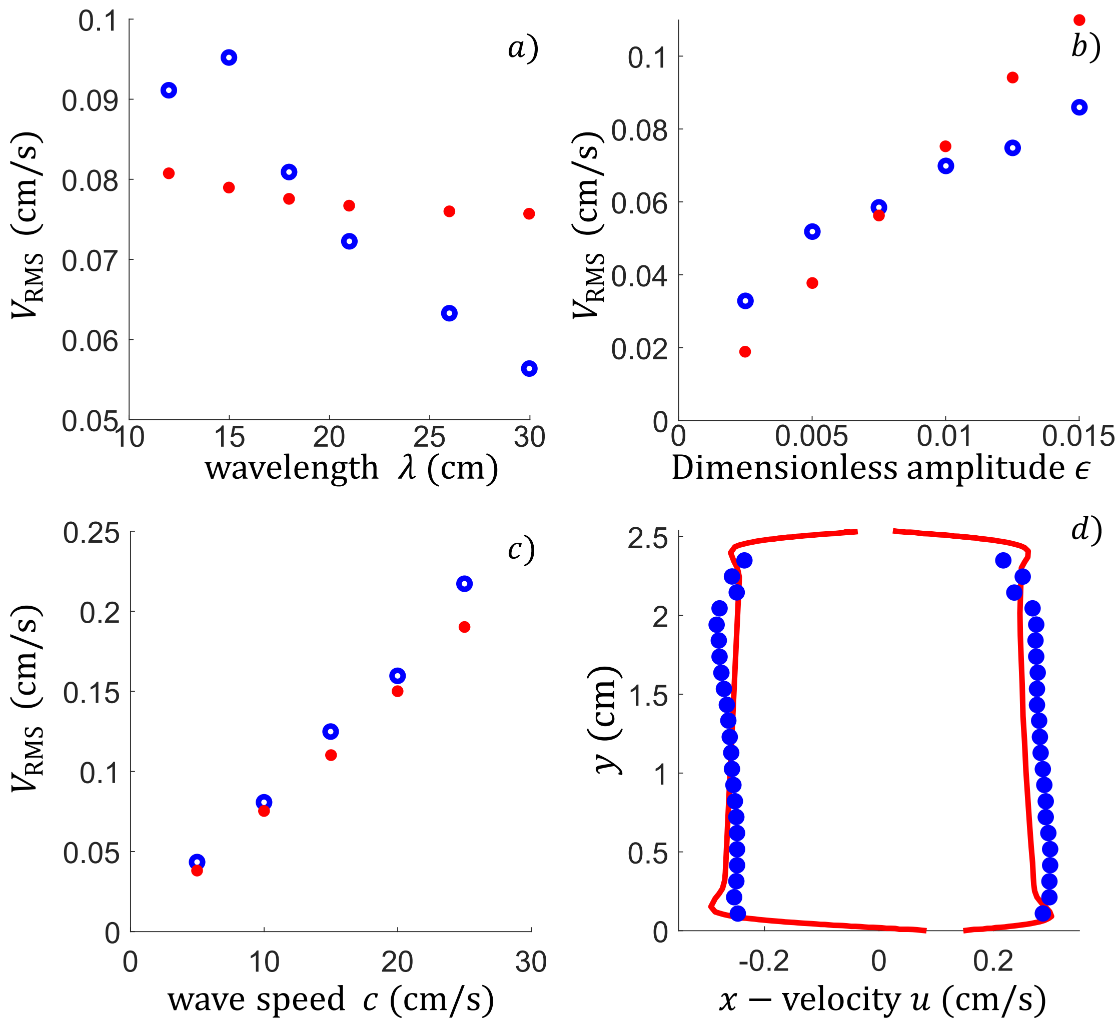


**Figure 5.1:** The figure shows a series of comparisons between the experimentally measured (blue) and analytical model values from Yin and Fung. a) Holding $c = 30$ cm/s and $\epsilon = 0.01$ while varying the wavelength $\lambda$ yielded little change in the root-mean-square velocity of the flow. The experimental values appear to have a small trend but are not significant. Both values are still close in magnitude. b) Holding $c = 30$ cm/s and $\lambda = 30$ cm while varying the amplitude $\epsilon$ shows similar magnitudes of root-mean-square velocity and trends for both the analytic model and experiment. c) Holding $\epsilon = 0.01$ and $\lambda = 30$ cm while varying the wave speed $c$ shows close agreement in magnitudes of root-mean-square velocity and trends for both the analytic model and experiment. d) Comparing the velocity profiles for the velocity in $x$ at a fixed point in space and time from the analytic model and experimentally measured values show good agreement.

The results from comparisons between Yin and Fung's model demonstrated that the experimental model was replicating trends predicted by the analytic model. The wavelength $\lambda$ on its own had little impact on the root-mean-square velocity. The wave speed $c$ and nondimensional amplitude $\epsilon$ had a linear trend with the root-mean-square velocity, where increasing either also increased the root-mean-square velocity. However, I was somewhat limited in how I could apply their analytic model given the limitations that I described earlier. The next step I took was to develop an analytic model which would suit the modeling applications that I was interested in, i.e. those described in section 2.1.

After developing the analytic model I presented in section 3.1, I ran a series of experiments with a large parameter span in order to validate the accuracy of the model. The approach was similar to the one I used previously. I chose a parameter range where I had previously estimated that the analytic model should yield accurate solutions. The parameter range estimate was given by the results from my analysis in section 3.1. It suggested that the analytic model would be accurate for the parameter range that I chose for experimental runs. To start, I consider the simplest case of a traveling wave. As noted in section 3.1, the experimental cases must be at high Reynolds number ($Re \gg 1$), with long wavelengths ($L_\lambda \gg 1$), and small amplitudes ($\epsilon \ll 1$). Given these criteria, I performed experiments with a traveling sine wave defined by the equation

$$\eta(x,t) = A\sin(\alpha x - \omega t). \tag{5.1}$$

To obtain velocity profiles along the length of the channel, I employed PIV measurements as described in chapter 4. The experimentally obtained velocity fields were then compared with analytically derived velocity fields and numerical simulations to ensure the validity of the results.

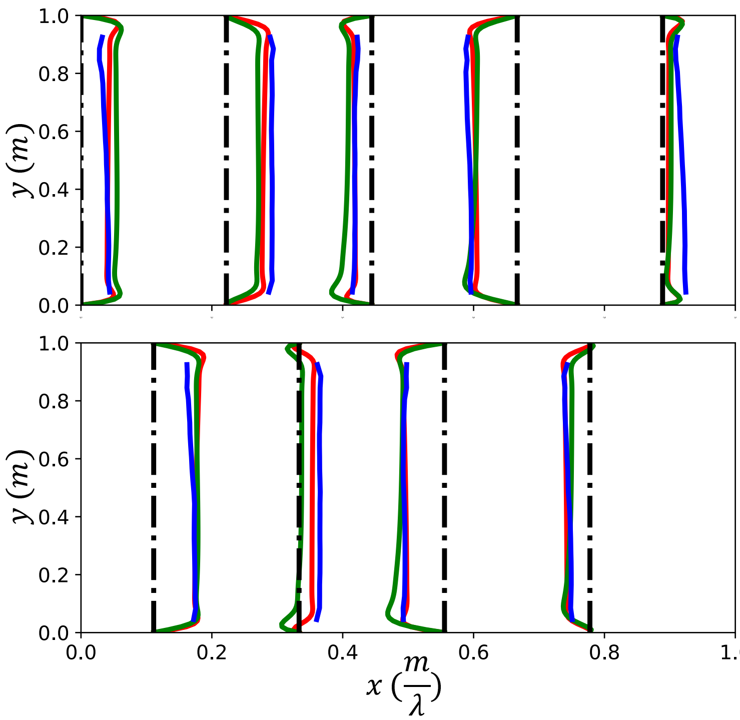


**Figure 5.2:** The figure presented illustrates a comparison of velocity profiles over one wavelength for the given parameters of $\lambda = 30$ cm, $c = 20$ cm/s, and $\epsilon = 0.01$. The velocity profiles are represented by the red line which depicts the analytically predicted velocity profile, the blue line which displays the experimentally measured velocity profile, and the green line which portrays the numerically calculated velocity profile.

The velocity profile from comparison figure 5.2 showed good agreement. The comparison consisted of comparing measured velocities over $y$ at fixed points in $x$ from the experiment, with those expected by the analytic model and from simulations performed by collaborators. For additional validation, I measured the root-mean-squared velocity ($V_{\mathrm{rms}}$) from the experimentally measured velocity field, and did the same three-way comparison between analytic, experimental, and numerical results. Figure 5.3 shows the comparison of the measurements. In the comparison, the nondimensional amplitude was held constant as $\epsilon = 0.01$ and the wavelength at $\lambda = 30$ cm.

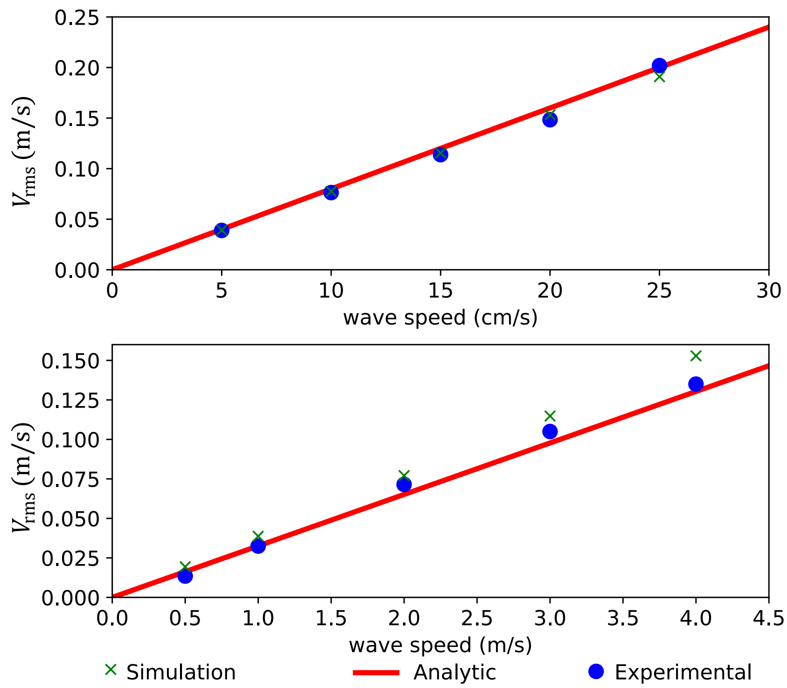


**Figure 5.3:** The root-mean-square velocity (equation A.6) in the bulk flow region was compared between experiments, modeling, and simulations with a constant wavelength of $\lambda = 30$ cm. The comparison was conducted for two values of $\epsilon = 0.01$ (top panel) and $\epsilon = 0.05$ (bottom panel).

As I previously showed in the preliminary analysis using Yin and Fung's method, the resulting root-mean-squared velocity of the experiment shows a linear increase when $c$ is increased for all methods. The methods also yield close results, which suggest that the experimental and analytic model are accurately capturing the dynamics of peristaltic flows.

As discussed in section 3.1, one of the main advantages of my solution over previous analytic solutions, is that it can admit a broader set of waveforms. Different waveforms impose different boundary conditions on the system. I know from equation 3.3, that the waveform imposes a temporal shape (it follows a certain time pattern) on the velocity in $v$, and as such one can expect that the velocity in $u$ follows the same temporal pattern, different from the sinusoidal case. To check for this, I compared experimentally obtained average bulk velocities $(u_{mathrmAB})$

using PIV, and the analytically obtained average bulk velocities. The average bulk velocities are calculated by taking the average in $y$ from $y = 0.05L$ to $y = 0.9L$ of $u$ at a fixed point in $x$. Figure 5.4 shows the comparison of measured and predicted average bulk velocities. The figure clearly shows that the analytic model and experimentally measured quantities are in agreement. Further, it validates that the boundary conditions, as modeled, for non-sinusoidal waveforms are correctly captured. The waveforms I used for validation in figure 5.4 can be described by

$$\eta(x,t) = Ae^{\gamma_g^2(x-\mathrm{mod}(ct,\lambda))^2}, \tag{5.2}$$

$$\eta(x,t) = A\,\mathbf{sawtooth}(\omega(x-ct)) - A/2, \tag{5.3}$$

$$\eta(x,t) = A\omega(\cos(\alpha x) + \sin(4\alpha x) + \sin(2\alpha x)), \tag{5.4}$$

where $\gamma_g$ is a factor that determines the traveling Gaussian curve width, and **sawtooth** is a sawtooth function. Note that the waveforms for the experimental device are input as discrete values on the software discussed in the appendix A.2, and it is possible to create waveforms that are not easily described by mathematical functions, which adds more versatility for applications.

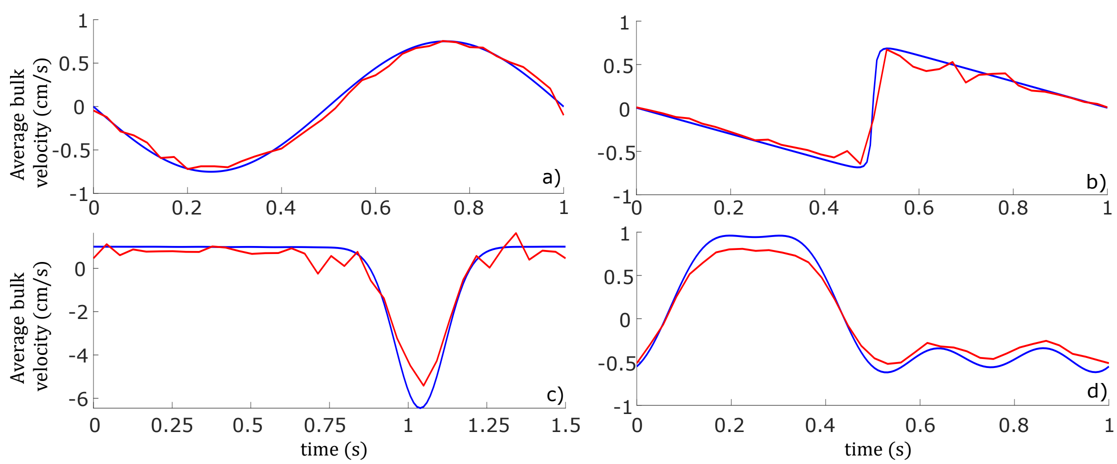


**Figure 5.4:** Average bulk flow velocity in the downstream direction for various deformation waveforms including sinusoid (a), sawtooth (b), Gaussian (c), and complex wave (d). Blue curves show analytic estimates derived using the model from [8]. Red curves show experimentally measured values.

To ensure the applicability and accuracy of the analytic model for its intended purpose of investigating the inner ear's much smaller scale, I compared the model's results to numerical simulations for parameter scales beyond the experimental model's capabilities. This additional validation step was crucial in establishing the model's accuracy and reliability.

To validate the analytic model at the microfluidic scale of the inner ear, I compare analytically predicted vorticity between numerical and analytic results. Figure 5.5 shows an example of the comparison between the two. The vorticity was calculated by taking the numerical derivative of experimentally measured velocity fields, where the vorticity is $W = \frac{\partial v}{\partial x} - \frac{\partial u}{\partial y}$. One can see that there is good agreement between the two as shown by panel c), which is the difference between the two. The slight variations observed can be attributed to differences in the boundary conditions. The numerical simulation was performed on a finite domain, with a wave boundary condition that tapers off in amplitude near the corners of the domain. This was necessary for the simulation to converge, as having non-zero velocities at the corners caused stability problems.

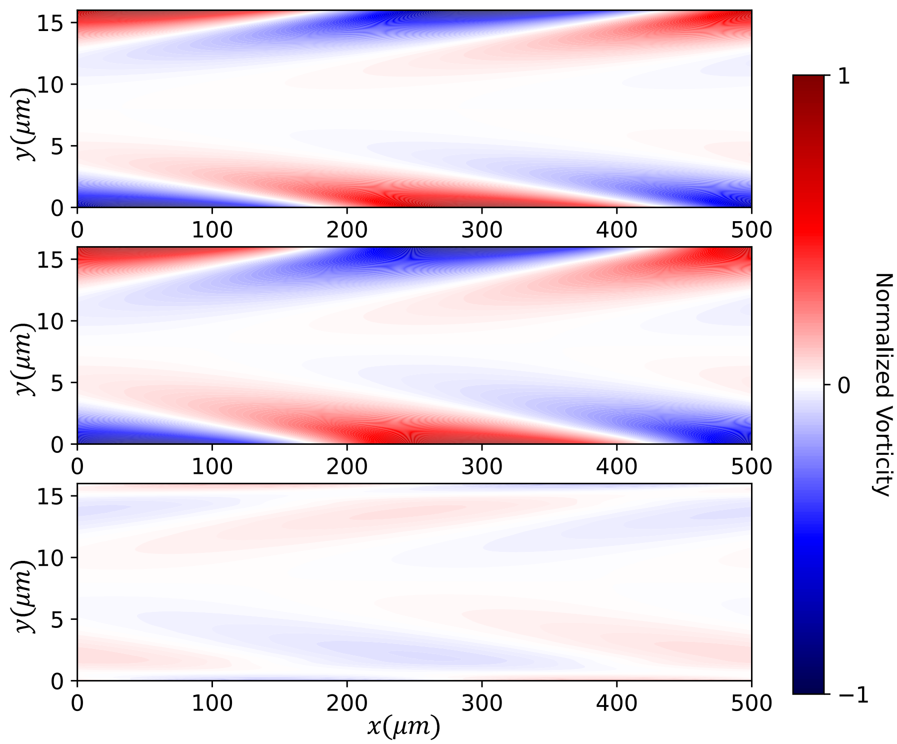


**Figure 5.5:** The following figures illustrate a comparison of vorticity fields obtained from an analytic model (a) and a simulation (b), along with a plot of their difference (c). In each figure, the vorticity is normalized by the absolute maximum vorticity of the model, while maintaining the following parameters: $\lambda = 500$ $\mu$m, $L = 16$ $\mu$m, $\epsilon = 0.0013$, and $c = 60$ m/s

## 5.2 Low Reynolds Number $Re < 1$ Validation of the Experimental Model

Even though my experimental device was not originally designed for applications with low Reynolds numbers ($Re \ll 1$), it is versatile enough to be able to achieve those conditions without major modifications. As part of the study I performed and published in [48], I decided to perform validation of the experiment by comparing experimentally measured values at low Reynolds number with values predicted by the low Reynolds number model from Shapiro analytic model [19].

To ensure a valid validation process, it is crucial for me to reinforce the significance of the mean pressure gradient's impact on peristaltic pumping. I have addressed this topic in detail in section 2.3.3, and to validate my results, I conducted all measurements under zero mean pressure gradient conditions. To clarify, the experimental setup was connected as depicted in figure A.5 in the appendix section, which ensured a zero mean pressure gradient.

Although the derivation of the following equation is presented in various studies from Weinberg [32] and Shapiro [19], but the most detailed description is found in Eckstein's thesis [43].

$$Q_o = \frac{3\epsilon}{2+\epsilon^2} \tag{5.5}$$

Using $Q_o$ I have a single parameter to validate between the analytic model and experimental measurements, similar to the validation approach I presented earlier where I used the root-mean-square velocity. I performed experiments for three Reynolds number values, $Re = 0.05$, 0.10, and 0.20, with varying amplitudes ranging from $\epsilon = 0.35$ to 0.70. The experiment had to be slightly modified using polycarbonate sheet spacers as described in the appendix section A.1. The modification reduces $L$, which increased the capability for $\epsilon$ to be higher, and consequently lowers the Reynolds number of the system as $L$ is proportional to $Re$. Having a higher $\epsilon$ also helps address the issue of background convection, as it increases the magnitude of the velocity of the induced flow.

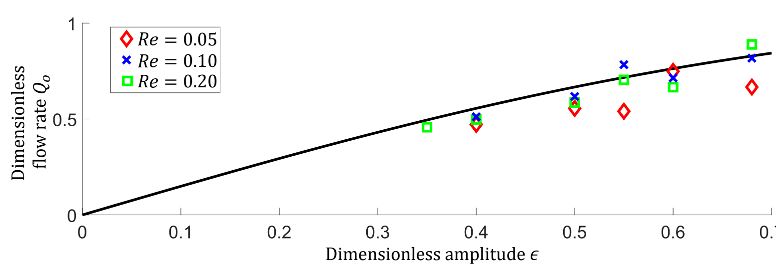


**Figure 5.6:** The flow rate, expressed as a dimensionless quantity using equation 5.5, was measured and found to vary with deformation amplitude in accordance with the analytic estimates provided by [9] (black curve). It is important to note that these results only apply to a recirculating setup, in which the mean pressure rise is zero.

Figure 5.6 shows a comparison between the analytically derived dimensionless flow rate $Q_o$ and experimentally measured values. One can see there is good agreement between theory and experiment. Further validating the capabilities of the experimental device.

## 5.3 Application in Mass Transport and Mixing

To comprehensively validate the models I have presented, it is crucial to conduct a thorough assessment of the Lagrangian transport characteristics of the flow. This is important, as the goal of modeling mixing dynamics in the inner ear is rooted in understanding how concentration is transported in the inner ear. This subsection demonstrates the practical application of the analytic model in the context of the inner ear, which is the motivation behind this study, as well as in the general study of mass transport and mixing in peristaltic flows.

One will see that the analytic model yields no net flow, and my experimental measurements also showed that there is no net flow for the parameter range I studied. This was expected since Shapiro et al's [19] study showed with equation 5.5 that a net flow in peristaltic pumping is proportional to $\epsilon^2$. Given that my focus is on small amplitudes, i.e. $\epsilon \ll 1$, it begs the question of how does this system achieve transport or mixing without a net flow? The answer lies in the Lagrangian dynamics exhibited by peristaltic flows.

First, I have to translate the analytic model's Eulerian results into the Lagrangian perspective. To do this I had a series of approaches. The first approach was to numerically calculate the positions of individual particles in the flow over time. I did this using a forward Euler scheme in time, in a parallelized code in MATLAB. The scheme can be summarized as the following:

$$p_{i+1} = p_i + \Delta t U(p_i)_i, \tag{5.6}$$

where $p_i$ is the position of a particle at time $i$, $\Delta t$ is the time step size, and $U(p_i)_i$ is the velocity at the particle position, at time $i$.

The results of the numerical integration were compelling, I observed that particles in peristaltic have looped paths. However, while performing convergence analysis, I noticed that the calculated paths were extremely sensitive to time step size. By comparing solutions for different time step sizes, I determined that in order to achieve convergence for the solutions I would require time steps to be approximately equal to $16000/f$, where $f$ was in the order of 1 Hz. This meant impractically high computation times (over two days) for simulations longer than a couple of periods. To further complicate the issue, it was evident that particles exhibited some net displacement, however, it was small for each period, demanding that I run simulations for multiple periods to obtain any meaningful results.

The way to address this difficulty with the computational method was to use the generalized Lagrangian mean method from section 2.3.1. Computationally, it means that I only have to run the calculation over one period. Then, the difference between the initial and final position of particles divided by the period of the flow yields the generalized Lagrangian mean field. This obviously reduced the computational burden significantly as I only needed to compute particle paths over one period. Having obtained analytic results, I moved on to the experimental measurements. I used PTV (as discussed in section 4.2) to measure the particle paths of individual microspheres in the apparatus. On the analytic side, I used two approaches. A brute force approach by numerically integrating paths using the velocity field given by the analytic model, and a purely analytic approach by analytically integrating using the generalized Lagrangian mean method described in section 2.3.1.

First I compared the Lagrangian analytic results and experimental measurements by looking at the particle paths themselves. Figure 5.7 shows particle paths from the experimental measurements, analytic results, and numerical results. It was difficult to capture particle paths in high detail in the experiment, however, the results are still compelling. It is clear that the path a particle follows shows close agreement between methods when compared at approximately equivalent locations. Another notable characteristic is that when different waveforms are induced, one can see that the particle path is affected accordingly. This suggested that is possible that different waveforms may have significantly different Lagrangian dynamics.

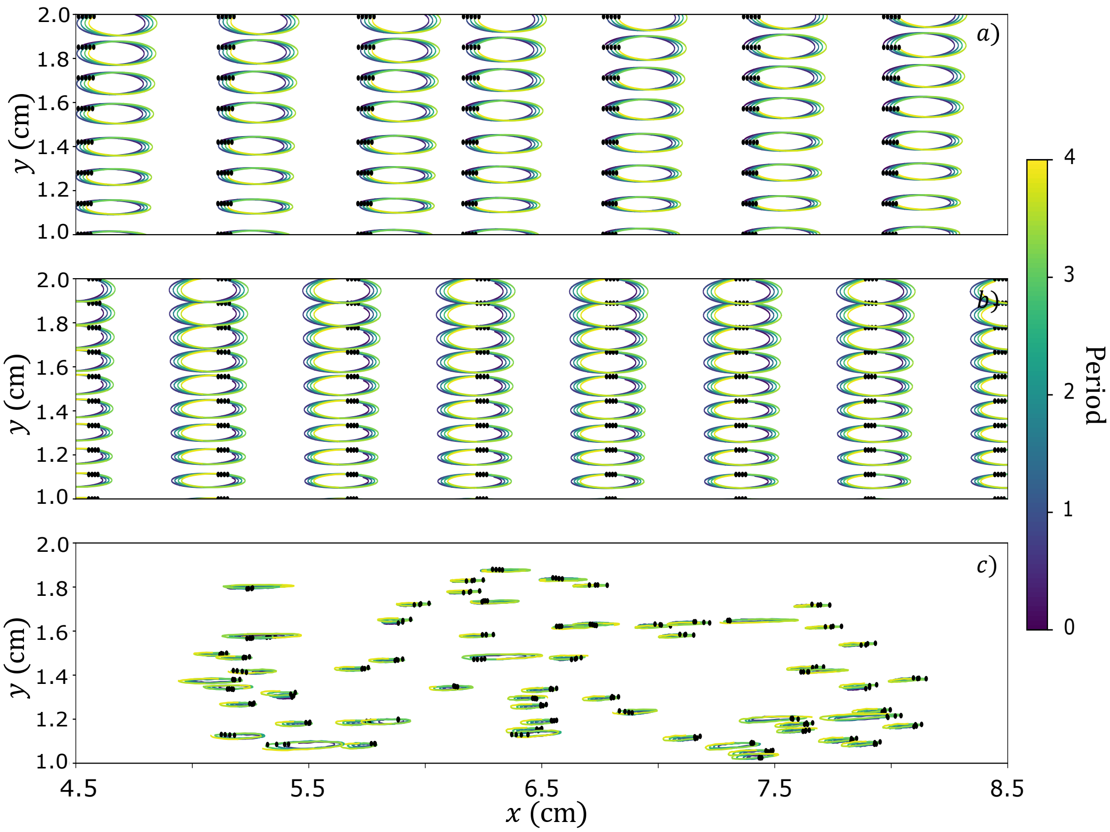


**Figure 5.7:** Examples of a) simulated, b) analytic, and c) experimentally measured particle pathlines, with $c = 1$ m/s, $\lambda = 30$ cm, and $\epsilon = 0.03$. Black points mark particle locations a period apart.

In order to quantitatively validate the models, I decided to compare the models by comparing calculated generalized Lagrangian mean fields. A comparison of average Lagrangian velocities in the bulk region of the flow (from $y = 0.1L$ to $y = 0.9L$) among the experimentally, numerically, and analytically calculated generalized Lagrangian mean is presented in figure 5.10. It is evident from the figure that there is a high level of agreement among the experimentally, numerically, and analytically calculated Lagrangian mean velocities. This result reinforces the accuracy and reliability of the models.

Prior to applying the model to the parameters of the inner ear, it is crucial to thoroughly validate the accuracy of the modeled Lagrangian dynamics. This is due to previous studies suggesting that peristaltic flows exhibit varied transport dynamics depending on the parameters studied. Therefore, it is imperative to analyze the Lagrangian mean velocity profile to gain insight into its characteristics. Specifically, Weinberg et al. [32] saw two effects, trapping, and reflux. For the specific case I am examining, where the peristaltic flow parameters fall within the range specified in table 3.1, Weinberg et al. estimated that I would observe reflux. Reflux generates mass transport that travels in the direction of the wave in sections located away from the moving boundary, while inducing mass transport in the opposite direction near the moving wall. The findings presented in Figure 5.8 illustrate the streamlines and their corresponding velocities in the $x$ direction of the Lagrangian mean field for various parameters. The Lagrangian mean field was calculated by applying the GLM method, as detailed in Chapter 4, which involves numerical integration of the Eularian velocity field. The plot indicates the presence of reflux, as evidenced by the negative Lagrangian velocity near the moving wall and positive velocity away from it. The Lagrangian velocities have the highest speed near the moving boundary, while the rest of the channel experiences a slower speed with a transition point of zero speed. Additionally, in figure 5.9 I plot the Lagrangian mean velocity profile, where one can clearly see the effect of reflux. The Lagrangian velocity is positive away from the wall and reverses the direction near it. The point that dictates where the Lagrangian velocity will reverse is driven by the Reynolds number. I quantify that point by locating the edge of the reflux region, which occurs at $y = y_{\text{edge}}$, with $u_{\text{d}}(y_{\text{edge}}) = 0$.

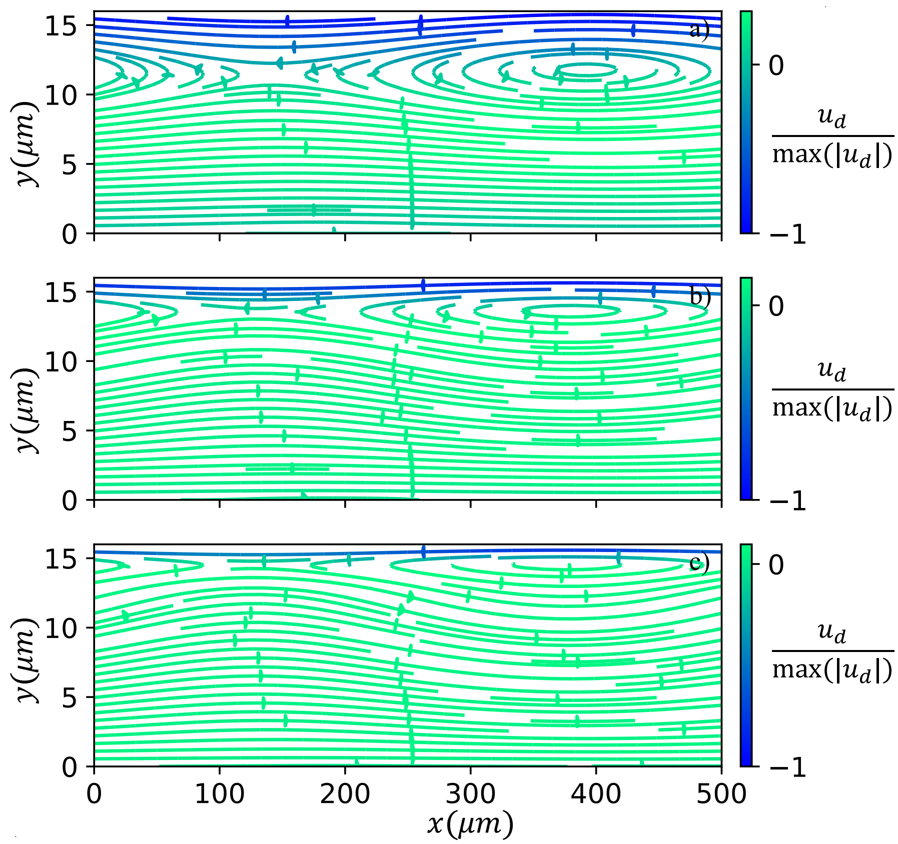


**Figure 5.8:** Comparison of Lagrangian mean fields with wave speed $c = 1$ m/s (a), $c = 10$ m/s (b), and $c = 100$ m/s (c). In all cases, $\lambda = 500$ $\mu m$, $L = 16$ $\mu m$, and $\epsilon = 0.0013$. The color bar is a ratio of the Lagrangian velocity $u_d$ over the absolute maximum Lagrangian velocity over the entire field $|\text{u}_\text{d}|$.

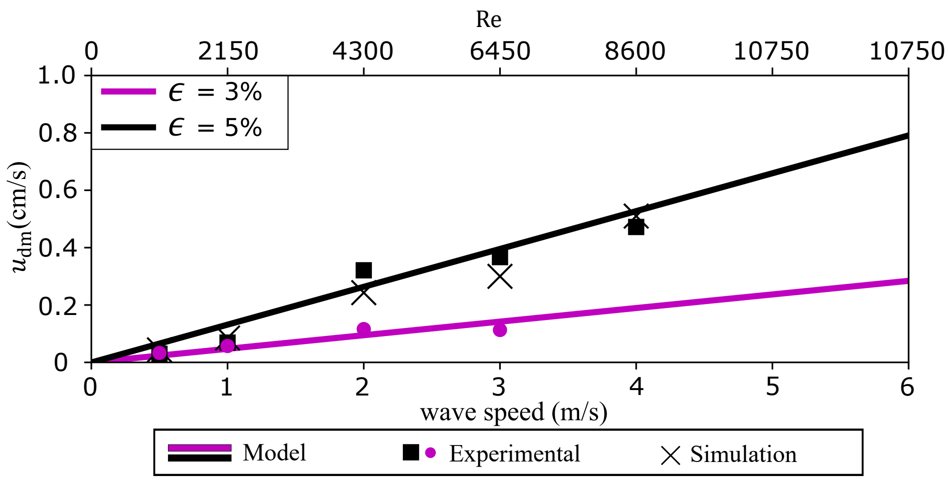


**Figure 5.9:** Variation of the mean drift velocity $u_{\mathrm{dm}}$ with wave speed $c$ and nondimensional deformation amplitude $\epsilon$, and the calculated Reynolds number. The wavelength was held constant at $\lambda = 30$ cm.

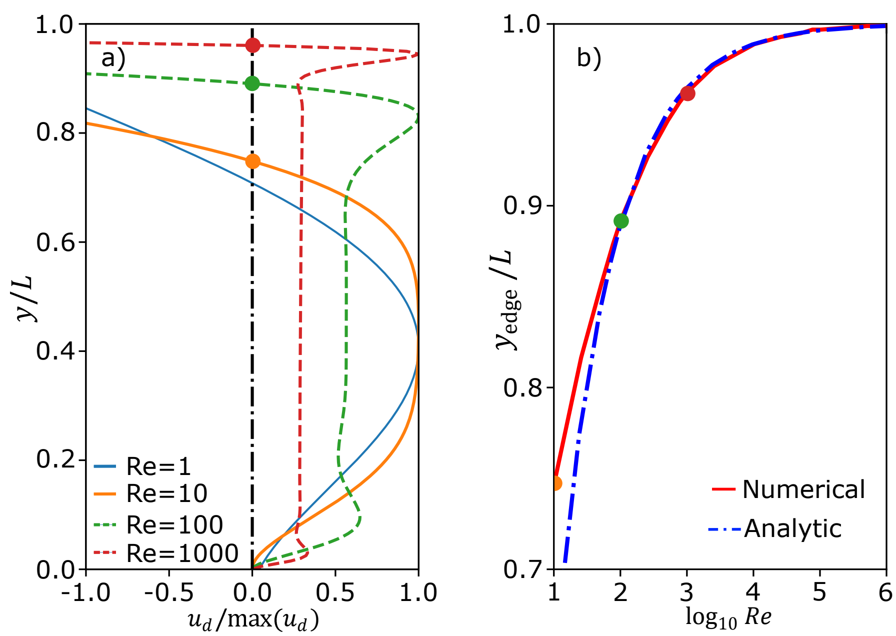


**Figure 5.10:** a) Comparison of the normalized drift velocity profile $u_{\mathrm{d}}/\max(u_{\mathrm{d}})$, at different Reynolds numbers $Re$. The black line marks the zero velocity point. b) Location of the edge of the reflux region, as predicted by the analytic model. The red line was obtained through numerical integration of the Eulerian velocity field. The blue line was obtained with the analytic model. The dots are the edge location for the curves in figure a), and the color matches the relevant Reynolds number. As the Reynolds number increases, the reflux region shrinks.

Now that the accuracy of the Lagrangian dynamics in the analytic model has been validated, I can confidently apply the model and expect accurate results. It is reasonable to anticipate that the model will produce precise outcomes when simulating flows in the inner ear. Moving forward, recall that the relevant parameters for peristaltic flow in the inner ear were obtained from in-vivo studies such as Karavitaki and Mountain [20]. The parameter values were presented earlier in table 3.1. I will now use these parameters to determine whether they can achieve the goal of mixing in the inner ear.

To fully determine the effects of peristaltic pumping on mixing. I used an advection-diffusion numerical simulation developed by fellow researchers at the University of Rochester. Details on the simulation code can be found in Troyetsky et al. [49]. Using this simulation model, I was able to determine how a channel with a peristaltic flow and one without any flow will transport some arbitrary concentration over time.

In figure 5.11 I show a comparison of advection-diffusion simulations of two channels with a concentration in a channel evolving over time. In one case, no flow is present, and diffusion alone is responsible for the concentration's spread. The other case features peristaltic flow which was calculated using the analytic model, where the parameters match the inner ear's estimates that I previously presented in table 3.1. One can see that the channel that has a peristaltic flow present, mixes the concentration significantly faster than the channel that relies on diffusion alone.

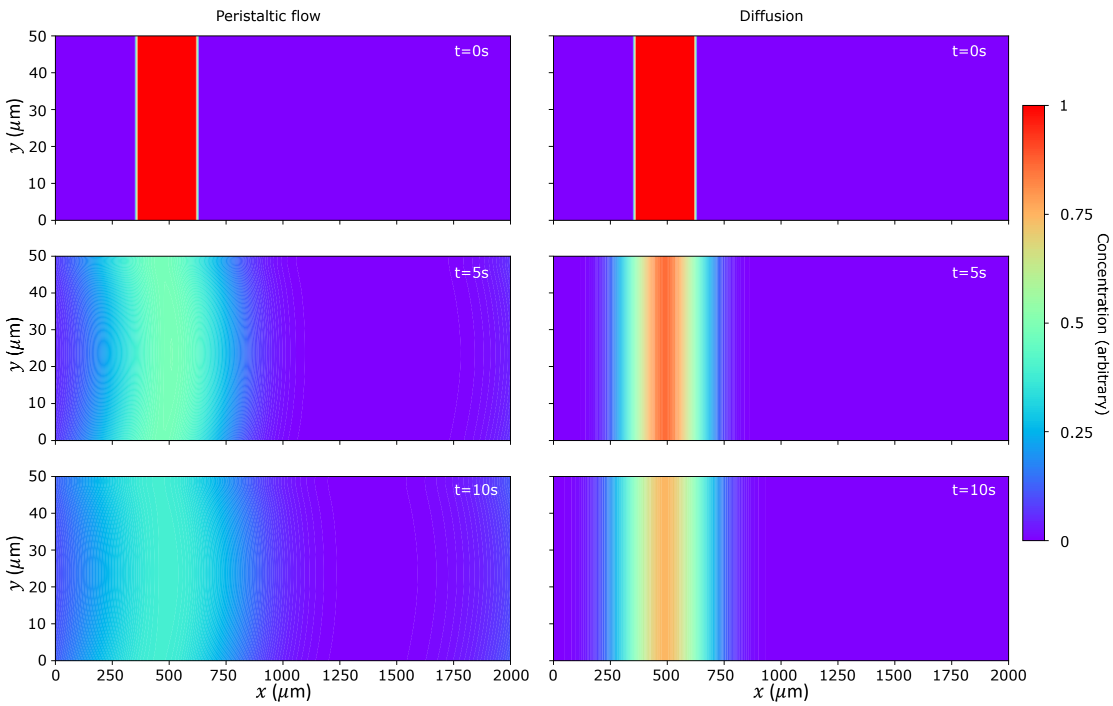


**Figure 5.11:** The figure illustrates the variation in the concentration of a passive scalar, influenced by both diffusion and the modeled Lagrangian mean flow, as well as by diffusion alone. When subjected to flow, the values of the parameters $\lambda = 200\ \mu$m, $L = 50\ \mu$m, $\epsilon = 0.002$, and $c = 50$ m/s are utilized, while the diffusion coefficient $\Xi$ remains constant at $7 \times 10^{-10}$ m$^2$/s in both cases. It can be observed that the peristaltic flow leads to greater mixing compared to the case with diffusion alone.

The reason why it makes sense that peristaltic flows enhance mixing in the inner ear is due to the presence of reflux. As discussed in section 2.1, the Tunnel of Corti is a long and slender channel, which means diffusion time scales along the $y$ axis (if one thinks of it three-dimensionally along in the direction of the diameter) is significantly faster (10 mm/50$\mu$ m$\approx$ 200 times faster). Reflux has the effect, as shown in figure 5.11 and figure 5.10, of spreading a layer of material along $x$ at speeds of the order of $A\omega$, and then diffusion takes the role of spreading the displaced concentration in $y$. This is likely an effect named Taylor dispersion and studied originally in [50, 51]. Taylor dispersion works in similar conditions where specific advective transport produces enhanced mixing of a fluid.

# 6 Oscillatory Flow in Junctions

This and the following chapters focus on how I studied the effect of channel geometries on oscillatory flows. The motivation for this study originated from an interest in developing a better understanding of how fluid flow occurs in the glymphatic system. The glymphatic system consists of a network of fluid channels in the brain where a form of oscillatory flow has been measured [10]. The underlying mechanism that drives this flow is unknown at this time, however by building a simple toy model which captures some of the features found in the real system, I hope to find useful data that can help develop a full theory of how the glymphatic system works. To better understand the importance of the glymphatic system, I will now provide an overview of how it is built and works.

The glymphatic system is a recently discovered system of the central nervous system that plays a key role in the clearance of waste products from the brain. It was discovered by Iliff et al. [52] in 2012. It is a specialized version of the lymphatic system and is composed of glial cells, small channels, and perivascular spaces that provide a pathway for cerebrospinal fluid (CSF) to flow through the brain. This system is essential for the maintenance of brain health and for the prevention of a range of neurological diseases. The glymphatic system works by allowing CSF to flow through the brain, picking up waste products such as amyloid beta proteins, which are associated with Alzheimer's disease.

The glymphatic system is composed of a series of perivascular channels and astrocytic processes. These channels are lined with glial cells, which act as support structures for the pathways and help to facilitate the flow of interstitial fluid (ISF) and waste. The paths of these channels are arranged in an interconnected web-like structure, with each pathway leading from one region of the brain or spinal cord to another. This allows for the efficient and rapid transport of waste and ISF throughout the brain and spinal cord.

The glymphatic system fluid network consists of vessels and channels that surround the blood vessels of the body, which in turn bifurcate and distribute to many sections of the brain. Figure 6.1 shows an image of how the glymphatic channels are structured around arteries. Figure 6.2 shows a model from [11] where the glymphatic system is shown to be a complex network of fluid channels.

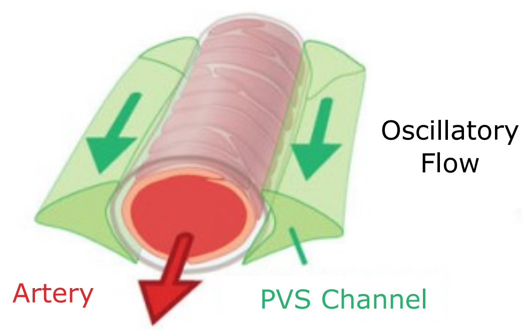


**Figure 6.1:** Sketch from [10] shows the structure of a glymphatic channel. The channel surrounds the artery and exhibits an oscillatory flow.

In 2018, a study by Mestre et al. [10] reported evidence of oscillatory flow in the glymphatic system. The study used two-photon microscopy and fluorescent tracers to visualize the movement of interstitial fluid in the mouse brain. It found that the pulsatile flow of glymphatic fluid was driven by the oscillatory contractions, which created a wavelike flow of CSF fluid within the glymphatic system. The authors concluded that this flow, which exhibits oscillatory characteristics, might be a mechanism for efficient and rapid clearance of metabolic waste from the central nervous system. Figure 6.3 shows flow measurements presented in [10] in the glymphatic system.

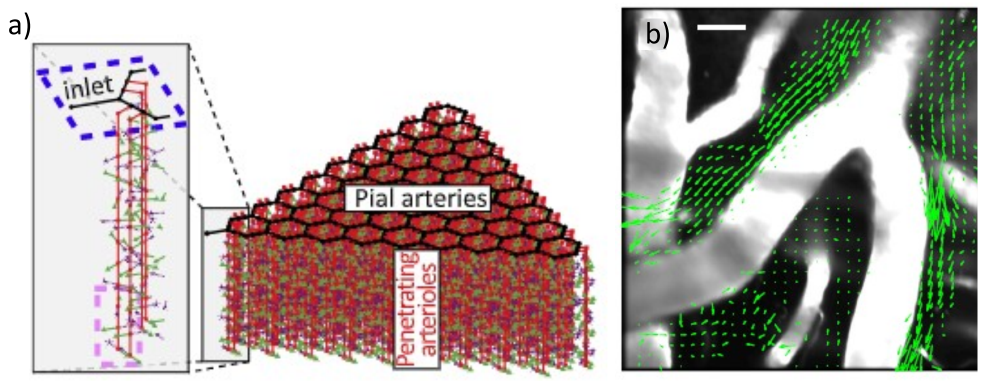


**Figure 6.2:** The diagram depicted in figure a) illustrates that due to the glymphatic system's composition of numerous branching channels, it is feasible to represent the system as an abstract fluid network model, as noted by Tithof and colleagues in their recent publication [11]. figure b) shows an image of a channel bifurcation where measurements were performed [10].

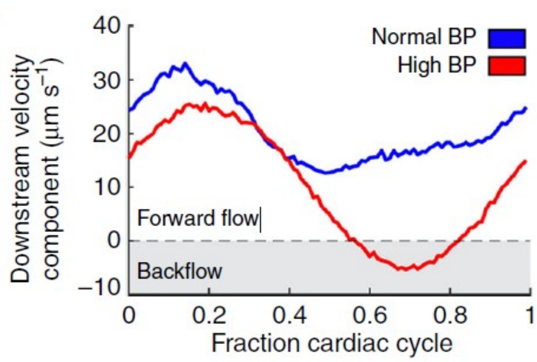


**Figure 6.3:** Flow measurements found in the glymphatic system from [10]. The figure shows how the flow-tracking particles move directionally in the channels with an oscillatory component.

At present, the mechanisms behind flow in the glymphatic system remain unclear. A review of the current hypotheses was put forth by [53]. As the implications of understanding glymphatic flows are significant, and oscillatory flow has been observed in the glymphatic system, I constructed a simple experimental device that can simulate flows with some of the same characteristics as the glymphatic system. My aim was not to recreate the exact environment of the glymphatic system, as this would be a challenging endeavor given the present unknowns. Rather, I sought to investigate whether certain characteristics of the system may have an effect on flow. I sought to isolate the fluid flow characteristics of an oscillatory flow, likely caused by the deformations of the arterial walls, and of bifurcating channels, which downstream split into multiple channels.

To guide my study, I conducted a review of various studies that investigated mechanisms involving an oscillatory flow in a channel system with some type of junction. The studies I focused on examined flow mechanisms where an oscillatory flow can result in a directional net flow due to a temporally asymmetric flow resistance at a T-junction. This effect can be described as rectification of the oscillatory flow, although the oscillatory component is not eliminated, unlike in the context of electronics. This means that when fluid is pushed in one direction through a junction, it will not exhibit the same flow resistance when flowing in the opposite direction. These are expected characteristics of a network-like fluid channel system such as the glymphatic system. To simplify the complex network of flows and observed oscillating flow in the glymphatic system, I reduced the system to a local junction for study. This approach has been used in other biological systems with complex networks and flows, such as studies of flow inside the lungs and arteries [12, 54, 55].

Some examples of studies that considered a simple system, where a junction and an oscillatory flow produce some net flow, i.e. have some form of rectification. Takagi et al. [56, 57] performed studies that focused on the nature of oscillatory flows interacting with a T-junction. Their system consisted of two reservoirs connected by a tube. The tube had a T-junction that connected to a piston. They observed that a pressure gradient between reservoirs can be produced if the length of the two pipes was not equal. Propst [58] performed an analytic analysis to further evaluate the nature of such a pumping mechanism. He created analytic models that captured the dynamics of the piston and junction system and ultimately determined that some form of nonlinear resistance at the T-junction is necessary in order to create a pressure gradient across the system. The results were further validated later by Cid et al. [59]. Lastly, a study by Nguyen et al. [12] showed a very similar system. In the study, they showed a looped channel where they were able to produce a flow by inducing an oscillatory flow with a magnetic piston within a channel. They hypothesized that this type of channel geometry has similar physical characteristics to that of lungs in birds, and can explain how flow occurs in looped sections of bird lungs. Critically, they theorized that the driving mechanism for this effect was the flow separation caused at the T-junction (figure 6.4).

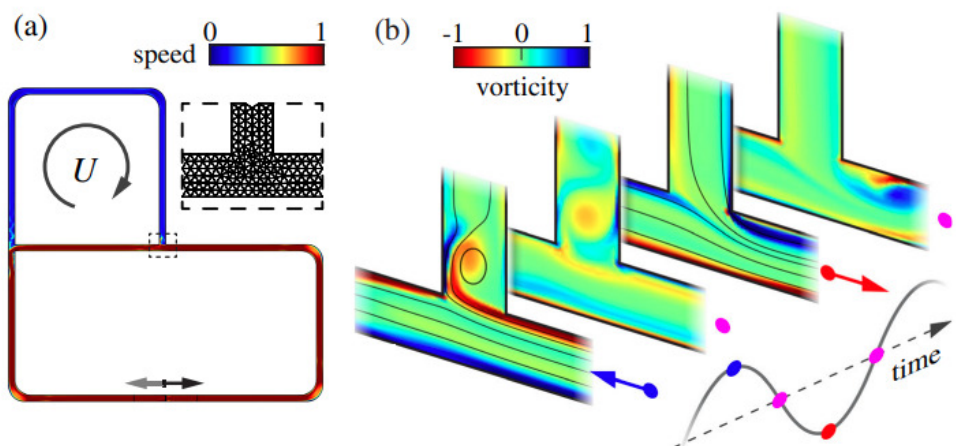


**Figure 6.4:** Figure from Nguyen et al. [12]. (a) Shows the simulated looped channel, the color is the speed of the flow along the channel at a selected point in time. Speed is normalized by the maximum value. At the bottom section, there is a piston driving the fluid. (b) The figure shows computational results at the T-junction of a looped channel in simulations. Four points of the cycle are plotted with the respective vorticity. The plot shows that over the cycle, there is some form of asymmetric flow structure in the cycle. This is what the authors pointed out to be flow separation that results in a valving effect, which ultimately produced a directional flow in the looped section of the system.

The studies revealed the possibility of generating net directional fluid transport in a system by solely utilizing an oscillating flow and a geometric feature in the form of junctions. In relation to the glymphatic system, periodic deformation of the walls of the perivascular space (PVS) was observed, which would likely displace fluid in an oscillating manner [53]. The PVS channels are structured as a network with many junctions. However, a main limitation in the comparison between the literature presented and the glymphatic system was the difference in parameters. The analysis from Mestre et al. [10] indicated that the flow in the glymphatic system was predominantly dominated by viscous forces, which were incompatible with the previous literature. Nonetheless, Nguyen et al. [60] found that for certain geometric conditions, it was still possible to observe a directional flow induced by advective forces, even when dimensionless analysis suggested that viscous forces were dominant. Therefore, the direct applicability of my findings to modeling flows in the glymphatic system remains open.

# 7 Oscillatory Flow in Junctions: Preliminary Study

This chapter focuses on describing the preliminary experiment design and findings employed to model two key components of the glymphatic system. The fluid system consisted of an oscillatory flow in a closed-channel fluid network. The preliminary design can be thought of as initial testing to determine if there were any interesting results. I then used the findings from this chapter to refine the experiment design and develop a better understanding of the system's dynamics which are explored in chapter 8.

## 7.1 Experiment Device

The initial experiment consisted of two channels, with a section of the two divided by a flexible membrane (shown in figure 7.1). Previous research on the glymphatic system hypothesized that pressure in adjacent blood vessels could cause deformations in the channels and, in turn, drive the flow. The membrane section was designed to simulate such deformations and investigate whether they serve as a driver of the flow.

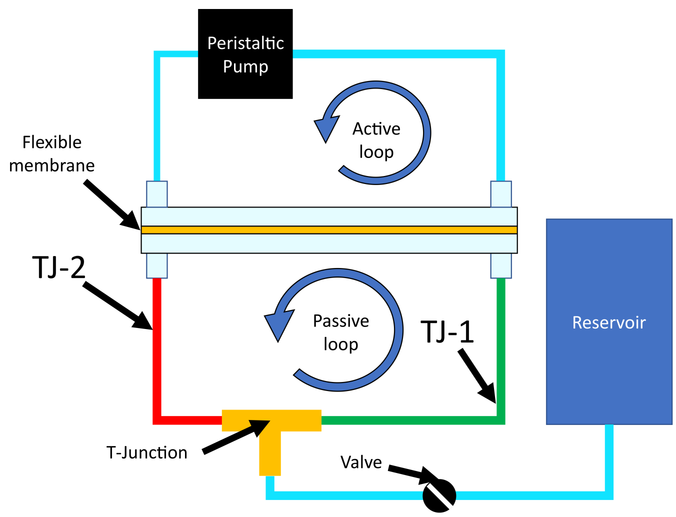


**Figure 7.1:** Sketch of the preliminary experimental design. Shown are the channel configurations of the experiment. The system has two fluid channel loops separated by a flexible membrane at one section. The two tubes are TJ-1 with a length of $L_1$ and TJ-2 with a length of $L_2$. A valve was in the system to help me fill the experiment with water. During experiments, the valve was always open, when closed no fluid was observed to be displaced in the passive loop. The top blue arrows indicate the positive direction of the flow, for this experiment.

The key parameters to consider in the experiment were the frequency $f$ of the flow, the length $L_1$ of the tubing TJ-1, the length $L_2$ of the tubing TJ-2 where $L_1 \geq L_2$, the total loop length $L_{tot} = L_1 + L_2$, and $\gamma = L_1/L_2$. Note that the frequency of the flow in the passive was always equal to the frequency of the peristaltic pump, and no lag in response was ever found. In other words, the phase of the active and passive channels was always equal. I constructed the dual channel component using four transparent acrylic sheets of 1/8 inch (3.2 mm) thickness, which I cut to specification using a BOSS CO2 laser. In between the layers of acrylic sheets, I placed thin rubber sheets (McMaster-Carr part no. 85995K12) with a thickness of 0.006 inches (0.15mm). These rubber layers were cut to match the size and through-hole features of the acrylic sheets, and so that when compressed the acrylic layers would seal. The rubber layer's role is mainly to provide a seal, but the middle one plays an additional role of being a shared wall between the two channels. Figure 7.2 shows a drawing of the layers with detailed dimensional specifications and has labels on the significance of the features. The laser cutter produced the through holes where I used 1/4-20 screws and nuts to tighten the layers together. The inlet features were cut to size to allow for 1/8 NPT threads. I then attached (McMaster-Carr part no. 5153K36) to the 1/8 NPT threads wrapping the threads with a small amount of Teflon tape to ensure a proper seal.

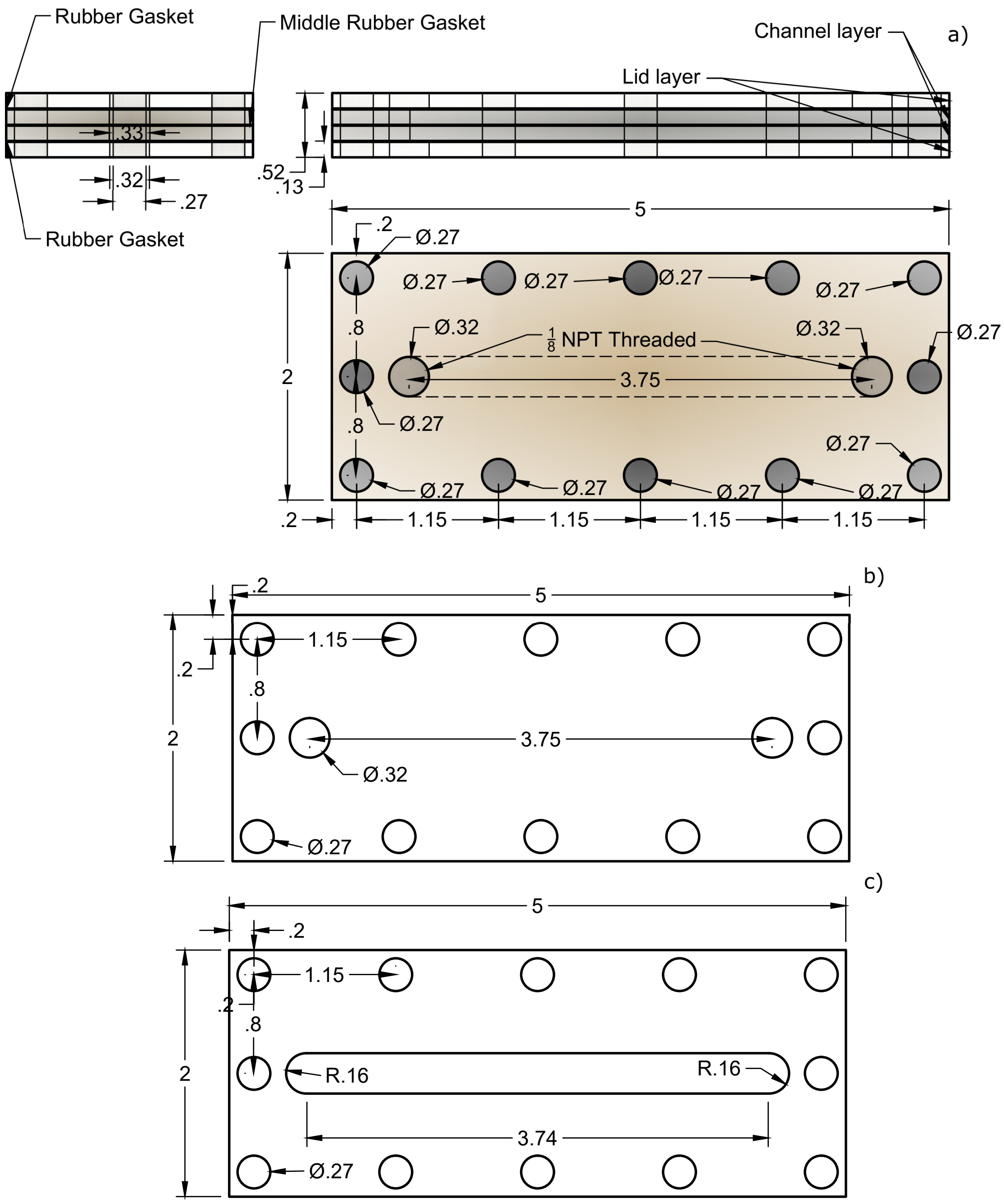


**Figure 7.2:** Detailed drawings of the experiment split channel. All dimensions shown are in inches. a) Drawing of the entire assembly. b) Drawing of the 'lid' layers. c) Drawing of the 'channel' layers.

I filled both channels with water and created two looped channels as illustrated in figure 7.1. The active channel was driven by a Kamoer KPHM400 24V stepper motor peristaltic pump. While the passive channel was connected to a t-connector (McMaster-Carr part no. 5117K13) and a fluid reservoir which I created using plastic soup containers.

The peristaltic pump was controlled using an Arduino MEGA 2560 board and a Pololu AMIS-30543 stepper motor controller. I could specify a rotation speed for the stepper motor that moved the peristaltic pump and it would produce a flow in the driven channel. The peristaltic pump consisted of three roller components that compressed a flexible tube as it rotated. Due to the pump having three rollers, the driven channel would experience a periodic flow with a frequency three times the stepper motor rotation rate. As fluid is pumped in the driven channel, a net pressure is generated, which forces the membrane in the passive channel to be displaced, which in turn displaces fluid in the passive channel.

The T-junction was acquired from McMaster-Carr part no. 5117K13 and is shown in detail in figure 7.3. This is an important detail of the design, as it will be demonstrated in the results that knowing the specific geometric characteristics of the T-junction is critical to the system.

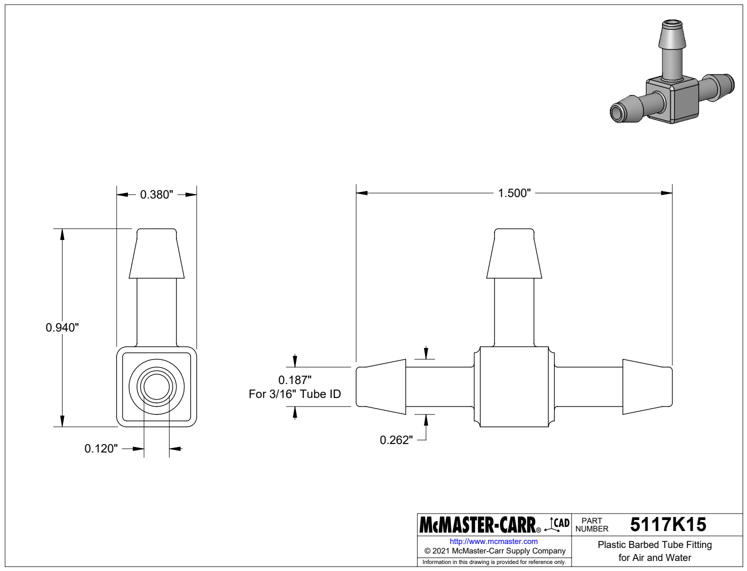


**Figure 7.3:** McMaster-Carr part no. 5117K13 schematic of the T-junction used for experimental measurements. This junction was used for the preliminary experiment, as well as testing the final experiment.

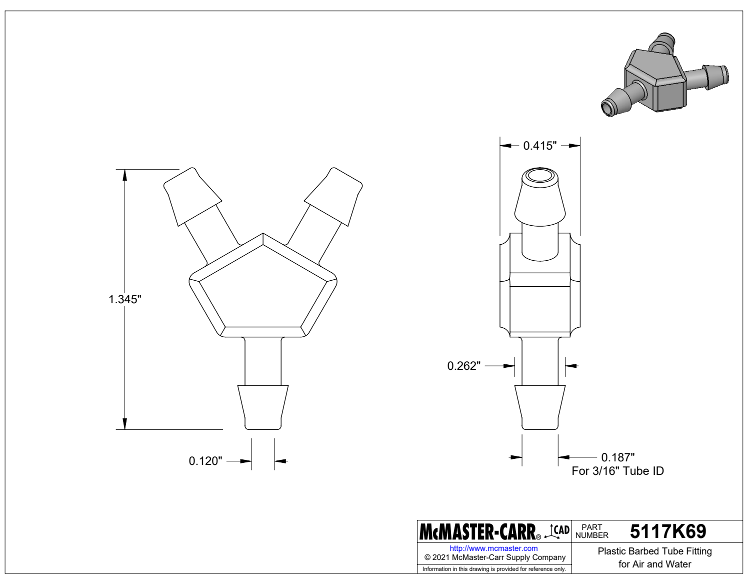


**Figure 7.4:** McMaster-Carr part no. 5117K69 schematic of the Y-junction used for preliminary experimental measurements.

## 7.2 Data Acquisition Techniques

I utilized Emergent M3000 cameras to capture videos of the flow in the system for this experiment. I measured the flow from the videos by utilizing microspheres from Cospheric with dimensions 90-106 $\mu$m and a density of 0.98 g/cc (part number REDPMS-0.98).

I attempted to perform some particle tracking velocimetry (PIV) measurements using PIVLab but found it difficult to produce acceptable data. Details on PIVLab were available on [46] and were also discussed in more extensive detail in chapter 2. The main issue was that my experiment design had no measures to allow for illuminating particles in a plane, due to this all the particles captured by the camera were moving three-dimensionally, which could not be compensated for by the software properly.

I used PredictiveTracker to obtain data, which allowed me to perform Particle Tracking Velocimetry (PTV) as discussed in Chapter 2. The PredictiveTracker produced particle paths for individual particles.

## 7.3 Preliminary Experiment Results

Once the system was set up as described in section 7.1, I selected a set of parameters to test, which meant I selected the tube lengths for TJ-1 and TJ-2 and specified a frequency $f$. I recorded videos of segments of tubing at TJ-1 and TJ-2, as shown in figure 7.1. Using PredictiveTracker, I obtained the paths of the moving particles in the videos. The measured paths provided me with quantitative data, which indicated that particles showed some form of net displacement in the loop section of the device. The particles moved back and forth but seemed to not fully return to the original position, always drifting slightly in one direction.

To obtain a definitive measurement of the net motion of the particles, I took the position of particles in the downstream velocity at two points in time. The two points in time are a multiple of some integer $\mathbf{n}$ times the period of the driven flow $T_{driven}$ apart. Then I can obtain an estimated average net velocity as

$$u_{net} = \frac{p_F - p_I}{\mathbf{n}T_{driven}} \tag{7.1}$$

where $p_F$ is the position of the particle in the flow direction at the end of $\mathbf{n}$ cycles and $p_I$ is the initial position in the flow direction. To ensure that this measurement was as accurate as possible, I would also have to add another condition, where the initial particle position $p_I$ would have to be equal or as close as possible to the point in time where the particle velocity is zero. Figure 7.5 shows particle paths measured at TJ-1, where the downstream position is plotted vs time. The downstream velocity was defined to be positive in the direction from TJ-2 to TJ-1. One can see the oscillatory component of the flow is present, but also that the periodic lines appear to have a linear slope to them, indicating that the particles drift over time.

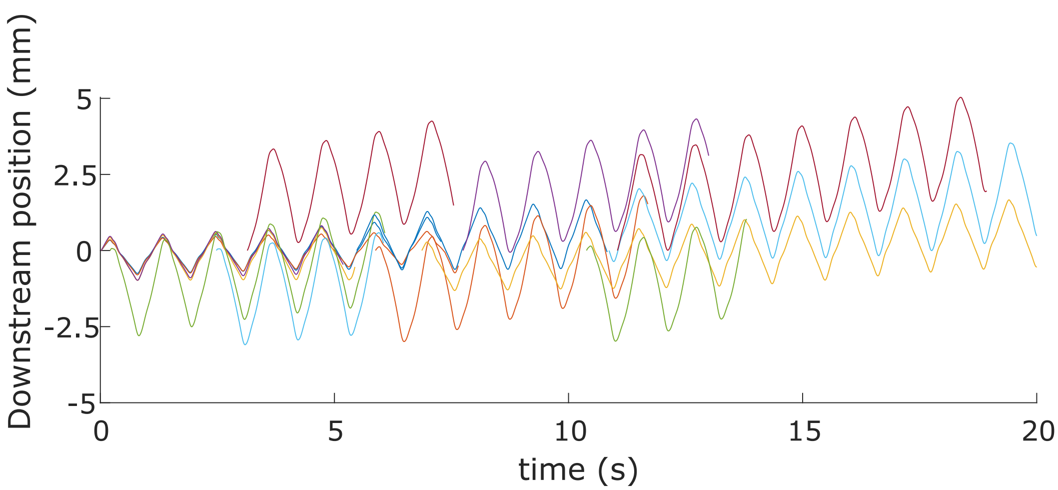


**Figure 7.5:** Shown is a measurement of particle positions at TJ-1 over time. Each line represents a singular tracked particle. The positive direction of position is associated with the position from TJ-1 towards TJ-2. Parameters for this plot were $f = 2.25$ Hz, $\gamma = 4$, $L_{tot} = 40$ cm. The scale was 125 pixels per mm. The lines show the oscillatory nature of the motion, with an added nonperiodic drift. Understanding the source of the nonperiodic drift is the focus of this study.

In all experimental conditions, the net flow appeared to be unidirectional. To investigate this further, I conducted a test to determine whether reversing the peristaltic pump direction in the active channel would result in a reversal of the flow in the passive channel. Despite the reversal of the pump, no change in the direction of the flow was observed, indicating that the mechanism did not depend on the peristaltic pump, but rather on periodic deformations caused by the rubber membrane that induced flow in the passive channel.

To further confirm the presence of net flow, I measured the flow at two different locations, namely TJ-1 and TJ-2. The results of these measurements consistently showed that the particles drifted in the same direction, from TJ-2 to TJ-1.

I observed that the instantaneous speed of the flows at TJ-1 and TJ-2 was significantly different, this is shown in figure 7.6. From this, I hypothesized this was due to the different flow resistances between TJ-1 and TJ-2 due to their length and the oscillatory flow in the system. Notably, the ratio of maximum measured speeds was approximately equivalent to $\gamma$, where the maximum speed at TJ-1 was approximately four times lower than at TJ-2.

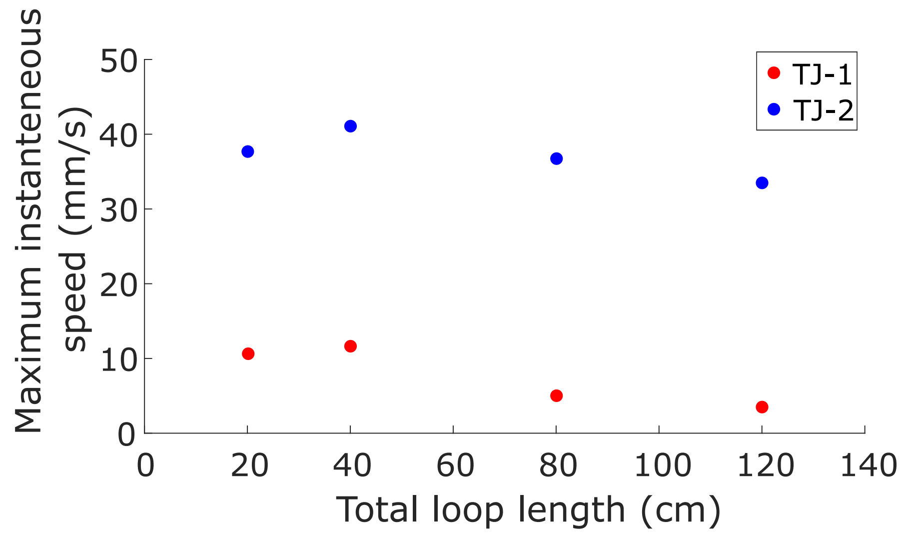


**Figure 7.6:** Shown is the maximum instantaneous speed as a function of the total loop length $L_{tot}$. The loop ratio was held constant $\gamma = 4$ and $f = 2.5$ Hz. Measurements in blue were performed at a section of TJ-2. Measurements in red were performed at a section of TJ-1. The maximum instantaneous speed decreases with increasing total loop length $L_{tot}$. The data suggest that this decrease is likely due to an increase in resistance from viscosity in the loop. This is in agreement with the expectation that resistance to flow in a pipe increases linearly with $L_{tot}$. The plot shows each tube of the loop has different speeds related to the difference between $L_1$ and $L_2$, likely due to viscous resistance to the flow. Note that speed has no direction, and if the direction were to be applied, the measurements for TJ-2 would be negative.

Having established some basic observations of the system, and a number to quantify the flow, I moved on to running experiments in an attempt to determine which parameters drive the flow. I decided that the parameters to test would be the frequency of the flow $f$, and the length of the tubes $L_1$ and $L_2$. This was to test the hypothesis that a difference between $L_1$ and $L_2$, combined with an oscillatory flow was enough to generate a flow. Perhaps if the flow is driven by the difference between $L_1$ and $L_2$, a larger mismatch would lead to a faster flow. Testing the frequency is a simple way to test if there is a link to the oscillatory component of the flow.

First, fixing the length of the tubes to $L_{tot} = 40$ cm and varying the frequency of the pump, I found that as I increased the frequency, there was a tendency for the net velocity of particles to increase. In figure 7.7 one can see that as the frequency of the pump increased, the measured net velocity also increased. However, after reaching a frequency of 2.5 Hz, the net displacement per cycle decreased.

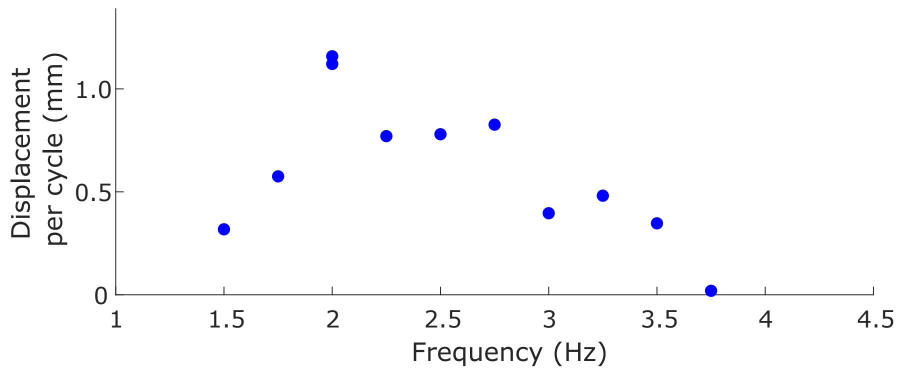


**Figure 7.7:** Measurements of the net velocity of particles at TJ-1 when the frequency of the peristaltic pump is varied. The plot shows an upward trend in net velocity where it peaks somewhere between 2 Hz to 2.75 Hz. The loop ratio was $\gamma = 4$ and loop length $L_{tot} = 40$ cm.

This observation was critical in determining the next step of the study. I had two possible explanations for what was causing this behavior. One possibility was that a frequency of 2.5 Hz was creating optimal conditions in how the flow behaved at the T-junction, and thus the maximum displacement of the system would be dictated by the connections and channel geometries. The alternative was that the fluid was being pushed by a rubber membrane which experienced periodic pressure increases due to the peristaltic pump pushing fluid. The rubber membrane must have some natural frequency at which the amount it was displaced would be maximized. This would mean that near that natural frequency of the membrane was creating larger displacements of fluid than at other frequencies. If that were the case, I could not conclude that there was an optimal frequency for a generalized system, as all the frequency dependence would be linked to the material properties of the flexible wall.

I measured the maximum instantaneous speeds as a function of frequency as shown in figure 7.8. I found the same trend as for the results in figure 7.7. This further validated my suspicions that the experiment design's link to the mechanical properties of the flexible membrane posed a significant limitation, as it was not possible to isolate the effects of the amplitude of the membrane's deformation and the frequency on the induced flow of the passive channel. This led me to redesign my experiment for final measurements presented in chapter 8.

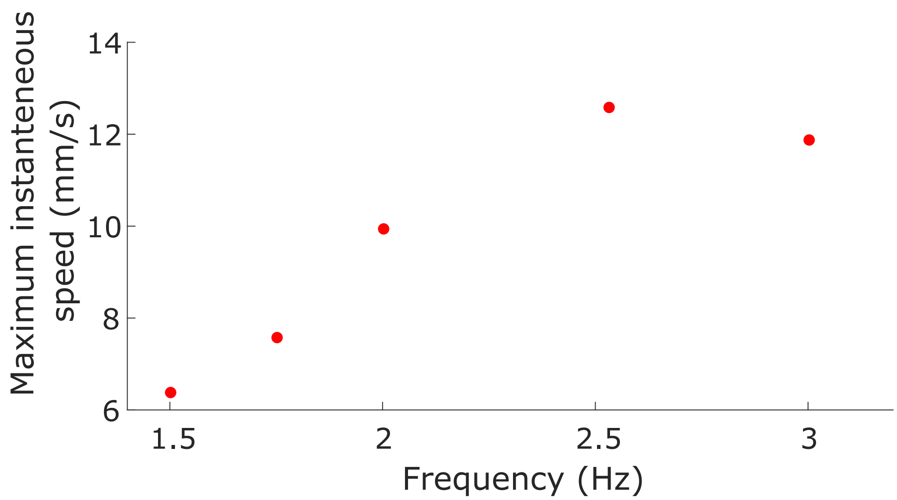


**Figure 7.8:** Measured maximum instantaneous speed of particles at TJ-1 as the frequency is varied. Other parameters were held constant at $L_{tot}$ = 80 cm, $\gamma$ = 4. Similar to figure 7.7, the particles' maximum instantaneous speed appears to peak around the same frequency range. One potential explanation for the speed peaking around a specific frequency is that the rubber membrane is excited at that frequency, and as such the maximum amount of deformation to displace fluid in the active channel occurs at around 2.5 Hz.

Before diving into the redesigned experiment, I continued making preliminary observations to determine what other factors play a role in inducing a net flow. I tested whether unequal lengths between tubes TJ-1 and TJ-2 were a necessary condition to induce a net flow. It was easy to comprehend why having equal length tubing would not result in a net flow. If both tubes were of equal length and the membrane was shifted uniformly in relation to the channel, it was reasonable to assume that the fluid would be displaced symmetrically into and out of the reservoir, thereby leading to no net flow across the loop. However, if a net flow was produced with equal length tubes, then it seemed probable that the driver was the flexible membrane deformation. It was possible that the peristaltic pump had caused the wall to be moved in an asymmetric manner, which resulted in a net flow across the loop.

I tested this hypothesis with equal length tubing, leading to noisy results, which are shown in figure 7.9. It was clear that there was no consistent pattern. I hypothesized two possible reasons for this: first, I had not taken enough time to refine my analysis methodology, which could have caused errors in the results. Second, I had cut the tubing by hand, measuring the lengths $L_1$ and $L_2$ with a ruler; thus, it is likely that the small differences between tubing lengths resulted in net flows. This hypothesis is analogous to that of an unstable point, such as a ball at the top of a hill, where it is impossible to place the ball in the exact middle.

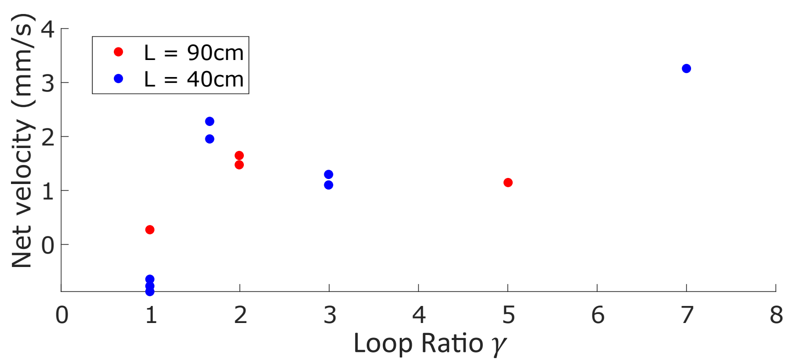


**Figure 7.9:** A series of measurements of net flow for different values of the loop ratio $\gamma$ and two different total lengths $L_{tot}$ were plotted at a fixed frequency of $f = 2$ Hz. The results indicate that no consistent pattern emerges regarding how $\gamma$ affects the flow. However, noteworthy variations are evident near $\gamma = 1$, which can be explained by the expectation of no net flow at this point, and the consequent potential for drastic changes as we move away from it.

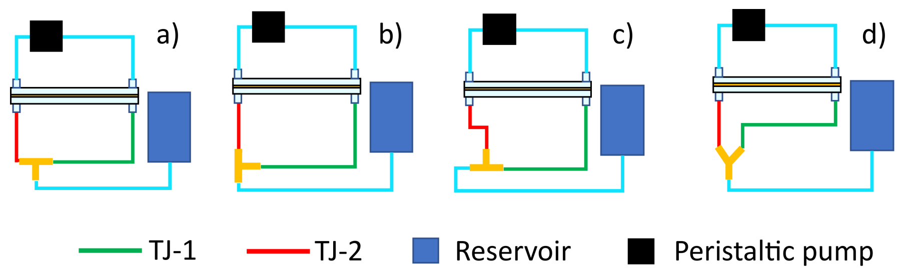


**Figure 7.10:** Shown are the tested configurations for different geometrical configurations that I tested. The resulting measured net velocities are shown in table 7.1.

| Configuration | Net Velocity (mm/s) at TJ-1 | Net Velocity (mm/s) at TJ-2 |
|---|---|---|
| a) | -0.06 | 0.20 |
| b) | -0.12 | 0.49 |
| c) | 0.14 | -0.33 |
| d) | 0.03 | -0.04 |

**Table 7.1:** Table showing measured net velocities for different T-junction configurations. The configurations' details are shown in figure 7.10.

So far, I had not yet changed the T-junction of the looped channel. I hypothesized that altering the geometry of the junction, from a T-junction to a Y-junction, might lead to different flow characteristics. This could be due to the fact that the geometry can impose different resistances to the flow in each bifurcating channel, and with a periodic motion, it could result in an overall net flow. Table 7.1 illustrates the preliminary results I obtained when I tested different junction geometries shown in 7.10 and varied the order of connections to the T-junction. The results show appeared to show a conclusive effect on the flow characteristics due to the geometry.

To continue with my study, I proceeded to conduct analytic analysis of the experimental system in order to advance my study. Through the analysis, I was hoping to gain insight that would enable me to design a more effective experiment and uncover the mechanism underlying the net flow in the looped channel.

## 7.4 Analytic Analysis

I had to consider whether I could connect the physical scaling of the behavior I observed to my initial goal of studying glymphatic fluid flow. The most apparent distinction was that my experimental apparatus was much bigger, and thus assessing typical dimensionless parameters, such as Reynolds number, may point to the fact that the flow I was seeing was outside of the scope of the glymphatic mechanism.

For the experiment system, one can define the Reynolds number using the same definition as in a pipe, given that the flow occurs mostly in circular tubing. The Reynolds number is defined by equation 1.3, which can be rewritten as

$$Re_f = \frac{\mathbf{U}D}{\nu}, \tag{7.2}$$

where $\mathbf{U}$ is a characteristic flow velocity which we can define as the mean velocity of the flow in the pipe, $D$ is the diameter of the tubing which in this case is equal to 0.48 cm to 0.64 cm, and $\nu$ is the kinematic viscosity of water. The appropriate value of $\mathbf{U}$ to use is complicated. This is because the velocity in the pipe is not constant (it is time-dependent), and since the flow is divided into three different channels (TJ-1, TJ-2, IO as seen in figure 8.1), we have three different speeds as shown in figure 7.8.

I can determine a maximum Reynolds number by using the maximum measured speed, while this may not necessarily lead to a good scaling parameter for the system, it will give a conservative result in terms of what sort of flow behavior I can expect.

For the preliminary experiment, I measured particle velocities in the range of 13 cm/s to 1 cm/s, which yields an estimated maximum Reynolds number range between 1000 and 100. This value is fairly high when compared to estimates for the Glymphatic system, which is in the range of a Reynolds number in the order of

$10^{-3}$. However, this does not detract from the interesting flow observations, and it is still possible that the physics at play may extend to a lower Reynolds number parameter range. Another factor to consider is the Womersley number. The Reynolds number requires some characteristic velocity $U_T$, which can be difficult to define in an unsteady flow with multiple channels. However, for oscillatory flows, I can use the Womersley number across all the channels. The Womersley number is defined for my experiment as

$$Wo = \sqrt{\frac{2\pi f D^2}{\nu}} \tag{7.3}$$

where $D$ is the diameter of the tubing, $f$ is the frequency of the flow and $\nu$ is the viscosity of the fluid. My observations showed that the frequency remained constant throughout the entire system, even though the magnitude of velocities is different. The Womersley range was 38 to 6. This range is above what one ought to expect from the actual glymphatic system making the analogy more difficult to justify. It was clear from the preliminary findings that I was obtaining consistent directional flow, but in order to better study and relate the flow parameters to those of the glymphatic system, I would need an experimental device where I could control the parameters with more accuracy. One major limitation to achieving this was the dependency on material properties on the flow as I found in section 7.3. As such, I developed the final experiment design which I discuss in chapter 8.

## 7.5 Summary of Preliminary Findings

Based on my preliminary findings, it was possible to generate a directional flow in the passive channel that was not influenced by the flow direction in the active channel. However, the frequency of the flow in the active channel did affect the flow in the passive channel. Moreover, I discovered that having unequal tubing lengths between TJ-1 and TJ-2 was crucial for creating a net directional flow.

Furthermore, changes to the T-junction shape and connection pattern had a significant impact on the flow direction. These observations provided a foundation for further investigations of the system with an improved design.

# 8 Oscillatory Flow in Junctions: Final Study

Having performed preliminary experiments, I determined that adjustments to the experimental design were necessary. The main issue with the two-channel version of the experiment was that controlling the amplitude of the oscillatory flow in an accurate manner was not possible. The reason for this is due to the amplitude of the rubber membrane being tied to a resonant frequency; the details of this limitation are discussed in chapter 7. Due to this, my observations led me to test whether the same phenomenon could be reproduced by inducing an oscillatory flow in a different manner. I modified the experiment so that the oscillatory flow was produced by a syringe pump. This chapter focuses on this enhanced design and the resulting observations.

## 8.1 Experimental Device

My objective in redesigning the experiment was to create a device that would enable precise control of the oscillating flow's amplitude. To achieve this, I implemented a syringe pump system that allows for accurate amplitude control of the membrane. Rather than permitting the membrane to deform in response to pressure variations caused by the active flow channel in the previous experiment, which was not possible to control precisely, the syringe changes the volume in the closed system and forces the membrane's deformation to absorb the volume of fluid that is injected with the displacement of the syringe. This enabled me to accurately regulate the magnitude and frequency of the flow independently of the membrane's mechanical characteristics. A sketch of the updated version of the system is found in figure 8.1.

The updated experiment design consists of three primary components: a syringe pump, and a T-junction channel with a rubber membrane functioning as a pressure relief valve. This also added one key parameter to the control, which was the stroke (the total distance the syringe will travel over half a cycle) of the syringe $S$. The stroke refers to the maximum distance between the two points of oscillation of the syringe piston; thus the stroke of the syringe determines the amount of fluid that will be displaced from the syringe in a linear manner.

The updated experiment design included three components: a syringe pump, a T-junction channel with a rubber membrane as a pressure relief valve, and a key parameter in the control, the stroke of the syringe. The stroke of the syringe determines the amount of fluid that will be displaced linearly. The syringe pump consists of a stepper motor, which drove a threaded shaft connected to a linear stage. This allowed the stepper motor to accurately displace the syringe. For the purposes of this study, I only performed experiments using an oscillatory motion of the syringe pump. The syringe was a 100 ml plastic syringe with a diameter of 3.8 cm and was controlled by a Pololu AMIS-30543 stepper motor driver.

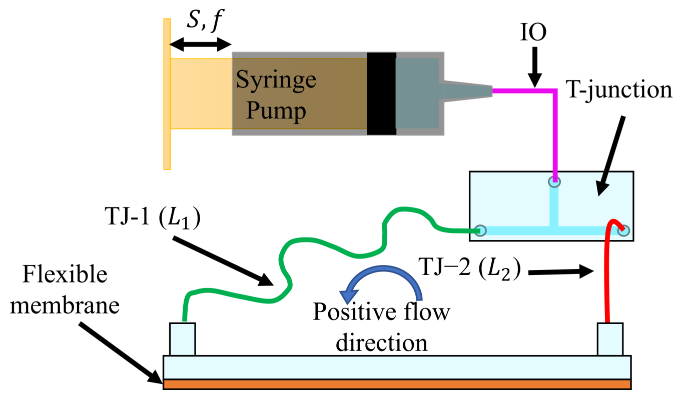


**Figure 8.1:** Sketch of the final experimental design. The system differs from the preliminary one (Figure 7.1) as it only has one looped channel. Flow is driven into the channel with a syringe pump and the membrane on the other end is allowed to deform to allow fluid into the loop. The two tubes are TJ-1 with a length of $L_1$ and TJ-2 with a length of $L_2$. The blue arrow indicates the positive direction of the flow.

The pressure relief membrane was unchanged from the preliminary experiment design seen in figure 7.2. The one exception was that one of the two channels was not used; it was simply open to the atmosphere. The system was filled with water and microspheres, except for one set of measurements (figure A.13) where the system was filled with glycerin.

I used two different T-junctions for the experiments. One of the T-junctions was acquired from McMaster-Carr part no. 5117K13 and is shown in detail in figure 7.3. The other was designed and fabricated by myself. My T-junction design consisted of a T-shaped channel that was laser cut into a sheet of acrylic, then sandwiched between two acrylic sheets to form a large see-through channel in the shape of a tee. Figure 8.2 is the schematic for the final design. The final design makes the critical difference where the channels are close in area dimensions to that of the connecting tubing. The reason for this is to attempt to minimize potential effects caused by a steep transition in the flow area between the tubing and T-junction.

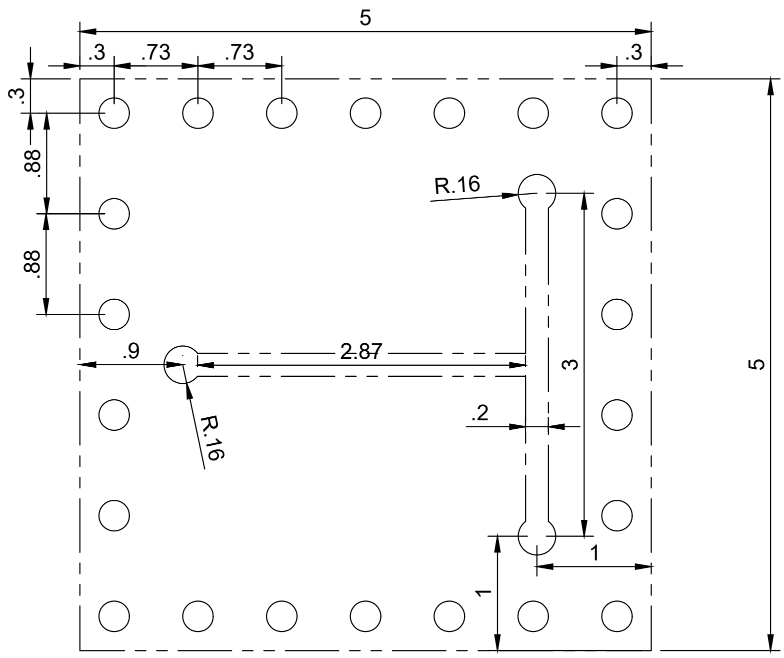


**Figure 8.2:** Schematic of the final T-junction design. This T-junction geometry was used for the final experiment where the junction was constructed to allow visualization of the flow inside.

## 8.2 Final Design Measurements

In this section, I present results from the updated experimental device. The updated design enabled me to acquire better data which allowed me to establish trends in the dynamics and identify key components of the flow mechanics.

I used the same techniques as in the preliminary experiment to determine the net velocity of the flow in the system as described in section 7.2. To quantify the net flow, I measured the net velocity of particles at a section in TJ-1 using Particle Tracking Velocimetry. Having refined my measurement techniques and approach for the second iteration of the experiment, I show examples of the measurements I performed in figure 8.3. Panel b) in the figure illustrates how the particles have an oscillatory motion, with some net motion over time. This visualization is intended to give an idea of how the bulk of lab measurements translate into the data presented later in this chapter.

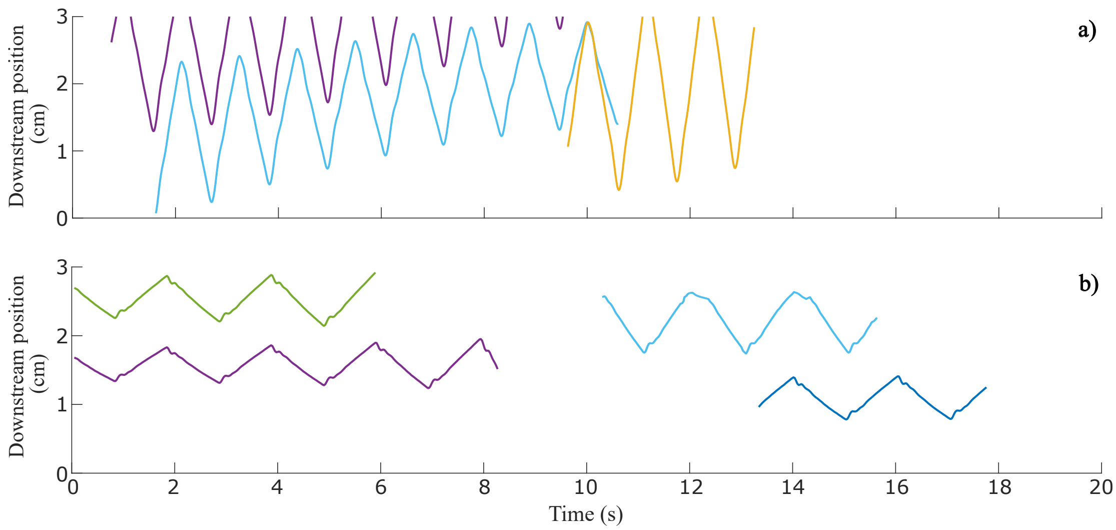


**Figure 8.3:** Downstream particle positions in a section of T-1, with each particle path colored differently. a) With parameters $f = 1$ Hz, $S = 2.0$ mm, $\gamma = 4$, $L_{tot} = 80$ cm, particles and the surrounding fluid have a net velocity, as they drift away from the visible area. b) With parameters $f = 0.5$ Hz, $S = 2.0$ mm, $\gamma = 4$, $L_{tot} = 80$ cm, particles oscillate without any net velocity.

Measurements of the net velocity $u_{net}$ for a large set of parameters are shown in figure 8.4. The parameters I tested were $S$, $f$, and $\gamma$ for the measurements in the figure. The net velocity measurements were performed at four or (eight in the case of panel c) in figure 8.4) different frequencies. I performed ten measurements at each frequency, and I plotted the average net velocity at each frequency. The error bars indicate the standard deviation of the ten measurements. The goal for this set of measurements was to determine which parameters are controlling the net flow. My hypothesis was that perhaps by picking different strokes, $\gamma$, or frequencies I could increase or decrease the net flow. I decided to test $\gamma$ as I hypothesized that the asymmetry created by the unequal lengths of $L_1$ and $L_2$ was a key component of the mechanism that produced a net velocity in the system.

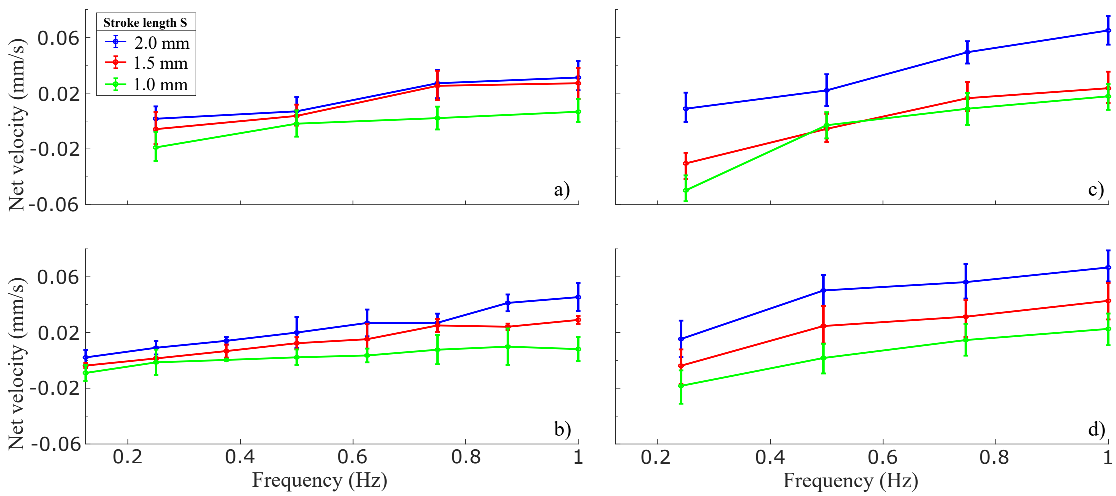


**Figure 8.4:** Shown in the figures are net velocity measurements measured at TJ-1 as a function of frequency. Each panel represents measurements with different values of $\gamma$, where a) $\gamma = 2$, b) $\gamma = 3$, c) $\gamma = 4$, and d) $\gamma = 7$. Each colored line represents a different value of Stroke $S$. The plots help establish trends in the system, where it can be seen that higher values of $S$ and $f$ lead to higher net velocities. It is also possible to have negative velocities in the case of small values of both $S$ and $f$.

The measurements shown in figure 8.4 show that there is a linear relationship between the magnitude of induced net flow and the stroke $S$, as well as between the induced flow and the frequency $f$. The direction of the flow is positive as shown in figure 8.1, which means that positive net flow would displace fluid from TJ-1, into the pressure relief membrane, and then into TJ-2. In each of the four panels, it was clear that a higher stroke at equivalent parameters yielded higher net velocities. However, one notable characteristic is that at lower $f$ and $S$, the flow direction was reversed. It was more difficult to establish a clear relationship between net flow and $\gamma$. Comparing results between the panels of figure 8.4 no clear trend was established as $\gamma$ was changed. However, the measurements of amplitude from figure 8.6 suggest that the ratio of the magnitude of speeds measured at TJ-1 and TJ-2 differ depending on $\gamma$. One consequence of having different velocities at each section of the junction is that defining a single Reynolds number for the system would be complicated, not just due to the time dependency, but also the fact that we have three channels that have three different peak speeds. Notwithstanding the challenges associated with accurately forecasting the behavior of a system using the Reynolds number, I note that the highest value of the Reynolds number represents the scenario where inertia maximizes its influence on the dynamics. The maximum Reynolds number is measured within the T-junction's segment that links to the syringe. As such the Reynolds number in the system is defined as

$$Re_T = \frac{2Sf\Lambda_{rr}D}{\nu}, \tag{8.1}$$

where $\Lambda_{rr} \approx 20$ is the ratio of the area of the syringe $\Lambda_{syringe}$ to the area of the tubing $\Lambda_{tubing}$, $D$ is the diameter of the tubing, and $2Sf$ is the average speed of the syringe.

Another parameter of interest is the observed amplitude of the particles' motion. From figure 7.5 and 8.3, one can see the oscillatory motion of the particles, from which it is possible to extract an amplitude. To define the amplitudes for the particle motion, I measured the maximum distance between two points over half a period of oscillation, but only considered the maximum value obtained from the experiment. It is worth noting that the velocity profile of the flow creates spatial variations in the amplitude. Therefore, limiting the analysis to the maximum measured value ensures consistency in the analysis. Specifically, I labeled the maximum amplitude for measurements at TJ-1 as $A_{TJ-1}$ and the maximum amplitude for measurements at TJ-2 as $A_{TJ-2}$.

Given that the main feature of interest of the system is its ability to produce a net directional flow from an oscillatory flow, I estimated the efficiency of producing a net directional flow from an oscillatory flow in the system using the same methodology as described by [12]. I calculated the efficiency of producing a net flow by employing

$$E = u_{net}/(2A_{TJ-1}f). \tag{8.2}$$

The average particle speed in TJ-1 can be calculated as $(2A_{TJ-1}f)$. Equation 8.2 provides a ratio of energy input and output, with the input being the oscillating flow caused by the syringe, and the output being the net flow produced. Figure 8.5 illustrates the relationship between frequency and efficiency. The analysis showed that the highest absolute efficiency was achieved at lower frequencies, which was associated with a negative net flow direction. As the frequency increased, the efficiency declined until the net flow became positive. Subsequently, the efficiency increased, but slower than in the negative regime and with high diminishing returns.

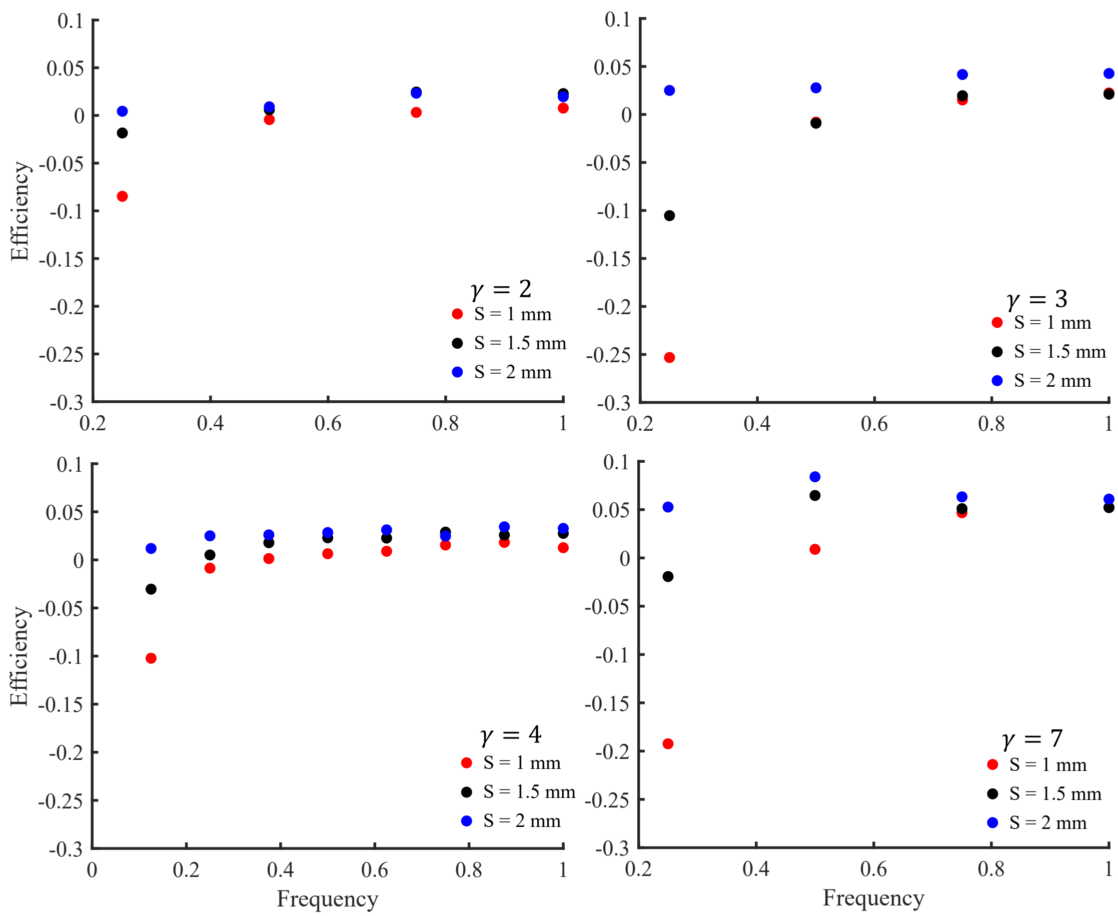


**Figure 8.5:** The data presented in the figures demonstrate the efficiency of generating a net flow through a calculation. Notably, the lowest frequencies are associated with the highest absolute efficiency.

Another important feature that I was able to analyze using the amplitudes of particles was the maximum average speed. The maximum average speed at the channel $s$ as

$$s_{TJ-1} = 2A_{TJ-1}f. \tag{8.3}$$

The maximum average speed $s$ is a useful parameter for validating my observations. Note that the maximum average speed and maximum amplitude are considered to be the maximum that is measured, just as in the case of amplitude. To conduct experimental measurements, I selected the ten longest particle paths in terms of duration for each experiment I performed. For each path, I extracted the maximum speed at every half-cycle and calculated the average of these values to obtain ten measurements. The highest value among these measurements represents the experimentally measured maximum average speed. Since the highest quality measurements were typically obtained near the center of the tubes where speeds were maximized, the values of the ten measurements did not differ significantly, usually less than a 5% difference. This method worked well in my experiment because the oscillations resembled a triangle wave, as depicted in Figure 8.3. To understand what the maximum average speed $s$ says about the system, consider the experiment in a steady-state scenario, where instead of an oscillatory flow, the flow is one where the syringe continuously injects fluid. For the case where $L_1 = L_2$, one can easily estimate the maximum average speeds at each tube $s_{TJ-1}$ and $s_{TJ-2}$. All we need is the inlet (or syringe) flow speed. For my experimental system, one can estimate $s_{IO}$ from the parameters of the syringe. The syringe pump produces a maximum average flow rate that is equivalent to $Q_{syringe} = s_{syringe}\Lambda_{syringe} = 2\Lambda S f$. Due to continuity, we can calculate that the same maximum average flow rate must be maintained through the rest of the system, thus flow at the IO channel must be $Q_{syringe} = Q_{IO}$. I can estimate the speed at IO as $s_{IO} = s_{syringe}\Lambda_{syringe}/\Lambda_{tubing}$. Then the flow must split evenly between the two symmetric channels, meaning that $s_{TJ-1} = s_{IO}/2$.

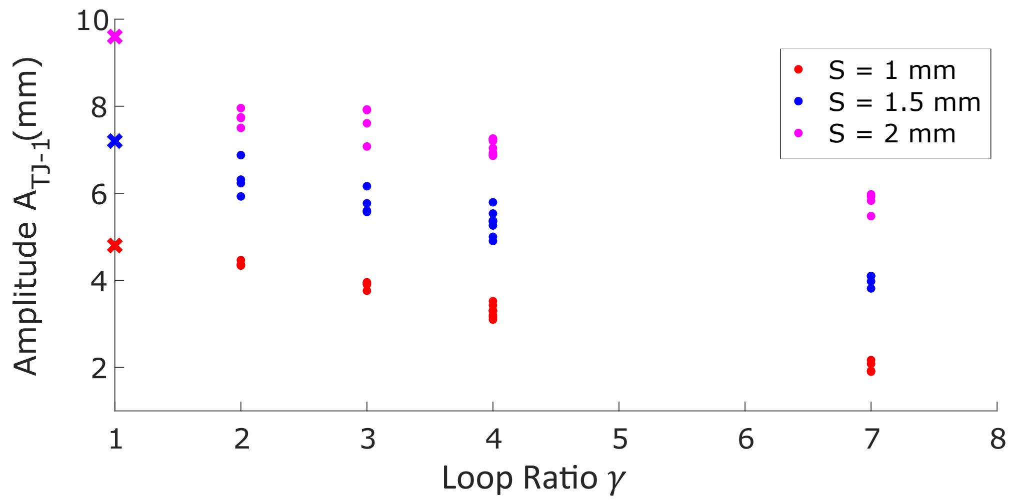


**Figure 8.6:** Shown is a plot of the maximum amplitude measured at TJ-1 versus the loop ratio $\gamma$. The total loop length was $L_{tot} = 80$ cm. Each of the colors represents a different value of $S$. The scatter clearly shows how the amplitude increases as $\gamma$ decreases. The values also converge towards the expected amplitude as $\gamma \to 1$. The expected amplitudes are plotted as exes.

In the case of an asymmetric channel setup, where $L_1 \neq L_2$, the final step in this relationship is not straightforward. From my observations in the preliminary section 7.3, the speed of the fluid is overall lower at TJ-1 compared to TJ-2. This is not surprising as TJ-1 should produce more resistance than TJ-2 to the flow towards the membrane due to its longer length. Given this observation, it is not possible to use the same simple analysis to predict values of $s_{TJ-1}$ and $s_{TJ-2}$.

However, it provides a valuable tool to verify measurements. Since $L_1 > L_2$, then it follows $s_{TJ-1} < s_{TJ-2}$. As a consequence, $A_{TJ-1} < A_{TJ-2}$ to compensate for the speed differential, and as $\gamma \to 1$, we should see both measured amplitude $A_{TJ-1}$ and $A_{TJ-2}$ converge to the same value as the one estimated in the symmetric case. Measurements of the amplitude at TJ-1 in the experiment and shown in figure 8.6, show a clear trend that converges towards the expected value as the loop ratio trend to one ($\gamma \to 1$). For my system where $\gamma = 1$, the expected amplitude at TJ-1 for $S = 1$ mm is $A_{TJ-1} = 4.8$ mm, $S = 1.5$ mm is $A_{TJ-1} = 7.2$ mm, and $S = 2$ mm is $A_{TJ-1} = 9.6$ mm. Furthermore, the results from figure 8.6 suggest that the dominant factor in viscous losses in the system is the long tubes, not the T-junction. I observed that as the stroke $S$ drops, so must the maximum average speed in the tube since the speeds at the tubes are defined as $s_{TJ-1} = 2A_{TJ-1}f$.

I attempted to model the phenomenon where a drop in speeds and amplitudes is linked to the loop ratio $\gamma$. I used the following model, where I consider two-dimensional steady viscous flow in a T-junction shown in Figure 8.7. In the experiment the maximum Reynolds number flow I modeled was approximately 1000, given this, I found it adequate to model the steady flow using Poiseuille flow. The boundary conditions are the following: The inlet imposes a flow rate $Q^*_{in}$ and the two outlets have a pressure condition where they both are at atmospheric pressure $P_{atm}$. Given that a flow rate is imposed at the inlet, one can consider the equivalent as the inlet imposes a pressure $P_0$ which achieves a flow rate $Q^*_{in}$ at the inlet. From Poiseuille flow theory we know that a pressure difference is defined as

$$\Delta P = \frac{8\mu l Q^*}{\pi R^4}, \tag{8.4}$$

where $\Delta P$ is the pressure difference between the inlet and outlets ends, $Q^*$ is the flow rate, $\mu$ is the dynamic viscosity of the fluid, $l$ is the length of the pipe, and $R$ is the radius of the pipe. The relationship of pressure loss is linear with the pipe length and is the only parameter we have changed. Since the pressure is equivalent at the end of each of the two channels in the simple model, then it follows

$$Q^*_1 l_1 = Q^*_2 l_2 \tag{8.5}$$

or

$$Q^*_2 / Q^*_1 = l_1 / l_2 \equiv \gamma. \tag{8.6}$$

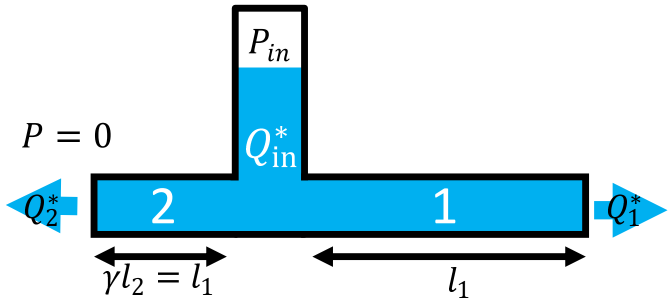


**Figure 8.7:** Shown is a sketch of the analytic model. The model considers steady flow at a two-dimensional system of three channels connected by a T-junction. The perpendicular channel imposes a flow rate, simulating the conditions of the syringe pump. The two outlet channels are labeled as 1 and 2, they have their own respective lengths and are open to the atmosphere. Each channel's flow rate is described by $Q^*$ with their respective label.

This result is consistent with the measurements shown in figures 7.8 and figure 8.6, as all three demonstrate that $\gamma$ is linked to the ratio of flow rates between TJ-1 and TJ-2. However, they do not provide insight into what the mechanism driving the net flow in the loop was. Given this, I reviewed literature that appeared to have similar systems as mine in chapter 6.

The similarities between Nguyen et al. [12] and my observations prompted me to perform experimental observations at the T-junction in hopes of observing the same flow characteristics they had observed. A key takeaway from this analysis was to observe how the flow at the T-junction differed over the cycle. That is, what does the flow look like when the syringe is injecting fluid into the system (which I call the *push* cycle), versus when the syringe is pulling fluid from the system (which I call the *pull* cycle).

### 8.2.1 Measurements at the T-Junction

I conducted an experiment to test the hypothesis that the geometric properties of the T-junction are responsible for inducing a flow. To do this, I changed the geometry of the T-junction by swapping the connections at the T-junction, as illustrated in figure 8.8. This was the same approach as what was conducted in the preliminary study, but this iteration of the experiment allowed me to visualize the effects on the flow at the junction.

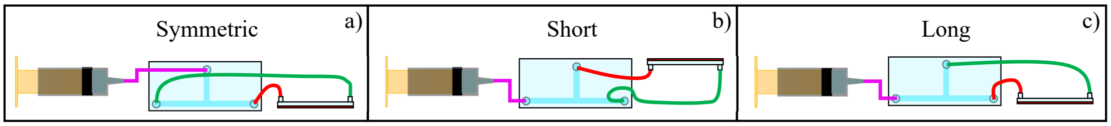


**Figure 8.8:** Sketches of the three configurations that were tested. a) The *Symmetric* configuration connected the central arm of the T to the syringe pump (IO). b) The *Short* configuration connected the central arm to the short tube (TJ-2). c) The *Long* configuration connected the central arm to the long tube (TJ-1).

Figure 8.9 shows net velocity measurements for each of the different geometric configurations shown in figure 8.8. The measurements were performed in the same manner as those for figure 8.4. Plotted measurements are the average of measured net velocity for ten different measurements. The error bar is the standard deviation of the measurements. The most important result of the experiments was that I was able to reverse the direction of the net velocity in one configuration. This agreed with my preliminary observations and confirmed that the geometric conditions of the loop created a net flow.

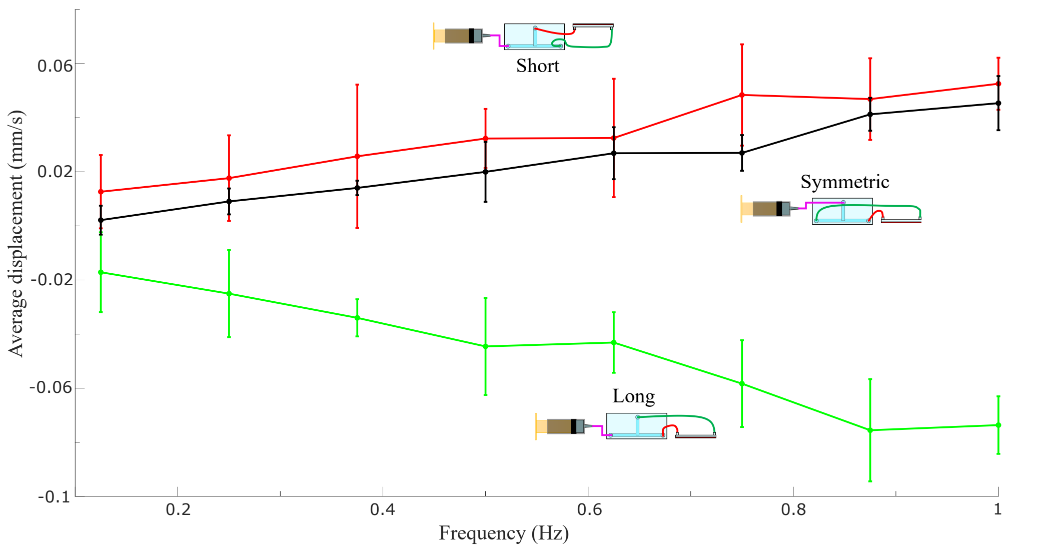


**Figure 8.9:** Measurements of the net velocity in a section of TJ-1 for different interconnection configurations. For the *Long* configuration, the direction of the flow is reversed. The effects of $S$ and $f$ on the magnitude of the net flow remained the same as shown in figure 8.8.

I employed a rheoscopic fluid solution, which can be made using Barbasol [61], to visualize flow patterns in the system without needing additional analysis tools. When conducting measurements, I focused on visualizations at one of three key areas, a section of TJ-1, a section of TJ-2, or the T-junction. Figure 8.10 shows various images of the flow at the T-junction, which revealed the formation of a stagnation line where the flow bifurcated from one channel to two. This line acted as a separatrix, dividing two sections of the flow. The separatrix remained centered in the case of a symmetrical loop, but shifted towards the longer tube (TJ-1) in the loop with unequal tubing lengths, likely due to the lower resistance for fluid to move towards the shorter tube (TJ-2). Additionally, the location of the separatrix was not constant over time, as it shifted over the cycle, indicating that the flow paths were different when fluid was pushed into the loop, versus when it was pulled out of the loop. This temporally asymmetric reaction was likely the mechanism driving net flow as it suggests that flow resistance is variable over time and space allowing for a form of valving effect in the system.

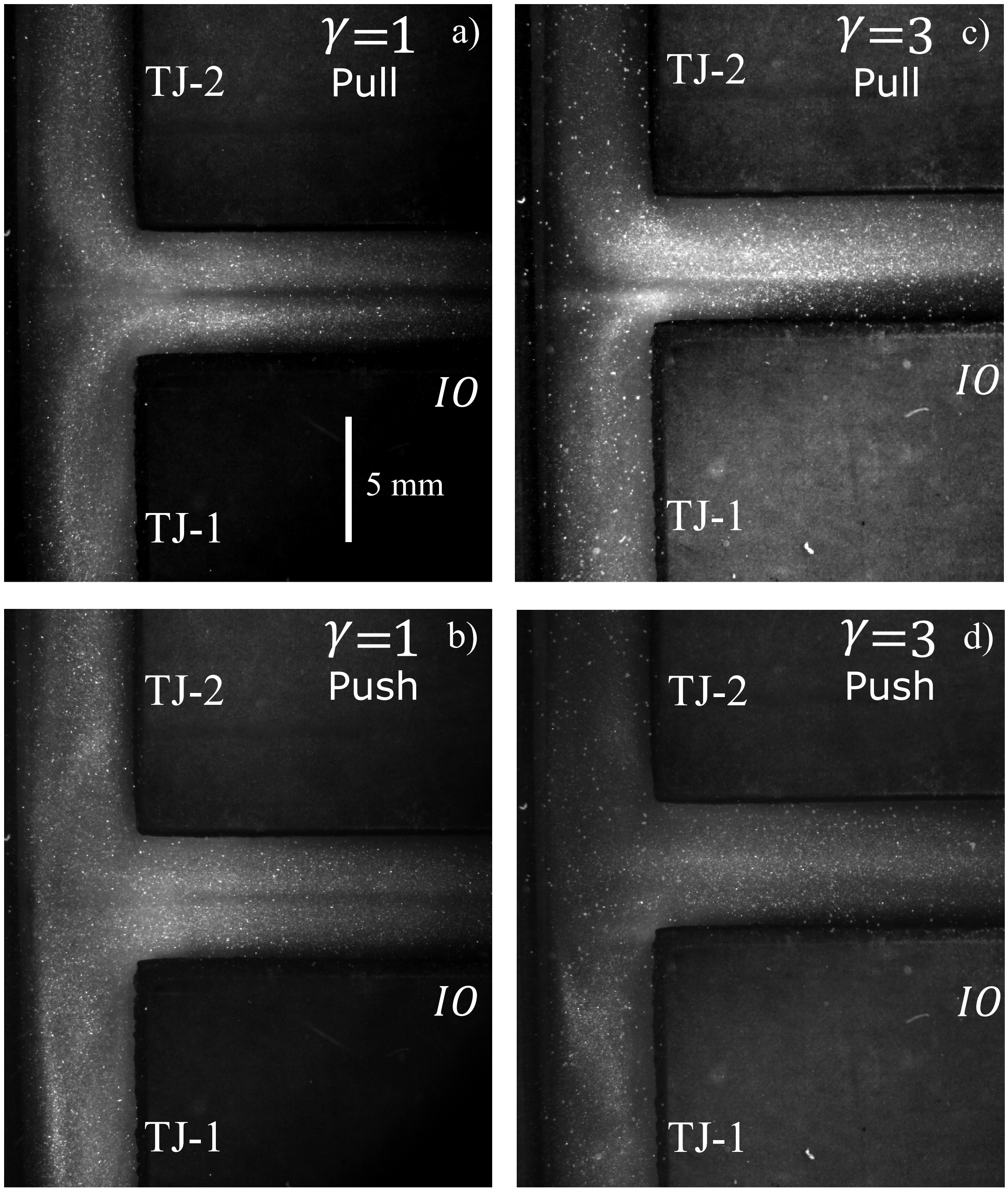


**Figure 8.10:** Visualizations of the flow at the T-junction during the *push* and *pull* portions of a cycle for two configurations: $\gamma = 1$ and $\gamma = 3$. Dark regions indicate flow separation, which is located in the center of the symmetric $\gamma = 1$ configuration and shifted towards the inlet of TJ-1 for the asymmetric $\gamma = 3$ configuration. This indicates that changing $\gamma$ induces an asymmetry in the flow. Reynolds number as defined by equation 8.1 was 30 for all cases shown.

In order to better measure the effect of the separatrix, I performed PTV measurements at the T-junction which yield more quantitative measurements than rheoscopic visualizations. Although PIV measurements were initially attempted, they proved to be unsuccessful due to the absence of tools capable of measuring a two-dimensional sheet of the fluid, similar to the method employed in chapter 5, they were unsuccessful. Therefore, PTV was used as it is more forgiving in this scenario. The measurements obtained are shown in figures 8.11 and 8.17.

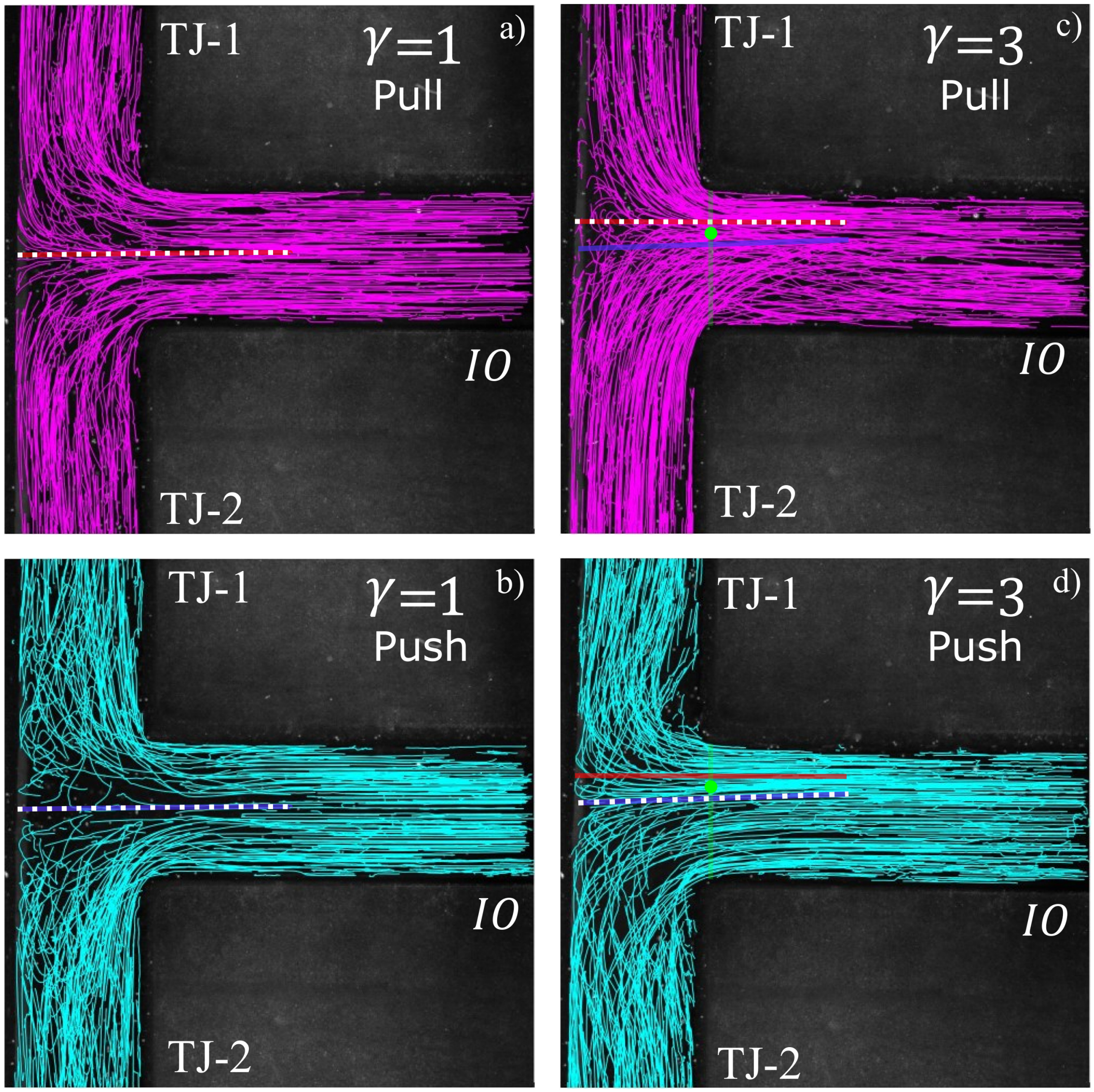


**Figure 8.11:** The particle paths at a T-junction for two configurations at two different stages of the cycle have been analyzed. Magenta lines indicate paths occurring during the *pull* part of the cycle, while cyan paths indicate the *push* part. Blue and red curves mark the approximate location of the separatrix for each part of the cycle. The green line is the width of the channels, and the green circle is the analytically approximated separatrix location. Reynolds number as defined by equation 8.1 was 30 for all cases shown.

Figure 8.11 replicates the conditions presented in figure 8.10, but the fluid was filled with particles for PTV measurements. The measurements shown are particle paths divided into the *push* and *pull* sections of the cycle. The measurements clearly indicate the location of the separatrix at each section of the cycle, and confirm the qualitative measurements from figure 8.10. The separatrix does not change location in the case of the symmetric configuration $\gamma = 1$, which is expected given that we always expect both connecting channels (TJ-1 and TJ-2) to have the same velocity. In the case of the asymmetric configuration $\gamma = 3$, I observed that the separatrix position was always closer to the tube with higher resistance (TJ-1) and the separatrix changed position over time.

In an attempt to characterize the position of the separatrix, I revisited the model from earlier in this section delineated in figure 8.7. By taking into account the experimental speed measurements portrayed in figure 8.6 and preliminary speed measurements depicted in figure 7.8, I have been able to demonstrate that a portion of the flow properties can be replicated by considering the steady-state Poiseuille flow. Consequently, I attempted to determine the location of the separatrix utilizing the same model. While my two-dimensional model is not an exact replica of the T-junction experiment, it should still be able to capture the dominant flow dynamics with less complexity when compared to a three-dimensional model. Additionally, a two-dimensional model made it feasible for me to perform simulations for various parameters, as it is much less computationally intensive than a three-dimensional model.

Since the velocity profile of plane Poiseuille flow $u_{Poi}$ follows a simple parabolic function of the form $u_{Poi} = U_{s1}x^2 + U_{s2}$, where $x$ ranges from some value $-b$ to $b$, and $U_{s1}$ and $U_{s2}$ are constants that determine the velocity magnitude, I posed the following question: To ensure that the flow rate is properly divided between the two outlets, creating a separatrix or separation line, which segment of the inlet velocity profile is required to meet the flow rate demands of each outlet? To answer this question first consider that mass conservation states

$$Q^*_{in} = Q^*_1 + Q^*_2. \tag{8.7}$$

Equation 8.7 can be rewritten as

$$D_c \bar{u_{in}} = D_c \bar{u_1} + D_c \bar{u_2}, \tag{8.8}$$

where $D_c$ is the two-dimensional channel gap width, $\bar{u_{in}}$ is the mean velocity at the inlet, $\bar{u_1}$ is the mean velocity at outlet-1 and $\bar{u_2}$ is the mean velocity at the outlet-2. From equation 8.6 and equation 8.8 I can write

$$\bar{u_{in}} = (1+\gamma)\bar{u_1}. \tag{8.9}$$

The flow rate at the inlet is obtained via the spatial integration of the velocity field as

$$Q^*_{in} = \int_0^{D_c} u_{in} dx_c, \tag{8.10}$$

where $dx_c$ is the space in the cross-stream direction of the inlet. To visually interpret what this integral is considering, see figure 8.12, where the purple line is the line over which the integral is considered. From here I can use equations 8.9 and 8.10 to obtain an expression where I sought the flow rate distributed to outlet-1 as a function of the flow profile of the inlet velocity profile. In other words, I seek what section from 0 to an unknown position $D_a$ of the inlet velocity profile will equal the flow rate at outlet-1. The equation is

$$Q^*_1 = D_c \frac{\bar{u_1}}{1+\gamma} = \int_0^{D_a} u_{in} dx_c, \tag{8.11}$$

which is

$$\frac{D_c^3}{6+6\gamma} = \int_0^{D_a} x_c(D_c - x_c) dx_c. \tag{8.12}$$

Integrating then yields

$$\frac{D_c^3}{6+6\gamma} = \frac{D_c D_a^2}{2} - \frac{D_a^3}{3}. \tag{8.13}$$

Solving equation 8.13 for $D_a$ yields multiple potential solutions. However, only one should fall will fall in the range of reasonable answers, where $0 < D_a < D_c$. $D_a$ represents the position at the inlet velocity profile where the separatrix should be positioned. It is also important to note that this prediction only considers the position at the inlet of the square section that makes up the T-junction, the separatrix in reality extends further upstream as shown in experimental measurements such as in figure 8.10.

To determine the validity of my analytic approach to estimate the separatrix position I used numerical simulations using ANSYS Fluent. ANSYS Fluent is a commercial computational fluid dynamics software package developed by ANSYS. Fluent is widely used for simulating fluid flows in research. Fluent utilizes numerical methods to solve the equations governing fluid flow.

Figure 8.12 illustrates a simplified view of the model I simulated, which consists of three elongated two-dimensional channels interconnected by a T-junction. The size of the channel is defined by $D_c$. To compare with the experimental model, I utilized values of $D_c = 5$ mm, and for numerical validation, I also utilized $D_c = 20$ mm. For the purpose of my study, I considered two distinct combinations of boundary conditions. Specifically, as depicted in Figure 8.12, the inlet boundary condition (highlighted in red) was either a velocity inlet with a specified velocity of 5 mm/s or a pressure outlet set at zero pascal. In turn, the outlet boundary condition (shown in green) was either a pressure outlet at zero pascal or a velocity inlet with a specified velocity of $5\gamma/(\gamma+1)$ mm/s for outlet-1 and $5/(\gamma+1)$ mm/s for outlet-2. Given that the maximum Reynolds number for my experiments was 1000, I employed the laminar model in Fluent and utilized the steady-state solver to derive the results.

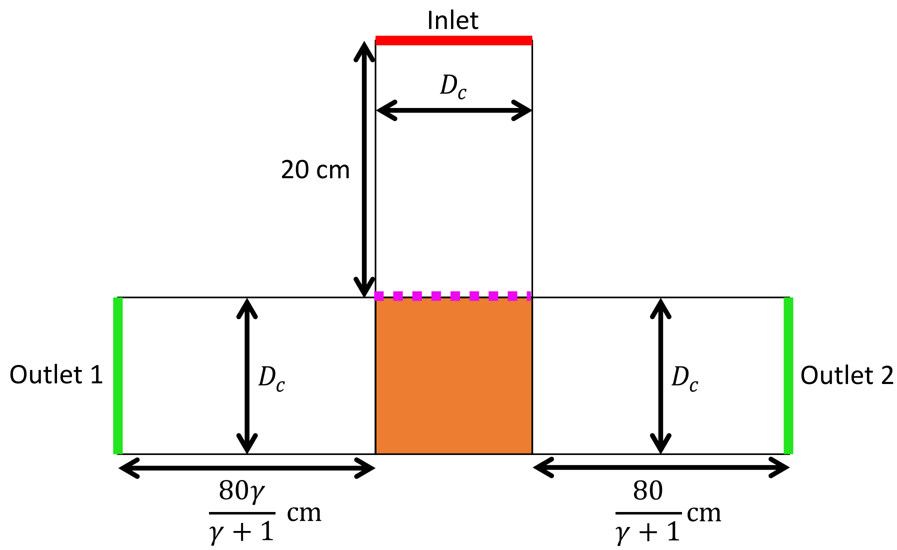


**Figure 8.12:** This is a simplified view of the model I simulated using Fluent software. I created a two-dimensional T-shaped connection with long channels attached to it and labeled the distances between them. The width of the channels is represented by the variable $D_c$. The orange section at the junction is where I focused on understanding the separatrix position, which is where the flow splits into two channels at the purple dotted line.

I show in figure 8.13 streamlines for the different simulations that were run using $D_c = 5$ mm. Of particular interest is panel c) and d) which are comparable to the experimental results presented in figure 8.11 and show similar results. Notably, the earlier experimental measurements with $\gamma = 3$ from figure 8.11 revealed that the separatrix changes position depending on the phase of the oscillatory flow cycle. This characteristic is also present in shown steady-state simulations which can be seen when comparing panels in figure 8.13.

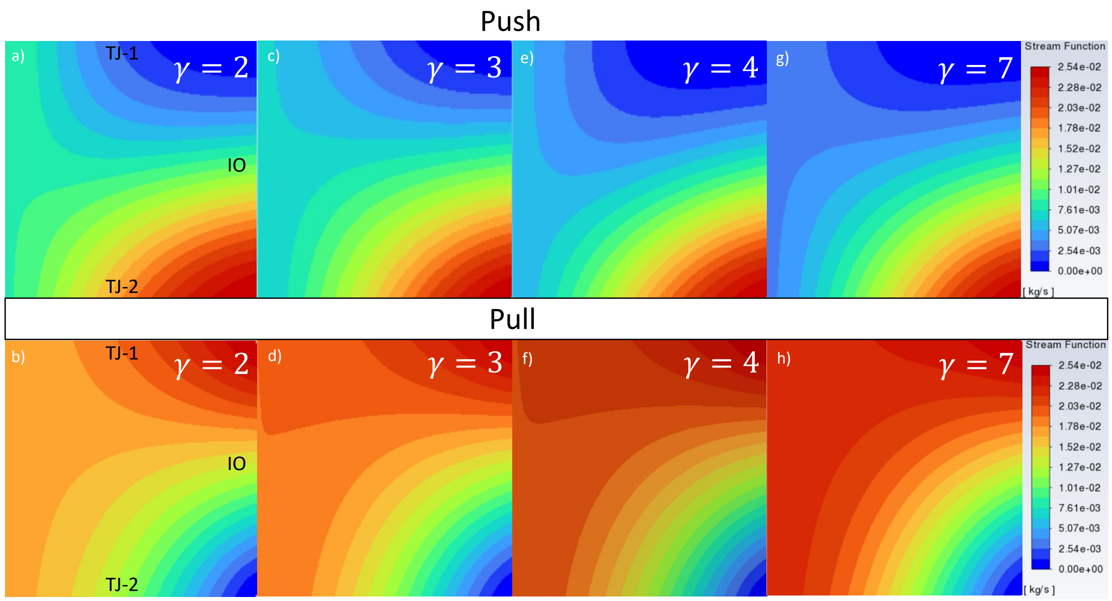


**Figure 8.13:** The numerical calculations shown in the figures depict streamlines for various $\gamma$ values, based on the model illustrated in Figure 8.12, with a Reynolds number of 30. The visualized area of interest is specifically the region highlighted in orange in Figure 8.12. The position of the separatrix is determined by extracting the position where the streamlines divide the flow between outlets/inlets along the purple line.

I compared numerical and analytic separatrix positions as shown in figure 8.14. Although the analytical model is not entirely consistent with the numerical simulations or experiment measurement, it accurately reflects the dependence of the separatrix position on $\gamma$. Specifically, during the *push* phase of the cycle, the position is closer to the longer tube (TJ-1), while during the *pull* phase of the cycle, the separatrix moves closer to the middle. When comparing the position during both cycle phases with the analytical model, as illustrated in figure 8.15, it is evident that the steady model predicts a separatrix position between the two phases measured in the experiment. This is likely due to the model's inability to account for losses induced by flow dynamics at the T-junction since it assumes that pressure differences are solely determined by the length of the tubes. Furthermore, it indicates that the flow resistance is temporally asymmetrical.

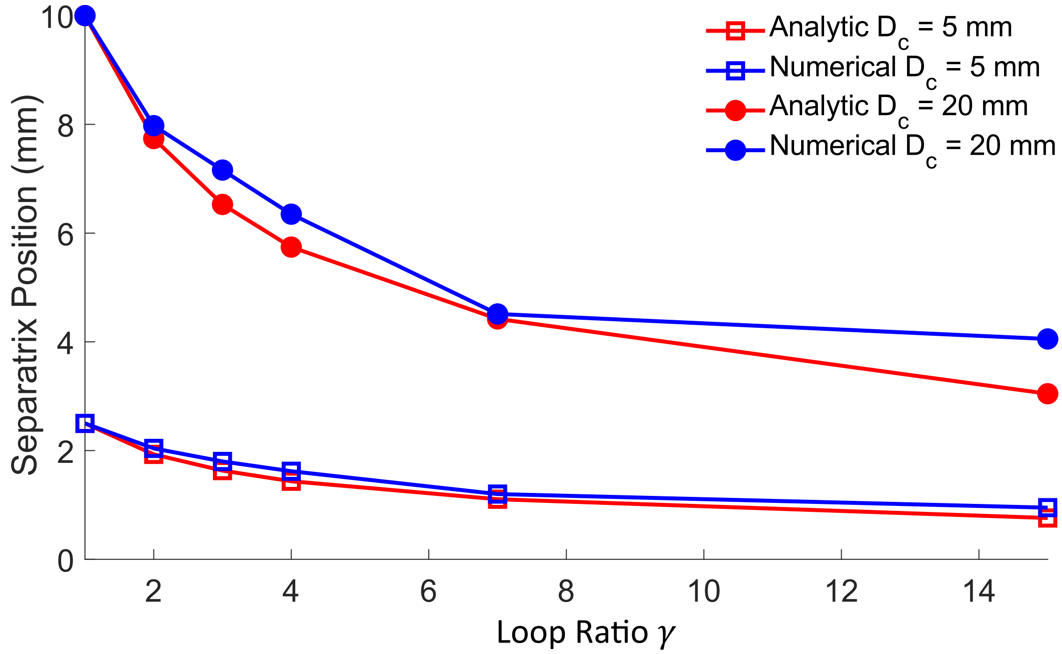


**Figure 8.14:** Shown is a plot of the estimated separatrix position from the analytic model and numerical simulations. Two cases are shown, one is for a system where the channel gap $D_c$ matches that of the experiment (5 mm), and another is $D_c = 20$ mm in order to test the sensitivity to changes in $D_c$. Reynolds number was held at $Re_T = 30$ to match experimental values. The comparison shows the model is perfectly accurate, however, it captures the relationship between $\gamma$ and the separatrix position well.

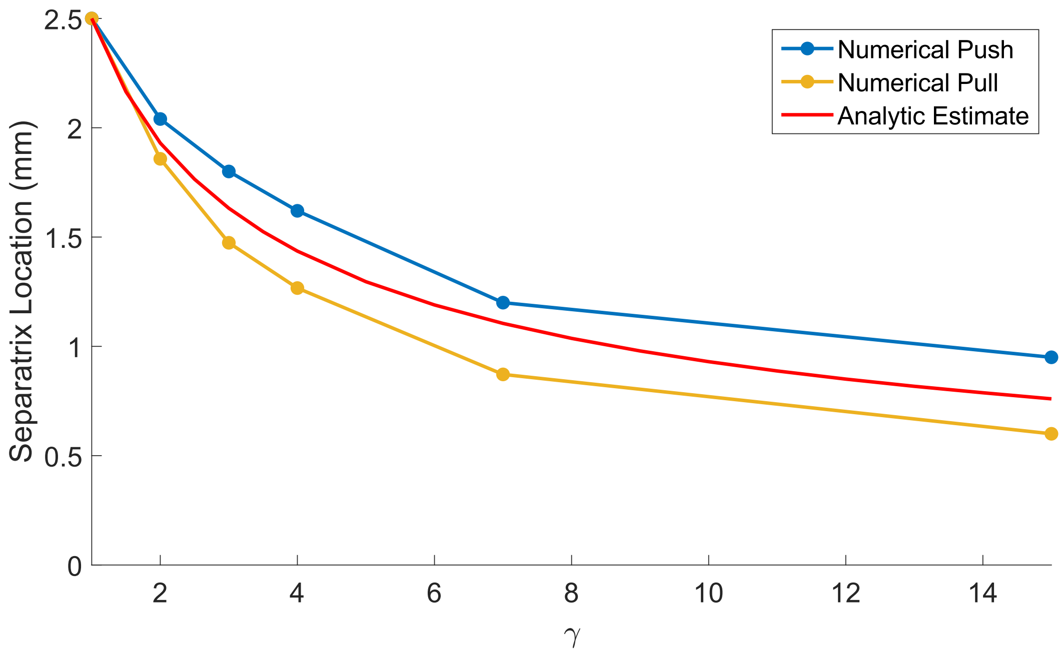


**Figure 8.15:** The present illustration presents a comparison between the analytically estimated separatrix position for a given $\gamma$ and the numerically measured separatrix position during the *pull* and *push* phases for a given $\gamma$. It is noteworthy that the analytic model predicts a position that lies between the two while correctly reflecting the impact of $\gamma$. This suggests that the model captures only a partial view of the dynamics, as the discrepancy is likely attributable to dynamics caused by the T-junction that are not accounted for by the Poiseuille flow model.

In addition to the previous results, I performed a test to determine the effect of different values of Reynolds numbers on the separatrix position. Figure 8.16 shows the streamlines of three different values. The figure demonstrates that varying the Reynolds number did not appear to trend in a specific manner or produce large changes for the Reynolds number range of my experimental measurements ($10 < Re_T < 1000$).

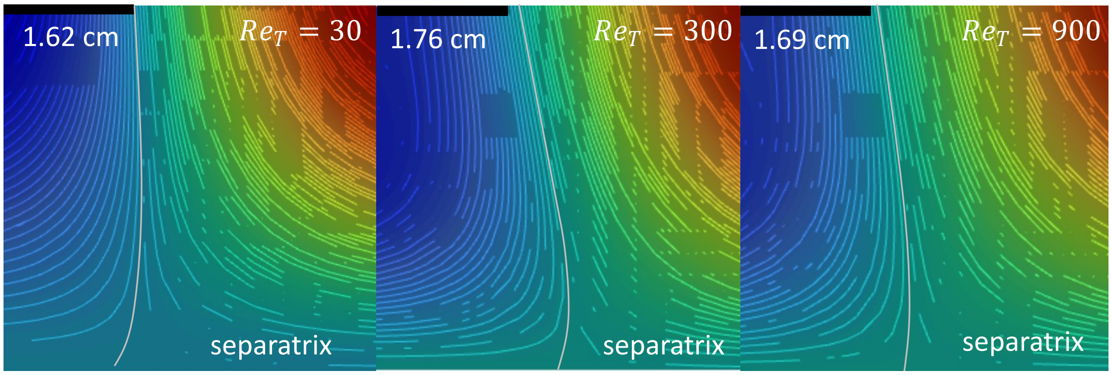


**Figure 8.16:** The figure illustrates a comparison of three streamlines obtained using Fluent software, specifically at the T-junction section. In each case, we set $D_c = 5$ cm and $\gamma = 3$, while varying the Reynolds number as labeled. The top left of each panel indicates the position of the separatrix at the inlet location.

To summarize, I have found that although the measurements and modeling of the separatrix did not offer an explanation of the mechanism behind the net flow, they do emphasize the significance of time-dependent dynamics on the observed flow. Moreover, the steady-state model only provides limited information regarding the system, such as the location and trend of the separatrix, but it fails to provide comprehensive insight into the intricate behavior at the T-junction. Therefore, comprehending the T-junction dynamics is crucial in characterizing the net flow in the loop.

From these observations, it became evident that the asymmetric flow resistance in the channel played a major role in the dynamics. It was clear that the different geometric configurations shown in figure 8.8 would have a strong effect in producing an asymmetric resistance to the flow. This made sense in cases where IO was aligned with TJ-1 or TJ-2. The flow inertia would make the flow prefer the path towards the channel that was aligned, instead of turning to the other channel. The following visualizations showed this effect and provided further insight into why the flow had been observed to reverse as shown in measurements in figure 8.9.

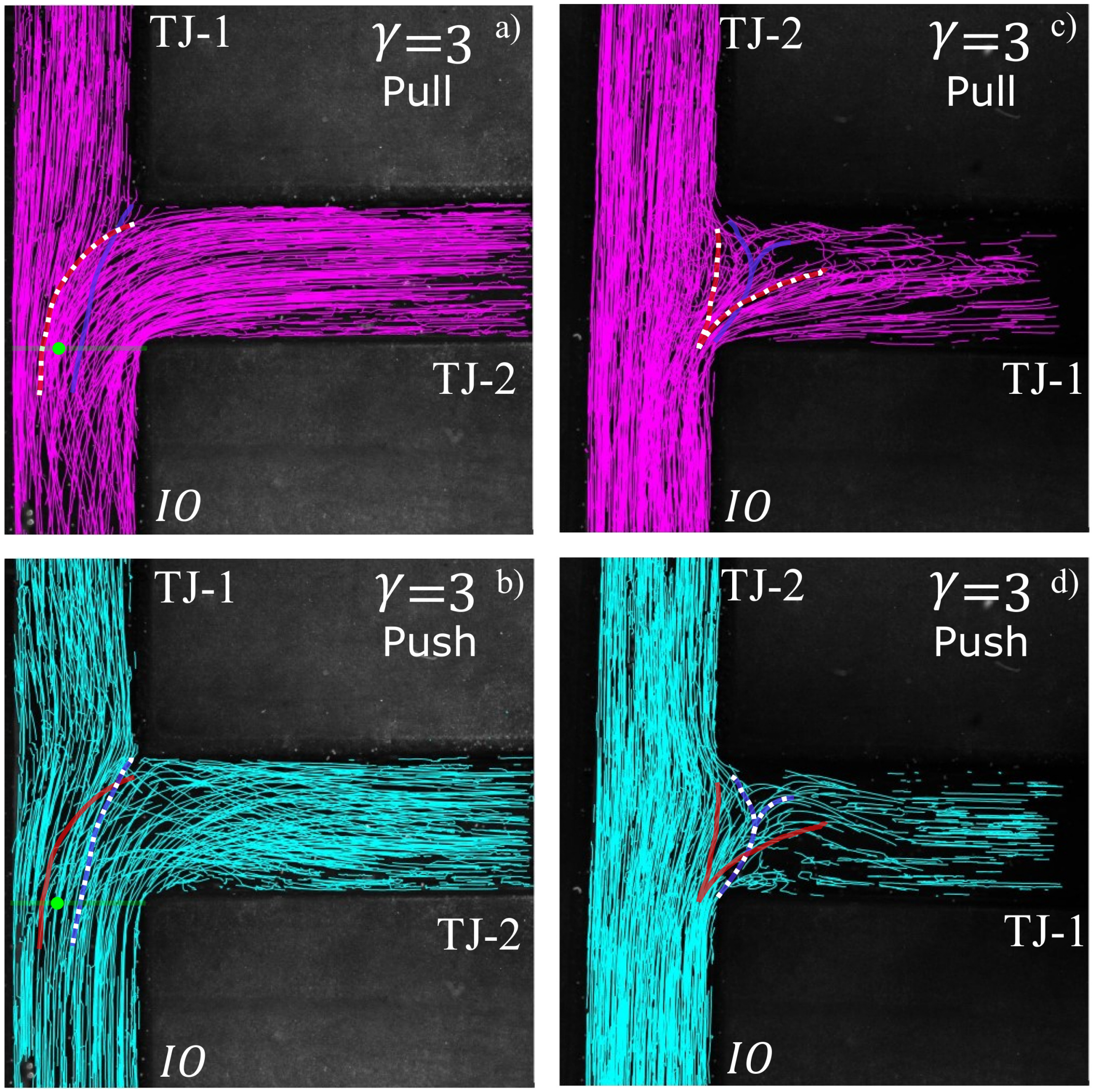


**Figure 8.17:** The particle paths at the T-junction for both the *short* and *long* configurations are marked in magenta and cyan, respectively, to indicate whether they occur during the *pull* or *push* part of the cycle. Blue and red curves give an approximate location of the separatrix for each part of the cycle. Overall, the different directions of flow create a net velocity in the loop. The green line is the width of the channels, and the green circle is the analytically approximated separatrix location.

Measurements for the *short* and *long* configurations described in section 8.8 are shown in figure 8.17. The separatrix over the *push* and *pull* cycles are significantly more different for these configurations. Particularly, the *long* configuration has different flow patterns between each section of the cycle. Notably, it appears that in the of the *short* configuration, I am able to approximate the position of the separatrix of the *short* configuration using the same methodology that I used for figure 8.11. Note that I did not perform any special treatment for the change in the configuration, as the analytic model cannot take into account the angle of the outlets with respect to the inlet. As such, the estimated position for the *short* configuration is the exact same as that for $\gamma = 3$ and $D_c = 5$mm in figure 8.11. The *long* configuration is not approximated well. This is likely due to the fact that the geometry of the flow is a dominant factor in increasing resistance to the flow, not just the tube length. During the *push* cycle, few particles travel towards TJ-1, while during the *pull* cycle, the particle flow is more evenly distributed. This finding would explain why the flow direction is reversed and seems to point towards an asymmetric resistance in flow depending on the section of the cycle.

These findings confirm that comprehending the temporal dynamics of the flow at the T-junction is critical for understanding the observed net flow inducing mechanism in the loop. While I was able to estimate the position of the separatrix and capture some effects of the tube length asymmetry, the simulations demonstrated that the analytic model falls short in reproducing all the steady-state features, let alone accounting for vortex formation caused by temporal variations in the flow velocity.

## 8.3 Summary of Findings

It would appear that the mechanism behind the valving effect is due to the separation of the flow, as observed numerically by Nyguen et al. [12]. It is not easy to identify a straightforward model to explain the transition to unstable flow and flow separation in a fluid system. To illustrate this point, consider flow in a pipe, where we have a relatively simple system and have developed some guidelines to predict instability of the flow [62]. In our particular case, we employed a junction geometry that was not limited to a singular geometric condition, coupled with a time-dependent flow exhibiting oscillatory behavior. The experimental observations I presented highlight the significant role of the junction in generating a net flow within the system. The characteristic flow pattern is consistent with findings from previous studies of flow in T-junctions, which have established that vortex shedding can induce complex dynamics in particle transport [63, 64]. Moreover, the sensitivity of vortex formation to the angle of the junction has been noted in prior research on T-junction flows [65]. This may explain how altering the configuration of the connections at the T-junction can result in different flow characteristics, as demonstrated by the experiments in this chapter. Different configurations, as illustrated in Figure 8.8, led to distinct net flows, as evidenced by Figure 8.9. Furthermore, the geometry of the junction itself had an impact on the flow, as demonstrated in Chapter 7.3 and summarized in Table 7.1.

Despite this, an understanding of this mechanism holds great value in both engineering applications and systems featuring looped channels and bifurcations. In particular, this mechanism may prove beneficial in biophysics scenarios, as demonstrated in the preliminary study where a peristaltic driven channel was shown to potentially induce flow on a non-driven channel. Moreover, it may also have utility in fluid logic chips where the ability to rectify an oscillating flow or vice versa, represents a valuable application [66]. It may be possible to model with some success using nonlinear resistance models such as those used in related studies looking at networks of channels some of which can be found in [56–58, 67], although the models likely will require modification to meet the looped conditions in some cases.

I did not study the case of highly viscous flows in detail and limited myself to only one set of measurements (figure A.13), however, the results do show some flow was produced. While this may seem counter to the separation mechanism that appears to be the source of pumping, it was shown in [12] that in that parameter regime, a flow can still be generated. The likely source is that separation at complex geometry channels with oscillatory flows can occur at low Reynolds numbers, i.e. lower values than $Re_T = 1$, as discussed in [60].

# 9 Conclusion

In the previous chapters, I showed two studies of oscillatory flows. From chapter 2 to chapter 5, I studied peristaltic flows to better understand the dynamics of hearing in the human inner ear. In my study, I was able to develop an analytic model that can accurately capture the flow dynamics for physical parameters that have been observed for the inner ear. Furthermore, I was able to implement my model in advection-diffusion simulations. I did this in order to determine the impact of peristaltic flows on the homogenization of fluid in the inner ear. The oscillatory nature of peristaltic flows has an interesting property where the Lagrangian transport dynamics can allow a simple periodic motion to transport material over a channel. I found that the combination of these transport properties with diffusion and the dimensional properties of the inner ear led to an effective mixing mechanism. The findings from this study are not limited to applications in the inner ear. The analytic model is a general solution that can be implemented in many applications where the conditions of long wavelengths, small amplitude, and high Reynolds number are met. Additionally, the model allows for fast mixing modeling for such systems, which can have an impact in other biological systems, as they are topics of interest in the stomach [4] and in microfluidic applications [22]. The experimental design itself has value as well, as the design was proven to be accurate when validated against analytic and numerical models, and unlike previous experimental studies, it is able to model a very large parameter range in wavelength, wave speed, and amplitude. More notably it is able to model arbitrary wave shapes, which also allows the experiment to extend to nondispersive waves. For those interested, I see a path in further developing this study by characterizing and creating a model that can address nondispersive waves. Nondispersive waves are a more realistic way of modeling physical conditions in the inner ear, and perhaps in other biological systems such as the insect hearts, fluid ingestion in insects, insect locomotion, and many others [68]. Additionally, nondispersive waves may have characteristics that allow for enhanced mixing due to the time dependency that is introduced by the nonlinear wave.

From chapter 6 to chapter 8, I studied the effect of channel geometries, where an oscillatory flow is present. The inspiration for this study was an attempt to better understand flows in the glymphatic system, although, over the course of the study, the parameter range of the glymphatic system and my experiment diverged. Still, the study yielded interesting results, that may have some limited applications on the glymphatic system, but still has great applicability to other systems. In short, the study looked at whether a net flow can be generated in a closed-loop channel where a T-junction is present. The results indicated that it is possible if an oscillatory flow is present. I was able to determine that the amplitude and frequency of the oscillatory flow can increase the net flow, as well as reverse the directionality. In an effort to determine the underlying mechanism driving this net flow, I used Nguyen et al. [12] as motivation to focus on the T-junction of the system. I found that changing the T-junction geometry leads to different net flows. Visualizations of the T-junction flow validate the observations from Nguyen et al., as I was able to observe that the time-asymmetric response in the system lead to a valving effect, which in turn produced a net flow in the looped channel. I developed an analytic model, which in conjunction with simulations, was able to predict with some accuracy a feature of the T-junction flow. While the model is not capable of determining why the net flow is induced, it does signal that the missing component is a temporally asymmetric viscous effect. This is likely due to the vortex formation at the T-junction, which the model is incapable of capturing. As previously mentioned, the glymphatic system was the inspiration for this study. However, the Reynolds numbers and Womersley numbers at which I was able to conduct the experiment did not match those of the glymphatic system. This meant that my study is possibly not a good model of the glymphatic system. That said, the conditions that I observed to generate flow in a looped channel are very general. The requirements for a net flow are that a T-junction and an oscillatory flow must be present. There are many systems in nature, such as lungs [69], and corals [70], as well as in engineering applications where we see networks of pipes [71].

Expanding on this work I would focus on two components. First, expanding the looped channel from a single junction to a full network of channels may lead to interesting results that are more applicable to complex networks found in the applications mentioned above. Second, the critical component that leads to a net flow appears to be the separation of the flow at the T-junction. As I demonstrated, the phenomenon I observed is not limited to only one geometry in the T-junction, meaning that establishing criteria that lead to a separation and valving effect at junctions would likely provide a powerful model to understand looped channel systems like this one. Additionally, measuring the position of the separatrix appears to yield information about the effective difference in resistances between the channels in the loop. Specifically, the key component appears to be the difference in resistance in time, as this allows for a valving effect to occur. Developing a model that determines the effective resistance of junctions for bidirectional flows would likely be able to model flows in looped channels like the one I studied.

# Bibliography

[1] L. Chittka and A. Brockmann, "Perception space—the final frontier," PLoS biology **3**, e137 (2005).

[2] (Encyclopædia Britannica, 2023), URL `https://www.britannica.com/science/ear/Transmission-of-sound-within-the-inner-ear#/media/1/175622/537`.

[3] W. Zhou and J.-H. Nam, "Probing hair cell's mechano-transduction using two-tone suppression measurements," Scientific reports **9**, 1 (2019).

[4] S. Alokaily, K. Feigl, and F. X. Tanner, "Characterization of peristaltic flow during the mixing process in a model human stomach," Physics of Fluids **31**, 103105 (2019).

[5] URL `https://www.shutterstock.com/image-vector/digestion-peristalsis-esophagus-stomach-intestine-vector-1375585718`.

[6] URL `https://www.good-pump.com/phone/details.php?id=41658`.

[7] URL `https://pumpsolutions.com.au/applications-peristaltic-pumps/`.

[8] R. Ibanez, M. Shokrian, J.-H. Nam, and D. H. Kelley, "Simple analytic model for peristaltic flow and mixing," Phys. Rev. Fluids **6**, 103101 (2021), URL `https://link.aps.org/doi/10.1103/PhysRevFluids.6.103101`.

[9] M. Y. Jaffrin and A. H. Shapiro, "Peristaltic pumping," Annual Review of Fluid Mechanics **3**, 13 (1971), https://doi.org/10.1146/annurev.fl.03.010171.000305, URL https://doi.org/10.1146/annurev.fl.03.010171.000305.

[10] H. Mestre, J. Tithof, T. Du, W. Song, W. Peng, A. M. Sweeney, G. Olveda, J. H. Thomas, M. Nedergaard, and D. H. Kelley, "Flow of cerebrospinal fluid is driven by arterial pulsations and is reduced in hypertension," Nature communications **9**, 1 (2018).

[11] J. Tithof, K. A. Boster, P. A. Bork, M. Nedergaard, J. H. Thomas, and D. H. Kelley, "A network model of glymphatic flow under different experimentally-motivated parametric scenarios," iScience **25**, 104258 (2022), ISSN 2589-0042, URL https://www.sciencedirect.com/science/article/pii/S2589004222005284.

[12] Q. M. Nguyen, A. U. Oza, J. Abouezzi, G. Sun, S. Childress, C. Frederick, and L. Ristroph, "Flow rectification in loopy network models of bird lungs," Physical review letters **126**, 114501 (2021).

[13] URL https://www.pololu.com/file/0J635/SY20STH30-0604A.pdf.

[14] J. R. Womersley, "Method for the calculation of velocity, rate of flow and viscous drag in arteries when the pressure gradient is known," The Journal of physiology **127**, 553 (1955).

[15] E. Watson, "Diffusion in oscillatory pipe flow," Journal of Fluid Mechanics **133**, 233 (1983).

[16] J. Jiménez-Lozano and M. Sen, "Particle dispersion in two-dimensional peristaltic flow," Physics of Fluids **22**, 043303 (2010).

[17] P. Skafte-Pedersen, D. Sabourin, M. Dufva, and D. Snakenborg, "Multi-channel peristaltic pump for microfluidic applications featuring monolithic pdms inlay," Lab on a Chip **9**, 3003 (2009).

[18] V. Todorov, B. Aprahamian, and H. Tahrilov, in *2016 19th International Symposium on Electrical Apparatus and Technologies (SIELA)* (IEEE, 2016), pp. 1–4.

[19] A. H. Shapiro, M. Y. Jaffrin, and S. L. Weinberg, "Peristaltic pumping with long wavelengths at low reynolds number," Journal of Fluid Mechanics **37**, 799–825 (1969).

[20] K. D. Karavitaki and D. C. Mountain, "Evidence for outer hair cell driven oscillatory fluid flow in the tunnel of corti," Biophysical journal **92**, 3284 (2007).

[21] J. Prakash, D. Tripathi, A. K. Tiwari, S. M. Sait, and R. Ellahi, "Peristaltic pumping of nanofluids through a tapered channel in a porous environment: applications in blood flow," Symmetry **11**, 868 (2019).

[22] K. P. Selverov and H. A. Stone, "Peristaltically driven channel flows with applications toward micromixing," Physics of Fluids **13**, 1837 (2001).

[23] F. Forouzandeh, X. Zhu, A. Alfadhel, B. Ding, J. P. Walton, D. Cormier, R. D. Frisina, and D. A. Borkholder, "A nanoliter resolution implantable micropump for murine inner ear drug delivery," Journal of Controlled Release **298**, 27 (2019), ISSN 0168-3659, URL `https://www.sciencedirect.com/science/article/pii/S0168365919300586`.

[24] S. M. Echteler, R. R. Fay, and A. N. Popper, *Structure of the Mammalian Cochlea* (Springer New York, New York, NY, 1994), pp. 134–171, ISBN 978-1-4612-2700-7, URL `https://doi.org/10.1007/978-1-4612-2700-7_5`.

[25] M. Shokrian, C. Knox, D. H. Kelley, and J.-H. Nam, "Mechanically facilitated micro-fluid mixing in the organ of corti," Scientific Reports **10**, 1 (2020).

[26] R. Fettiplace and J.-H. Nam, "Tonotopy in calcium homeostasis and vulnerability of cochlear hair cells," Hearing research **376**, 11 (2019).

[27] B. Johnstone, R. Patuzzi, J. Syka, and E. Sykova, "Stimulus-related potassium changes in the organ of corti of guinea-pig.," The Journal of physiology **408**, 77 (1989).

[28] J.-H. Nam, Y. Liu, and S. M. Gracewski, in *AIP Conference Proceedings* (AIP Publishing LLC, 2015), vol. 1703, p. 070004.

[29] R. Edge, B. Evans, M. Pearce, C.-P. Richter, X. Hu, and P. Dallos, "Morphology of the unfixed cochlea," Hearing research **124**, 1 (1998).

[30] S. L. Johnson, M. Beurg, W. Marcotti, and R. Fettiplace, "Prestin-driven cochlear amplification is not limited by the outer hair cell membrane time constant," Neuron **70**, 1143 (2011).

[31] T. Jabeen, J. C. Holt, J. R. Becker, and J.-H. Nam, "Interactions between passive and active vibrations in the organ of corti in vitro," Biophysical Journal **119**, 314 (2020).

[32] S. L. Weinberg, E. C. Eckstein, and A. H. Shapiro, "An experimental study of peristaltic pumping," Journal of Fluid Mechanics **49**, 461 (1971).

[33] Y. C. Fung and C. S. Yih, "Peristaltic Transport," Journal of Applied Mechanics **35**, 669 (1968), `https://asmedigitalcollection.asme.org/appliedmechanics/article-pdf/35/4/669/5449404/669_1.pdf`, URL `https://doi.org/10.1115/1.3601290`.

[34] F. Yin and Y. Fung, "Comparison of theory and experiment in peristaltic transport," Journal of Fluid Mechanics **47**, 93 (1971).

[35] F. C. Yin, *Theoretical and experimental investigations of peristalsis* (University of California, San Diego, 1970).

[36] J. N. J. Lozano, *Peristaltic flow with application to ureteral biomechanics* (University of Notre Dame, 2009).

[37] J. Jiménez-Lozano, M. Sen, and E. Corona, "Analysis of peristaltic two-phase flow with application to ureteral biomechanics," Acta mechanica **219**, 91 (2011).

[38] J. Jiménez-Lozano, M. Sen, and P. F. Dunn, "Particle motion in unsteady two-dimensional peristaltic flow with application to the ureter," Physical Review E **79**, 041901 (2009).

[39] K. AYUKAWA, T. KAWAI, and M. KIMURA, "Streamlines and path lines in peristaltic flow at high reynolds numbers," Bulletin of JSME **24**, 948 (1981).

[40] S. Takabatake and K. Ayukawa, "Numerical study of two-dimensional peristaltic flows," Journal of Fluid Mechanics **122**, 439 (1982).

[41] D. G. Andrews and M. E. Mcintyre, "On wave-action and its relatives," Journal of Fluid Mechanics **89**, 647–664 (1978).

[42] D. G. Andrews and M. E. Mcintyre, "An exact theory of nonlinear waves on a lagrangian-mean flow," Journal of Fluid Mechanics **89**, 609–646 (1978).

[43] E. C. Eckstein, Ph.D. thesis, Massachusetts Institute of Technology (1970).

[44] J. Stewart, *Calculus* (Cengage Learning, 2015).

[45] L. D. Landau and E. M. Lifshitz, *Fluid Mechanics: Landau and Lifshitz: Course of Theoretical Physics, Volume 6*, vol. 6 (Elsevier, 2013).

[46] W. Thielicke and E. J. Stamhuis, “Pivlab – towards user-friendly, affordable and accurate digital particle image velocimetry in matlab,” Journal of Open Research Software **2** (2014).

[47] D. H. Kelley and N. T. Ouellette, “Using particle tracking to measure flow instabilities in an undergraduate laboratory experiment,” Am. J. Phys. **79**, 267 (2011).

[48] R. Ibanez and D. H. Kelley, “A bioinspired apparatus for modeling peristaltic pumping in biophysical flows,” Bioinspiration and Biomimetics **17**, 066023 (2022), URL `https://dx.doi.org/10.1088/1748-3190/ac9c7e`.

[49] D. E Troyetsky, J. Tithof, J. H Thomas, and D. H Kelley, “Dispersion as a waste-clearance mechanism in flow through penetrating perivascular spaces in the brain,” Sci Rep **1**, 1 (2021).

[50] G. I. Taylor, “Dispersion of soluble matter in solvent flowing slowly through a tube,” Proceedings of the Royal Society of London. Series A. Mathematical and Physical Sciences **219**, 186 (1953).

[51] R. Aris, “On the dispersion of a solute in a fluid flowing through a tube,” Proceedings of the Royal Society of London. Series A. Mathematical and Physical Sciences **235**, 67 (1956).

[52] J. J. Iliff, M. Wang, Y. Liao, B. A. Plogg, W. Peng, G. A. Gundersen, H. Benveniste, G. E. Vates, R. Deane, S. A. Goldman, et al., “A paravascular pathway facilitates csf flow through the brain parenchyma and the clearance of interstitial solutes, including amyloid $\beta$,” Science translational medicine **4**, 147ra111 (2012).

[53] D. H. Kelley, T. Bohr, P. G. Hjorth, S. C. Holst, S. Hrabětová, V. Kiviniemi, T. Lilius, I. Lundgaard, K.-A. Mardal, E. A. Martens, et al., “The glymphatic system: Current understanding and modeling,” Iscience p. 104987 (2022).

[54] A. Ramuzat and M. Riethmuller, in *11th International Symposium on Applications of Laser Techniques to Fluid Flows* (Citeseer, 2002), pp. 13–16.

[55] D. N. Ku, D. P. Giddens, C. K. Zarins, and S. Glagov, "Pulsatile flow and atherosclerosis in the human carotid bifurcation. positive correlation between plaque location and low oscillating shear stress.," Arteriosclerosis: An Official Journal of the American Heart Association, Inc. **5**, 293 (1985).

[56] S. TAKAGI and T. SAIJO, "Study of a piston pump without valves: 1st report, on a pipe-capacity-system with a t-junction," Bulletin of JSME **26**, 1366 (1983).

[57] S. TAKAGI and K. TAKAHASHI, "Study of a piston pump without valves: 2nd report, pumping effect and resonance in a pipe-capacity-system with a t-junction," Bulletin of JSME **28**, 831 (1985).

[58] G. Propst, "Pumping effects in models of periodically forced flow configurations," Physica D: Nonlinear Phenomena **217**, 193 (2006).

[59] J. Á. Cid, G. Propst, and M. Tvrdỳ, "On the pumping effect in a pipe/tank flow configuration with friction," Physica D: Nonlinear Phenomena **273**, 28 (2014).

[60] Q. M. Nguyen, J. Abouezzi, and L. Ristroph, "Early turbulence and pulsatile flows enhance diodicity of tesla's macrofluidic valve," Nature communications **12**, 1 (2021).

[61] D. Borrero-Echeverry, C. J. Crowley, and T. P. Riddick, "Rheoscopic fluids in a post-kalliroscope world," Physics of Fluids **30**, 087103 (2018).

[62] B. Eckhardt, T. M. Schneider, B. Hof, and J. Westerweel, "Turbulence transition in pipe flow," Annual review of fluid mechanics **39**, 447 (2007).

[63] D. Oettinger, J. T. Ault, H. A. Stone, and G. Haller, "Invisible anchors trap particles in branching junctions," Physical review letters **121**, 054502 (2018).

[64] J. T. Ault, A. Fani, K. K. Chen, S. Shin, F. Gallaire, and H. A. Stone, "Vortex-breakdown-induced particle capture in branching junctions," Physical review letters **117**, 084501 (2016).

[65] K. K. Chen, C. W. Rowley, and H. A. Stone, "Vortex breakdown, linear global instability and sensitivity of pipe bifurcation flows," Journal of Fluid Mechanics **815**, 257 (2017).

[66] S.-J. Kim, R. Yokokawa, S. C. Lesher-Perez, and S. Takayama, "Constant flow-driven microfluidic oscillator for different duty cycles," Analytical chemistry **84**, 1152 (2012).

[67] Q. M. Nguyen, Ph.D. thesis, New York University (2021).

[68] F. Esser, T. Masselter, and T. Speck, "Silent pumpers: a comparative topical overview of the peristaltic pumping principle in living nature, engineering, and biomimetics," Advanced Intelligent Systems **1**, 1900009 (2019).

[69] K. Pradhan and A. Guha, "Fluid dynamics of oscillatory flow in three-dimensional branching networks," Physics of Fluids **31**, 063601 (2019).

[70] J. E. Samson, L. A. Miller, D. Ray, R. Holzman, U. Shavit, and S. Khatri, "A novel mechanism of mixing by pulsing corals," Journal of Experimental Biology **222**, jeb192518 (2019).

[71] E. B. Wylie and V. L. Streeter, *Fluid transients* (1978).

[72] H. Jeffreys, "Lxxvi. the stability of a layer of fluid heated below," The London, Edinburgh, and Dublin Philosophical Magazine and Journal of Science **2**, 833 (1926).

# A Appendix

## A.1 Experiment Hardware

I designed the channel to be a 2.54 cm (1 inch) square channel. The main considerations were that I needed to be able to deform one of the walls, and since I wanted to be able to visualize the induced flow, the wall material would have to be transparent (at least on two ends). As such, I decided to use 1.27 cm (1/2 inch) transparent polycarbonate sheets for the channel fabrication. For the flexible wall, I decided to use rubber and secure it into position via compression. I machined the polycarbonate walls to size and slotted sections in the sheets for assembly. I created features for the rubber to sit on top of the side walls and be compressed by the top section. Inside the slots, I machined smaller slots intended for sealant as shown in figure A.2, however, I found that they were ineffective due to limitations in the straightness of the long channel walls. I resolved this issue by simply filling gaps with silicone sealant.

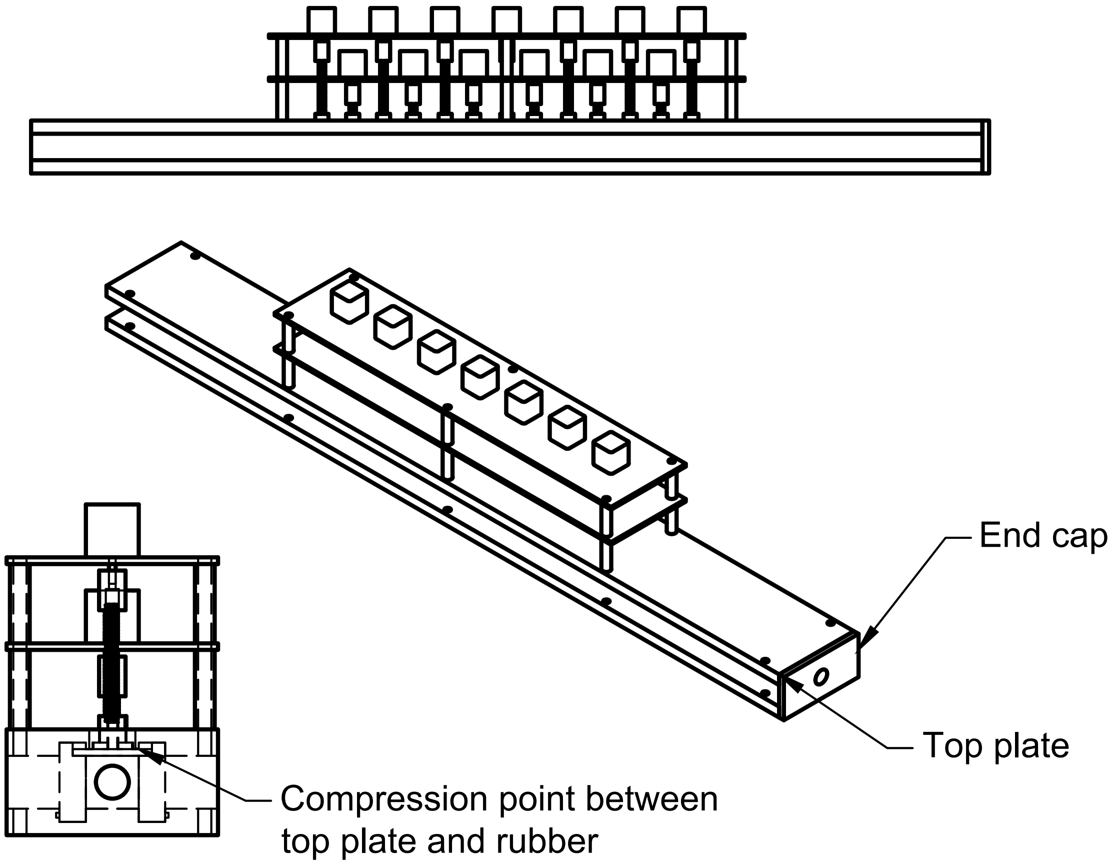


**Figure A.1:** The drawing shows the assembly of the experiment using the parts previously described. Indicated is how the top section of the channel applies compression on the rubber sheet to secure it in position, and produce a seal.

I fabricated the section responsible for compressing the rubber wall by machining the same polycarbonate sheet I used for the other walls. Figure A.1 shows a schematic of the compression plate that keeps the rubber in position. Additionally, the compression on the rubber seals the channel in the indicated section in figure A.2.

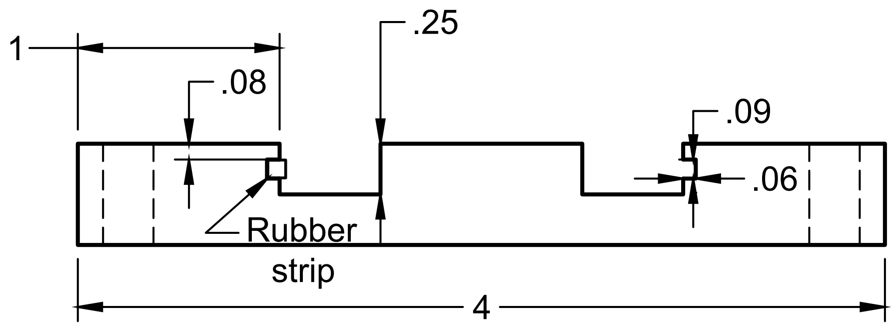


**Figure A.2:** Schematic of the bottom component of the channel in the experimental device. All units are in inches. Notably, I machined a small slot where the side walls are inserted to introduce a rubber strip to act as a seal.

I revised the design shown in figure A.1 due to the fact that the rubber wall was too hard for the actuators in the final design to deform. The reason is discussed in further detail in section 2.3.3. To reduce the stiffness of the wall, I opted to use a much thinner rubber sheet. To do this, I had to fabricate a structure that would sandwich the rubber in place, while performing the same role as the previous wall. Figure A.3 shows a schematic of the structure and rubber membrane. I fabricated the structure by using a BOSS laser cutter, then stacking the components to achieve a structure as shown in the figure.

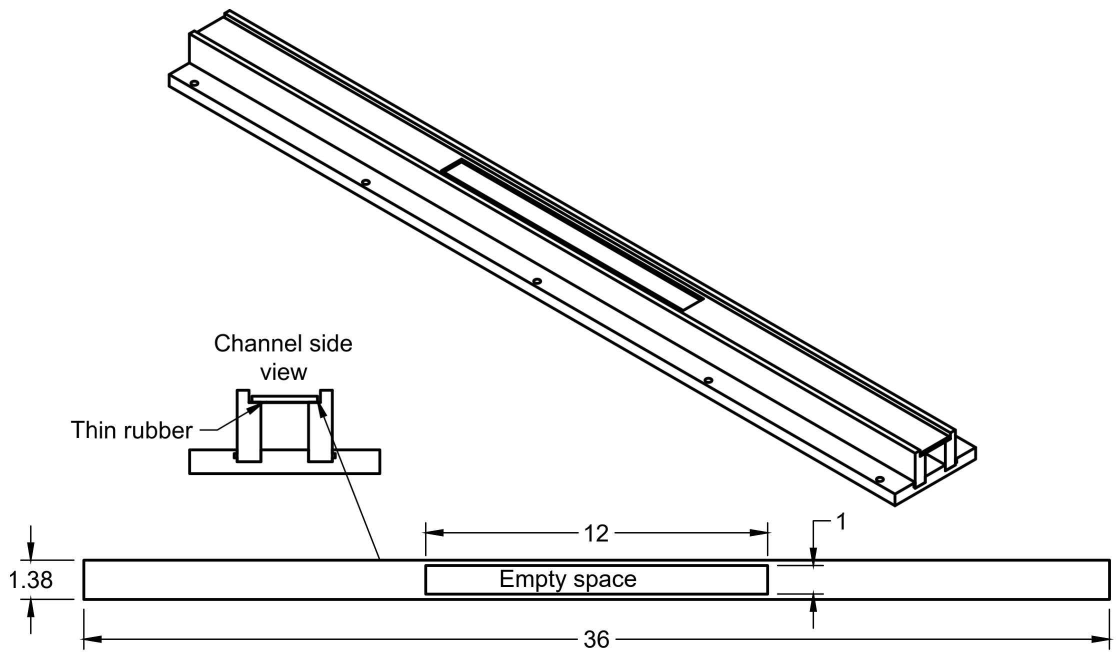


**Figure A.3:** Schematic indicating the location of the rubber seal (McMaster Square-Profile Oil-Resistant Buna-N O-Ring Cord Stock, part number 9700K12).

The effective size of the channel $L$ could be modified by introducing polycarbonate sheet spacers as shown in figure 4.1. The polycarbonate sheets matched the width of the channel (1 inch), spanned the length of the experiment, and had a thickness of 0.125 inches. Introducing two spacers would effectively turn the 1x1 inch channel into a 1x3/4 inch channel.

Above the top section of the channel, I constructed two plates that hold the actuators that displace the rubber sheet. The plates are placed in position with (2.54 cm) 1-inch spacers and have the patterns for NEMA 7 or NEMA 14 stepper motors machined on them. The original design used NEMA 7 stepper motors and was fabricated using polycarbonate sheets, however, I found that the polycarbonate sheets also tended to deflect when the actuators were in operation. To fix this I redesigned the shelves to be steel plates.

The end wall design shown in Figure A.4 remained constant throughout the study, with the exception of the tubing adapter portion. When a flow was induced in the channel, the fluid was forced to pass through the square channel and into the connected tubing, which had a reduced flow area than the full one-inch square channel. To investigate the effect of this reduction in flow area, various tubing sizes were tested, yet no effect was found.

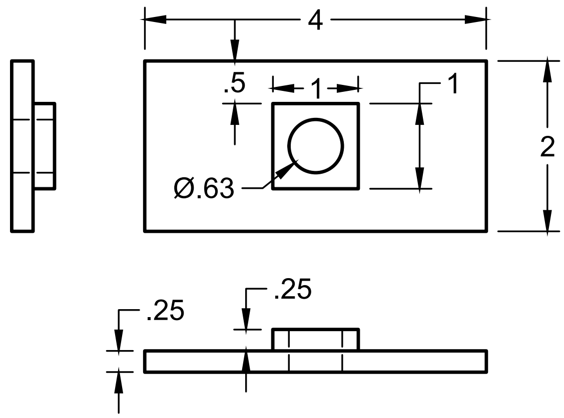


**Figure A.4:** The drawing shows the end walls (or caps) of the channel. The middle hole is an NPT 1/8 threaded hole where a hose is connected to the rest of the fluid system. The units shown are in inches.

Finally, the system was interconnected with tubing as shown in figure A.5. These connections ensure that the fluid can recirculate or create different conditions in the system. The valves serve to cut off the flow and create different configurations without the need to disconnect anything. Additionally, during the actual preparations for experiments, the valves make it significantly easier to fill the channel with water.

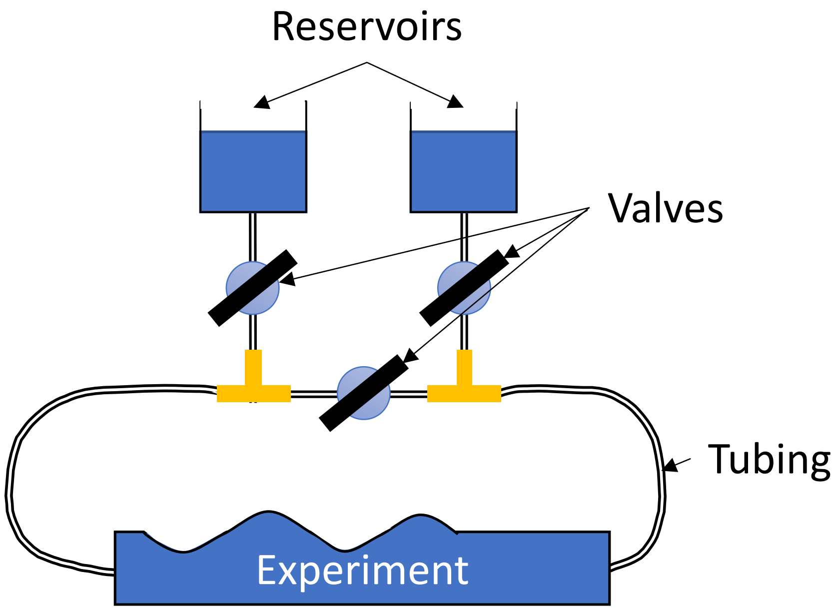


**Figure A.5:** The figure is a sketch that indicates how the major components of the experiment were interconnected. In essence, the experiment set up was a channel connected to a series of valves to allow me to fill the channel with fluid, ensure that the system has no trapped bubbles, and change the boundary conditions of the system by closing or opening valves, or change the pressure conditions by changing the amount of fluid at each reservoir, creating a pressure gradient along the experiment.

### A.1.1 Limitations and Flaws

In the previous subsection, I showed how I iterated on the design to overcome certain limitations and flaws. However, not every single issue was resolved and as such I will detail in this subsection the unresolved limitations and flaws. The rubber sheet required significant compression to properly seal the channel, this meant that the polycarbonate walls would flex and stress. Eventually, this led to the formation of cracks in the polycarbonate walls which had to be sealed. To address the damage and stress caused by compression I changed two things: First, the top wall was redesigned to be made out of aluminum. This eliminated any flexing and did a better job of distributing compression. Second, I added small steel plates underneath the bottom wall to distribute the forces on the bottom polycarbonate wall. The bottom wall must remain transparent since it is needed for the illumination of particles in the experiment, and the steel braces act as washers to distribute the compression force and prevent damage. Large deformations were sometimes an issue. Particularly with the design shown in figure A.1, the rubber sheet would be displaced in such a way that the seal with the side walls would no longer be effective. As mentioned earlier, the second design is a workaround for this, but at the cost of the modeling capabilities of a continuous wave. To elaborate on the limitations of wavelength modeling, first consider that the wall is not deformed in a continuous manner. The wall is actuated at discrete points over the wall, which means the material of the rubber will dictate how accurately a continuous deformation over the wall is modeled. Figure A.6 is a sketch that shows the consequences of different materials given a specific setup. In general, thinner, more stretchable material allows larger amplitudes, but it can result in what I call 'dimples' in the wave because the actuation points are too far apart. A hard thicker, harder rubber will in general do the opposite, thus making it much harder to deflect the wall other than for very small amplitudes.

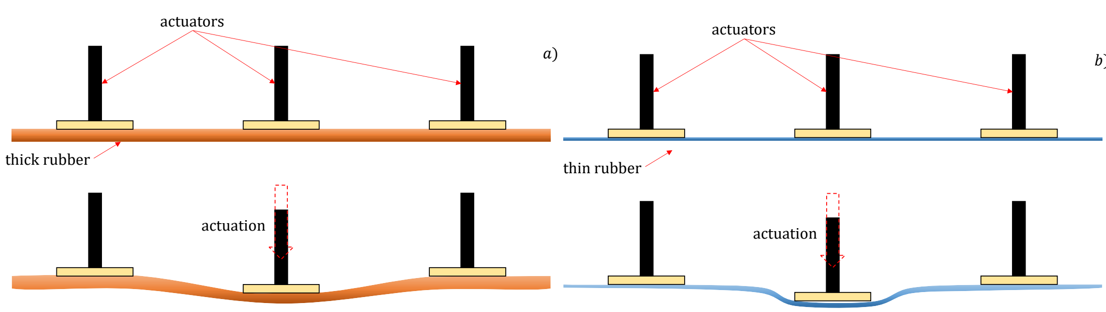


**Figure A.6:** The sketches contrast the effects of a thick and thin rubber wall on the experiment. a) Is an example where the rubber is thick, and so as an actuator deforms the sheet, it creates a smooth curve between actuators. b) Is an example of a thin rubber wall, where the wall only deformed locally, creating a sort of dimple, instead of a smooth curve between actuation points.

The vertical alignment of actuators, while not a critical component to consider for the accuracy of modeling itself, can cause significant issues during operation. The alignment of the actuators refers to the alignment between a stepper motor, the shaft coupling, the threaded shaft, and the threaded nut. Figure A.7 shows how the position of these components is related. One can see from the figure that if an angle is present, then there will be additional frictional forces between the components, besides the loading components of the actuation. Not only this, but severe misalignment (assuming it does not stall the motors) also means that the translational motion of the actuator will not be accurate, as the actuator will not displace the membrane just in $y$ (as is the ideal case), but also have an $x$ component. However, it is unlikely that inaccuracy is a problem, as stalling issues will almost always occur before the alignment is so poor that the accuracy of the actuator displacement is severely affected. The only way I found to ensure that the actuation remained smooth was to assemble the following actuator components loosely, then slightly tighten them to ensure the set screw did not produce significant misalignment due to the compression on the thread.

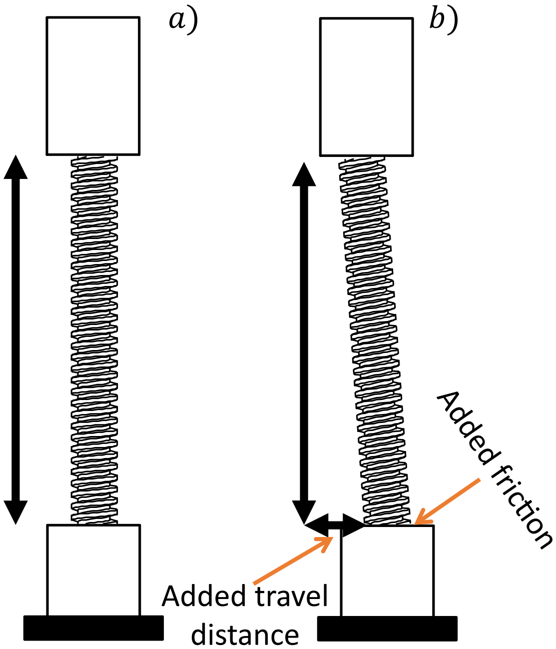


**Figure A.7:** Comparison of an aligned (a) and misaligned actuator (b). The sketch shows how a misaligned actuator would increase friction in the contact region with the bottom section, as well as not produce an accurate vertical displacement due to an added horizontal displacement.

## A.2 Control

In this section, I will detail the electronic and software components of the experiment.

As I showed in the previous subsection, the flexible wall is deformed by an array of actuators bolted above the flexible wall. The actuators work by using 16 or 20 stepper motors (Pololu Bipolar NEMA 7 3.9 Volt 0.6 Amp/phase or Pololu Bipolar NEMA 14 10 Volt 0.5 Amp/phase), each of which drives a threaded shaft in a nut that displaces the membrane. The assembly of the stepper motor, threaded shaft, and nut is what I refer to as an 'actuator'. These actuators are connected to a custom-made PCB board. The board contains 20 Pololu DRV-8825 stepper motor drivers, which interface with a MEGA 2560 Arduino. During construction, I used wire to connect all components, I would seriously recommend against this. The amount of cabling required is significant, one can expect at least 3 connections per controller to the Arduino board, meaning at least 60 wires must be used to that, then there are 4 wires per motor, and so on. As such I designed the PCB board, whose diagram is in figure A.8. At this point, I have described all the physical hardware that encompasses the experiment system itself. Now I move on to describe how I developed an interface from a computer to the experiment for control.

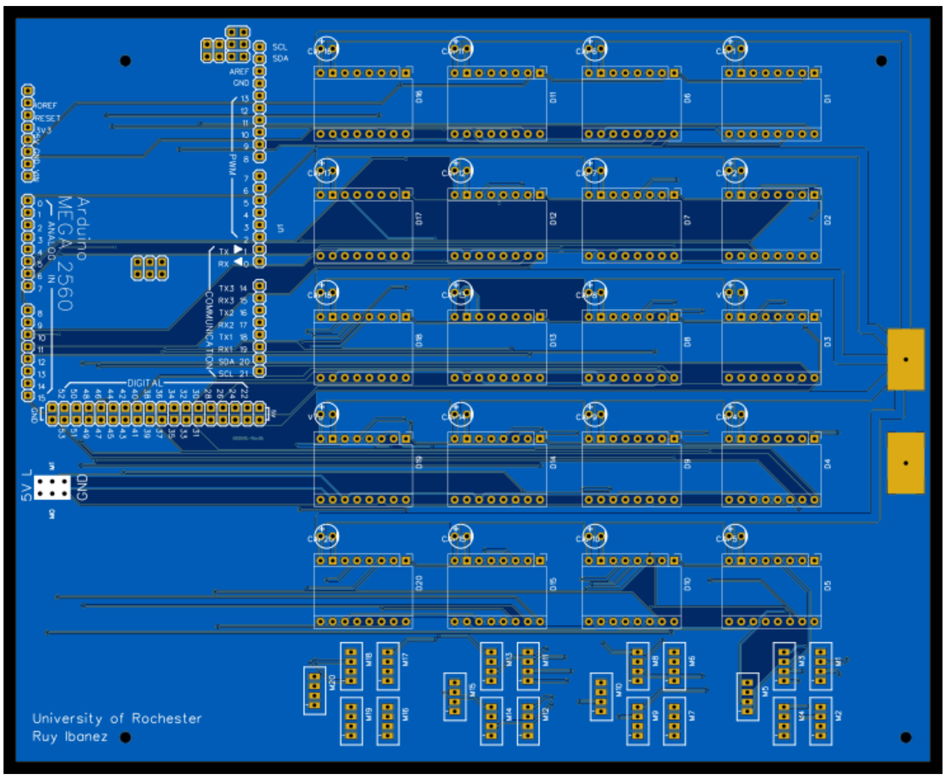


**Figure A.8:** The figure shows an image of the PCB board I designed for controlling the experimental hardware.

The software controls for this system are divided into two parts: MATLAB and Python code. First, MATLAB code is used to define the desired control parameters, such as the type and parameters of the sinusoidal wave. This code is then used to generate a text file containing the relevant data, which is then read by the Python code. The Python code reads the text file data and communicates with the Arduino board, which then drives the experiment accordingly.

The Python code receives a text file as input, which contains the stepping data for the stepper motors. It performs two primary functions: translating the text file into data that the Arduino can interpret as signals for the motion of the stepper motors, and controlling the frequency of data input into the Arduino board. The code communicates with the microcontroller to ensure communication is not interrupted and prevents the board from being overwhelmed with data.

The MATLAB code is responsible for translating the desired input, a traveling sine wave deformation with parameters $xi$, into a signal that the experiment can use. This signal must take into account the characteristics of the experiment system, such as the actuator thread and stepper motor characteristics, as well as the fixed frequency at which the Arduino board will output a signal. Each signal will instruct the stepper motor controller to step (or not to step) in a specific direction. The MATLAB algorithm uses the motor hardware parameters $S_m$ and $T_m$ and the idealized displacement to calculate the necessary motions to model the idealized wave. The MATLAB code grabs the ideal wave (that which the user wants to be modeled)

and what action must be taken at each signal that is sent out. To determine which signal is coded into the output, the code uses the following algorithm. Figure A.9 illustrates the algorithm that determines the motion.

Consider the $i^{\text{th}}$ stepper motor to be located on the flexible wall at position $x_i$. Each motor can displace the flexible wall in a discrete position, by a distance $\eta_i(x_i, t)$. The stepper motors have discrete motions with minimum displacement $\delta y_m = S_m T_m$. In order to simulate a continuous deformation of the wall in the apparatus, the MATLAB code calculates the motion required by each motor by taking the error between the idealized function $\eta(x, t)$ at the upcoming time $t_1$ and the motor's current deflection at the current time $t_0$. The scale of the discrete time is dictated by the signal output rate of the hardware (Arduino MEGA2560

R3 in our case). For example, if the controller output signals at a rate of 2 kHz, then the time scale is equal to 500 $\mu$s. The error is calculated by

$$\delta_e = \eta(x, t_1) - \eta(x, t_0). \tag{A.1}$$

Now the MATLAB algorithm determines that, if $\delta_e$ is larger than half the minimum displacement, i.e. $|\delta_e| > \delta y_m/2$, then a step output is produced with the according direction to minimize the error. For example, in the case of $\delta_e$ being positive, the algorithm determines a step in the negative direction must be taken. Otherwise, no step is produced as the current location is where the error is minimized. The MATLAB code uses equation A.1 at each point in time to produce a text file that contains the motion information for the stepper motors.

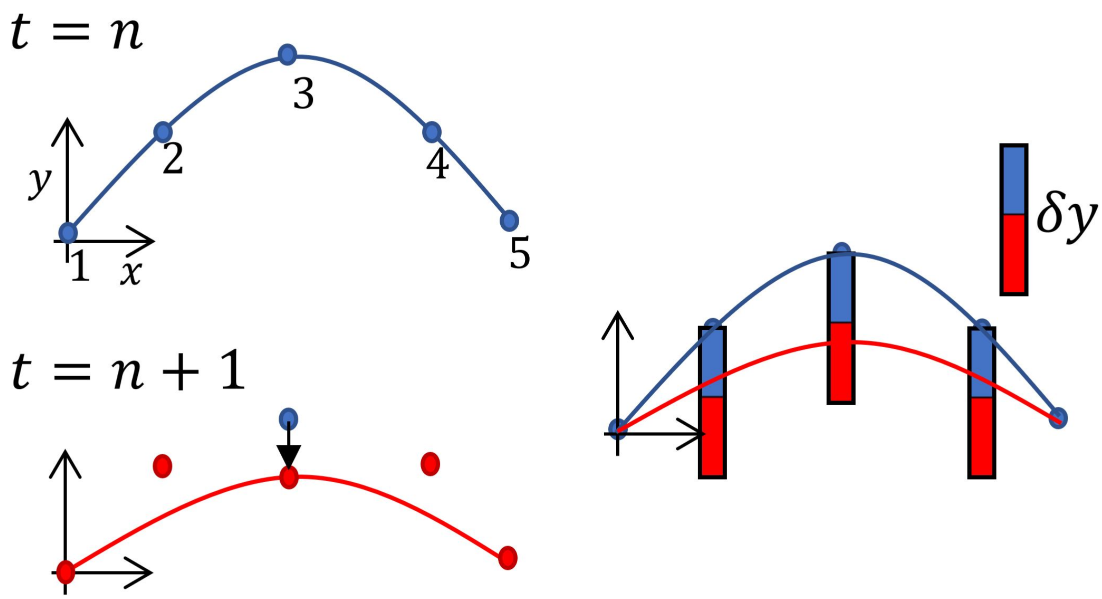


**Figure A.9:** A sketch is presented that demonstrates the algorithm used to determine if a stepper motor must take a step. The red and blue curves represent conceptualized wall positions, and the circles symbolize the position of the $i^{th}$ stepper motor. The middle image exhibits the calculation necessary to decide if a step must be initiated between time $n$ and $n + 1$.

**Control Limitations**

As with any experimental apparatus, there are limits to the parameters that can be input into the system. Most of these limitations should not impede experiments from spanning large parameter sets if understood in the planning stages of a project. Primarily one must be aware that there is a limiting factor to the frequency and amplitude that the actuators can model. This is due to the fact that any stepper motor controller will have a limit on their rotation velocity. Figure A.10 shows a torque curve for the stepper motors I used in my experiment. The figure shows that as the frequency of rotation of the stepper increases, the torque output decreases. Most stepper motors will share similar characteristics. Given this, at some point, the motor will stall and be unable to move. How quickly one reaches this limiting factor is dependent on the stiffness of the actuated membrane, a stiff membrane will require higher torque to be deformed, meaning stalling will occur at lower rotation frequencies. That said, there will be a rotation frequency where the stepper motor will stall even if it has no load. Another factor that can increase torque requirements is the alignment of the actuators.

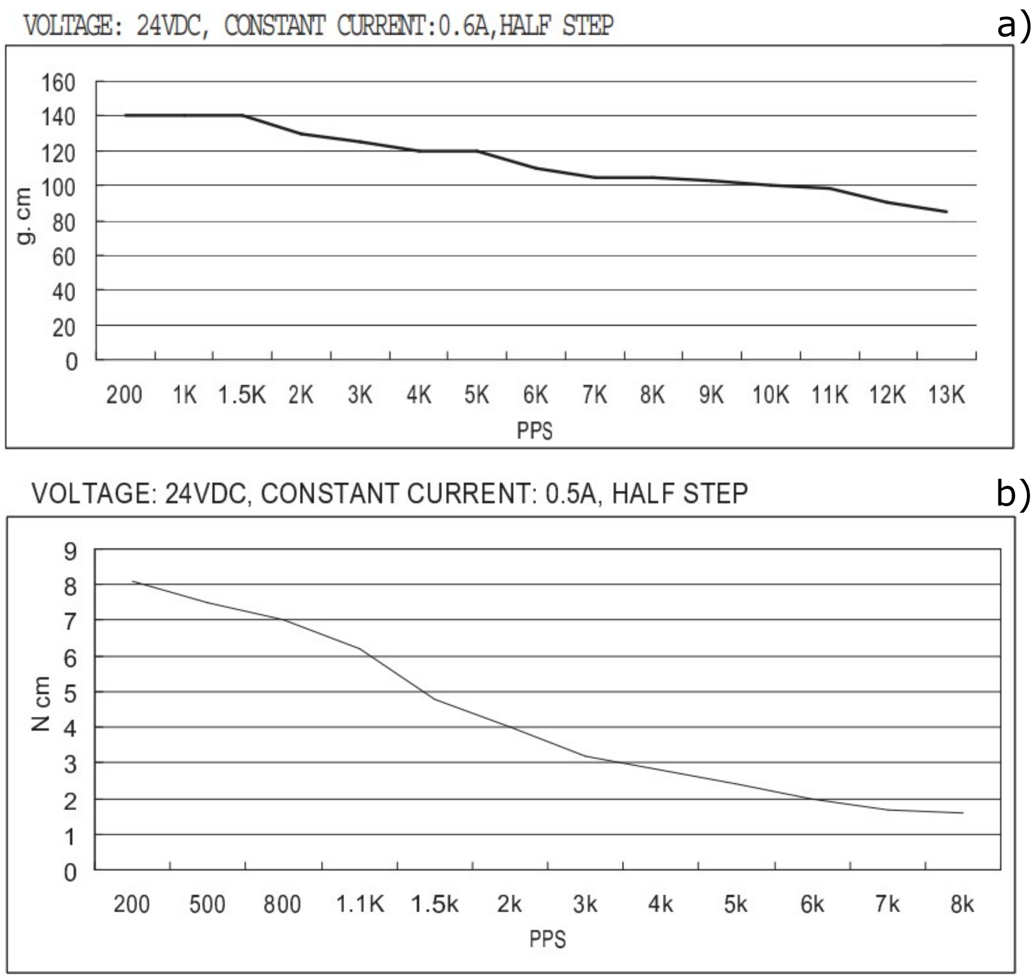


**Figure A.10:** Stalling torque curves for stepper motors from Pololu's datasheets [13]. PPS stands for pulse per second, the vertical axis is units of torque. Both curves are given for the half-step mode and are expected to have lower values for finer microstepping. a) Pololu Bipolar NEMA 7 3.9 Volt 0.6 stalling torque curve. Amp/phase b) Pololu Bipolar NEMA 14 10 Volt 0.5 Amp/phase stalling torque curve.

### Convection

During experimental measurements at low flow speeds, I found that measurements showed unusual movement without any input. There were two possible explanations for the passive flow I observed. One was that the particles were failing to be neutrally buoyant, and the second was that thermal convection was producing some sort of flow. To determine the cause of the passive flow, I tracked particle motion after allowing the experiment to reach thermal equilibrium after being filled with water. I found that particles moved around in a pattern that resembled convection, and not a vertical motion that would be characteristic of particles being too dense (falling downward) or too light (floating upward). Figure A.11 shows a plot of measured particle paths with no input.

To get an estimate of how long the system would take to reach thermal equilibrium, I use the heat equation to calculate a time scale for the system. The heat equation is

$$\frac{\partial T}{\partial t} = \frac{k}{c_p \rho} \nabla^2 T, \tag{A.2}$$

where the parameters $k$ is the thermal conductivity, $c_p$ is the specific heat and $\rho$ is the density of the material. For our case, I use water as the material. The experiment's channel size is a square channel of length $L = 2.54cm$. I use this as the spatial length scale for the heat equation. Solving for the time scale in the equation gives 4510 seconds as shown in equation A.3

$$t = \frac{c_p \rho L^2}{k} = 4510s \tag{A.3}$$

At this point, I estimated the thermal sensitivity of the experiment by calculating the critical Rayleigh number. The Rayleigh number is a measure of the balance between buoyancy and viscosity of a fluid and is used to describe the stability of convection. The Rayleigh number for a two-dimensional system is given by

$$Ra = \frac{g \alpha_T h^3 \Delta T}{\nu \kappa} \tag{A.4}$$

where $g$ is the acceleration of gravity, $\alpha_T$ is the coefficient of expansion of the fluid, $\nu$ is the kinematic viscosity of the fluid, $h$ is the height of the system, $\Delta T$ is the thermal gradient from top to bottom and $\kappa$ is the thermal diffusivity. The critical Rayleigh number for a system with solid boundaries was calculated by Jeffreys [72] to be $Ra_c = 1708$. With this information, I want to solve for the thermal gradient that would reach a critical Rayleigh number in our system. Rearranging to solve for the thermal gradient gives that the system is sensitive to thermal gradients of 6 millikelvin.

$$\Delta T = \frac{\nu \kappa Ra_c}{g \alpha h^3} = 0.006^o C \tag{A.5}$$

The results from this test suggested that the system is very thermally sensitive and suppressing convective flows would require extensive modifications. To address this the simplest solution was to restrict experiments to flows that produce much stronger flows than that of the background convection.

I decided to attempt to eliminate the apparent convective flow in the system I would create a small stable thermally driven stratification. In detail, since the density of water is dependent on temperature, the goal was to heat the top of the channel such that a temperature distribution would be induced. In the ideal scenario, the top of the channel would be the highest temperature and decay to the lowest temperature at the bottom. Given the linear dependency of temperature to density, this would ideally create conditions that would eliminate convection.

I used 22AWG Nickel-Chromium wire to create a heating pad on the top part of the experiment and proceeded to induce a current using a variable power supply. I calculated the heat input to be 80 $W$. To track the temperature at the walls I used thermocouples which I positioned throughout the experiment to measure temperature at different locations.

I found that even by creating a $5^o C$ thermal gradient between the bottom and top wall, I could not suppress convection effects. Even after waiting for the estimated thermal equilibrium time scale, flow patterns of convection were still present in the experiment. Figure A.12 shows the results of this testing and how it is not enough to eliminate the background flow.

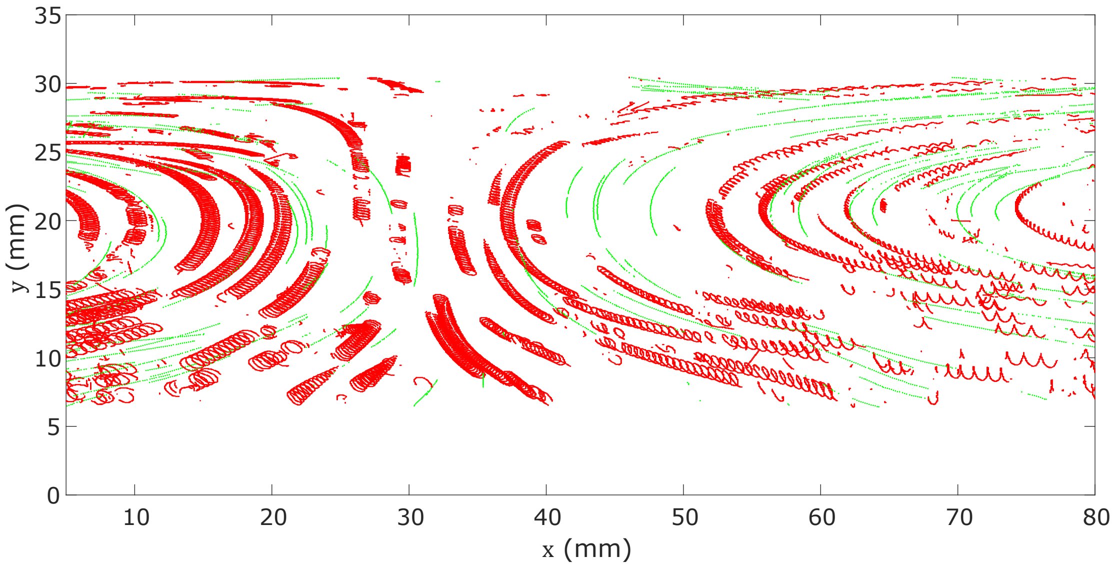


**Figure A.11:** Shown is a plot of experimental measurements. The $x$ and $y$ axis are positions in the visualization window of the experimental measurements. The red lines show particle paths measured using PTV when a peristaltic motion is forced in the system. The blue lines show measured particle paths where a low pass filter was applied on the red measurements, attempting to eliminate the oscillatory component of the particle path. The green lines were PTV measurements with no forcing on the system. It is very notable that the particles appear to follow a path that resembles Rayleigh-Bernard convection, where hot fluid travels upwards, and cold fluid downwards producing a vortex-like structure.

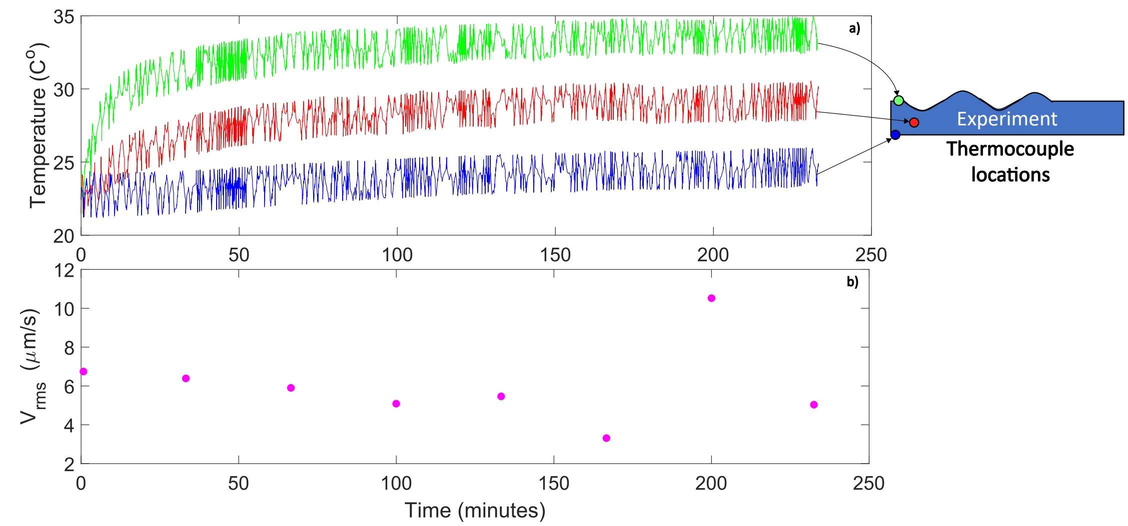


**Figure A.12:** Plotted are temperature measurements over time at three locations in the experimental device. These measurements were conducted while heating the top of the experiment. The sketch shows the location where I placed thermocouples for temperature measurements, the color of the plots matches the sketch locations. Over time a temperature gradient is produced and increases in the experiment between the top and the bottom. Plotted in pink circles are $V_{\mathrm{rms}}$ measurements of particles in the fluid. My hope from this experiment was to be able to eliminate the background flow as a stable temperature gradient is induced in the system. However, as the measurements of $V_{\mathrm{rms}}$, the added temperature gradient did not eliminate the presence of a background flow.

Given that I was unable to eliminate this convection-driven flow, I had to find a way to move forward with experiments without my measurements being affected by this background flow. The simplest thing to do was to simply measure the velocity magnitude of the background flow. Using the techniques that I discussed in section 4.2, I used PTV to track particles in the fluid and obtain their velocities. I then measured the root-mean-square velocity in order to determine the intensity of the flow. The root-mean-square velocity was calculated as

$$V_{\mathrm{rms}} = (\overline{u^2 + v^2})^{1/2}, \tag{A.6}$$

where $u$ is the velocity in the $x$-direction, $v$ is the velocity in the $y$-direction, and the overline is the spatiotemporal average over the bulk region of the flow, which I define as $0.05L \leq y \leq 0.9L$. From the PTV measurements, I obtained a root-mean-square velocity of $V_{\text{rms}} = 0.1$ mm/s. Knowing this value, I simply constrained myself to model flows that I expected to yield velocities that were orders of magnitude higher, this would ensure the convection-driven background flow was a small noise signal in my measurements.

### A.2.1 Minor Leakages

A final remark regarding the experimental design; a persistent minor issue with the experimental apparatus was the existence of minor leaks in the system. These leaks mainly occurred in components that I frequently removed. When reinstalling, I utilized vacuum grease (Dow Corning D-65201) to guarantee no leaks happened. For components that I infrequently disassembled or were cracked, I applied silicon sealant (Dow Corning RTV Sealant 732) to eliminate leaks.

## A.3 Side Note on Low Reynolds Number Flow in the System

Before concluding I want to make a brief side note on low Reynolds number measurements. Ultimately, the motivation for this study was to apply the findings to the glymphatic system. As such, one important consideration was that the observations I made with water were done at a much higher Reynolds number ($Re > 1$). While the higher flow velocities do not detract from the interesting results, it was preferable for me to analyze a closer analog to the glymphatic system by having a much more viscous dominated system. To do this I changed the fluid from water to glycerin. Doing so changes the viscosity of the system to approximately $5 \cdot 10^{-6}$ m/s$^2$ from $10^{-6}$ m/s$^2$. As a consequence, Reynolds numbers fall from the order of 100 to 0.1, and Womersley numbers drop from the order of 10 to 0.1.

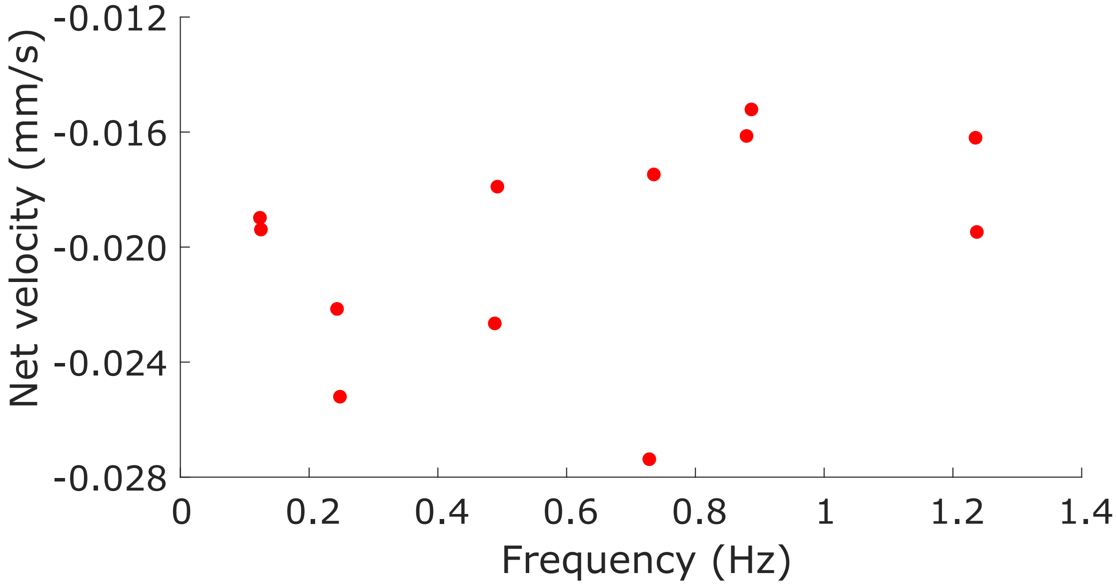


**Figure A.13:** Shown are measurements of the net velocity at TJ-1 as a function of $f$. These are the only measurements where the system used glycerin instead of water. The data was noisy but clearly shows a net velocity is present. The direction of the flow is negative for all measurements, unlike previous measurements with water.

The only measurements using glycerin are presented in figure A.13. They indicate that particles are experiencing a net velocity. The measurements suggest that the phenomenon causing the net velocity is still present even in highly viscous flow. Notably, the direction of the net velocity was inverted from that observed in the case of low values of $S$ and $f$ in figure 8.4. This possibly means that low values of $S$ and $f$ that lead to a reversal in direction, may also be tied to the viscosity of the fluid. This implies that inertia is of lesser importance in inducing a net velocity, suggesting that the direction of the net flow generated in the glycerin case can potentially be changed by increasing $S$ or $f$.